UNIVERSIDAD DE CHILE
FACULTAD DE CIENCIAS FÍSICAS Y MATEMÁTICAS
DEPARTAMENTO DE INGENIERÍA ELÉCTRICA

PARAMETRIC AMPLIFICATION OF ELECTROMAGNETIC SIGNALS WITH SUPERCONDUCTING TRANSMISSION LINES

TESIS PARA OPTAR AL GRADO DE
MAGÍSTER EN CIENCIAS DE LA INGENIERÍA, MENCIÓN ELÉCTRICA

JAVIER ALEJANDRO CARRASCO ÁVILA

PROFESOR GUÍA:
FAUSTO PATRICIO MENA MENA
PROFESOR CO-GUÍA:
CLAUDIO MOISÉS FALCÓN BEAS

MIEMBROS DE LA COMISIÓN:
ERNEST MICHAEL
MÓNICA AMPARO GARCÍA ÑUSTES

Este trabajo ha sido financiado por los proyectos ANID Fondecyt 1180700, BASAL AFB170002 y ACE210002

SANTIAGO DE CHILE
2022

RESUMEN DE LA TESIS PARA OPTAR
AL GRADO DE MAGÍSTER EN CIENCIAS DE LA INGENIERÍA, MENCIÓN ELÉCTRICA
POR: JAVIER ALEJANDRO CARRASCO ÁVILA
FECHA: 2022
PROF. GUÍA: FAUSTO PATRICIO MENA MENA
PROF. CO-GUÍA: CLAUDIO MOISÉS FALCÓN BEAS

AMPLIFICACIÓN PARAMÉTRICA DE SEÑALES ELECTROMAGNÉTICAS CON LÍNEAS DE TRANSMISIÓN SUPERCONDUCTORAS

Amplificación es requerida para detectar pequeñas señales de microondas. Una nueva tecnología prometedora para conseguir amplificación con ruido cuánticamente-limitado es el *amplificador paramétrico de onda-viajera e inductancia cinética* (KI-TWPA). A través de este dispositivo superconductor se obtiene amplificación desde una ecuación de onda no-lineal de corriente pasando por un proceso de mezclado-de-ondas donde una señal de bombeo y una objetivo son inyectadas. Sin embargo, las ecuaciones de amplitud usadas para diseñarlos están incompletas. De hecho, estas no consideran completamente la naturaleza compleja de las constante de propagación e impedancia característica, relevantes en TLs periódicas. Estos problemas son abordados en esta tesis para mejorar el proceso de diseño de KI-TWPAs. Primero, el método-de-múltiples-escalas es explicado y aplicado a la ecuación de onda no-lineal en mezclado-de-cuatro-ondas. Como resultado, diferentes modelos de ecuaciones de amplitud son derivados, junto con el surgimiento de las señales *ociosa* y tercer-armónica del bombeo. Se demuestra que la primera es requerida para amplificar, mientras que la última es indeseada. Además, la discordancia total en fase entre las señales objetivo, ociosa y bombeo, es identificada como la principal factor de amplificación. Tras esto, resultados de simulación con cada modelo son mostrados para diferentes diseños, presentando una guía de diseño.

ABSTRACT OF THE THESIS TO OPT
FOR THE DEGREE OF MASTER IN ENGINEERING SCIENCES, MENTION IN ELECTRICAL ENGINEERING
BY: JAVIER ALEJANDRO CARRASCO ÁVILA
DATE: 2022
THESIS ADVISOR: FAUSTO PATRICIO MENA MENA
THESIS CO-ADVISOR: CLAUDIO MOISÉS FALCÓN BEAS

PARAMETRIC AMPLIFICATION OF ELECTROMAGNETIC SIGNALS WITH SUPERCONDUCTING TRANSMISSION LINES

Amplification is required to detect small microwave signals. One new promising technology to achieve large amplification with quantum-limited noise is the *kinetic inductance traveling-wave parametric amplifier* (KI-TWPA). Through this superconductor device, amplification is obtained from a non-linear current wave equation undergoing a wave-mixing process where a pump and a target signals are injected. However, the amplitude equations used to design them are not complete. Indeed, they do not fully consider the complex nature of the propagation constant and characteristic impedance, relevant in periodic TLs. These two problems are tackled in this thesis with the goal of unveiling the optimal design process for KI-TWPAs. Firstly, the *multiple-scales-method* is explained and applied to the non-linear wave equation in four-wave-mixing. As a result, different models of amplitude equations are derived, together with the emergence of the *idler* and third pump's harmonic signals. It is demonstrated that the former is required in order to obtain amplification, while the latter is undesired. Furthermore, the total phase mismatch between the target, idler, and pump signals is identified as the main factor for achieving amplification. Thereafter, simulations results with each of the models are shown for different designs, from which a guide for optimal design is presented.

A mis padres, por su apoyo infinito que me impulsó a seguir mi propio camino.

Agradecimientos

El camino que he recorrido para desarrollar esta tesis no habría sido un viaje tan ameno de no ser por grandes personas que me han acompañado en estos años. Tanto familia como amistades y colegas, todos han significado mucho para mí y es mi placer dejar registrados aquí mis agradecimientos.

Primero que todo, agradezco a mis profesores guía y co-guía, Patricio y Claudio, respectivamente, por su alta dedicación y comprensión. Pero, principalmente, agradezco a Patricio por haber mostrado gran empatía, lo que me permitió seguir adelante con este proyecto incluso durante los momentos difíciles. También quiero aprovechar de agradecer el alto entusiasmo y tiempo entregados por Patricio en cada uno de los cursos que dicta, varios de los cuales yo presencié como alumno y como profesor auxiliar, pues son motivantes esenciales en la carrera de cualquier estudiante. Sin duda fueron muy relevantes para mi formación. Además, agradezco a mi colega del grupo de investigación, Daniel, por siempre estar interesado, tanto a nivel conceptual fundamental como práctico, en los estudios de investigación compartidos y discutidos con mucha riqueza durante el desarrollo de mi tesis.

Por supuesto, agradezco a todos mis amigos de la universidad, con quienes no sólo he disfrutado buenos momentos; de diversión, relajación, juegos, viajes, etc.; sino que también he podido conversar sobre asuntos científicos de física e ingeniería en diversas especialidades, lo que ha sido grato, motivante y, además, ayudado a la generación de nuevas ideas. Mención especial para Samuel, Kevin, Martín, Néstor, Richard, Albert y Diego Gallardo, todos "unas máquinas" en lo que se dedican y con quienes ha sido muy grato e interesante compartir. También gracias a Paloma, por haber sido siempre una gran amiga en todos los momentos, altos y bajos a lo largo de esta gran travesía. Pero, por sobre todo, agradezco a "Los Bellos"; i.e. a Óscar, Fernanda, Cristóbal, Diego, Mauricio, Catalina, Alfredo, Alonso, Nicolás, Vicente "*vegan*" y Vicente; sin quienes el estrés de la universidad no habría sido posible sobrellevar, porque sólo es posible cumplir con un gran desafío si va acompañado de momentos de desestrés, y con ellos no sólo he podido "pasarla bien", sino que también me han dado un hogar dentro de la universidad y más allá. En especial, gracias a quienes me apoyaron durante los momentos más difíciles.

Finalmente quiero agradecer a mi familia, que ha sido un pilar fundamental durante todos mis estudios y mi trabajo. A mis hermanos Andrés y Nathaly con quienes siempre puedo contar, relajarme y disfrutar; así como a mis padres que me han apoyado en absolutamente todo y con gran fuerza, sin lo cual, jamás habría podido seguir mi propio camino para descubrir mi pasión por la física y por la ingeniería.

Table of Content

List of Tables

List of Figures

Nomenclature

α	Attenuation constant
β	Wavenumber
η	Characteristic impedance
γ	Propagation constant
$\mathcal{L}$	Differential operator acting on a linear term
$\mathcal{N}$	Differential operator acting on a non-linear term
ν	Frequency
ω	Angular frequency
C	Capacitance per unit length
G	Conductance per unit length
I	Electric current
L	Inductance per unit length
R	Resistance per unit length
r	Real part of η
t	Time variable
V	Electric voltage
x	Imaginary part of η
Y	Shunt admittance
Z	Series impedance
z	Distance variable

Chapter 1

Introduction

Many modern technologies work through propagation of electromagnetic signals that are detected by components. Although, due to the finite sensitivity of these components, the detection can only be achieved for signals with a minimum amplitude. In order to detect signals with smaller amplitude than this minimum, the signal must be previously amplified by another component (an amplifier). Therefore, the design and fabrication of amplifiers is key to extend the use of these technologies, ranging from astronomical instrumentation and quantum computing to cellphones and classical computers.

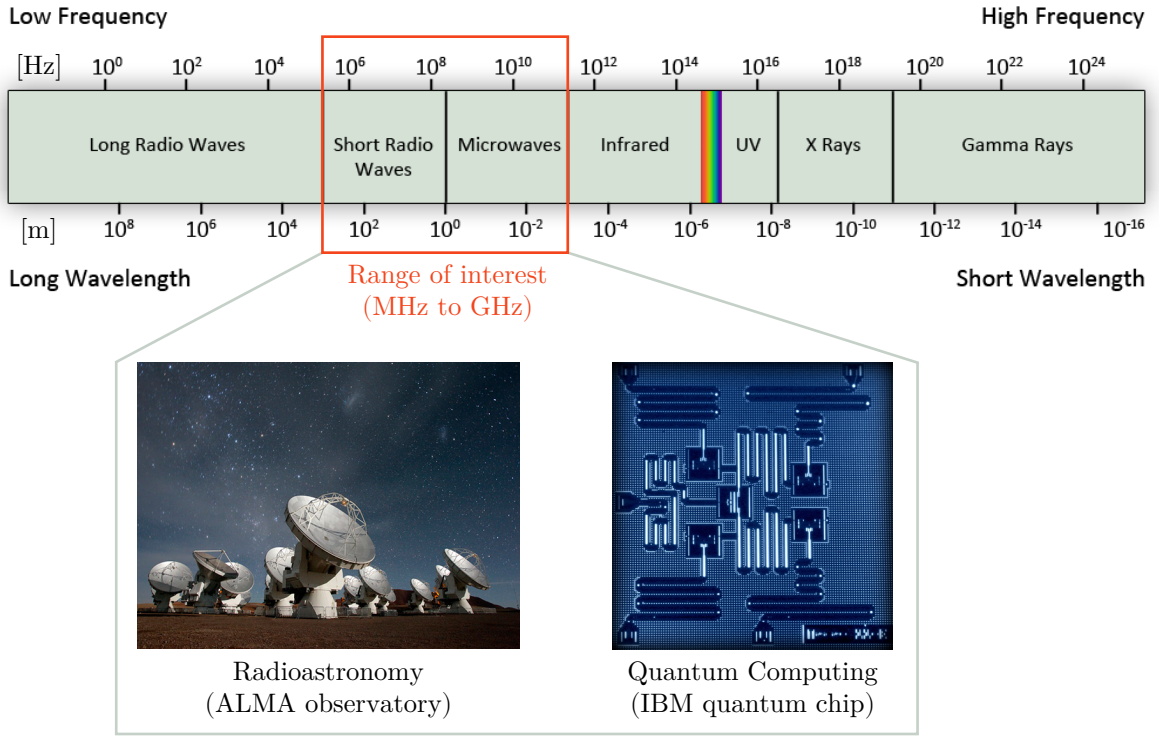

Figure 1.1: Electromagnetic spectrum (top) and two examples where the range of MHz-GHz frequencies are detected for scientific and technological purposes (bottom).

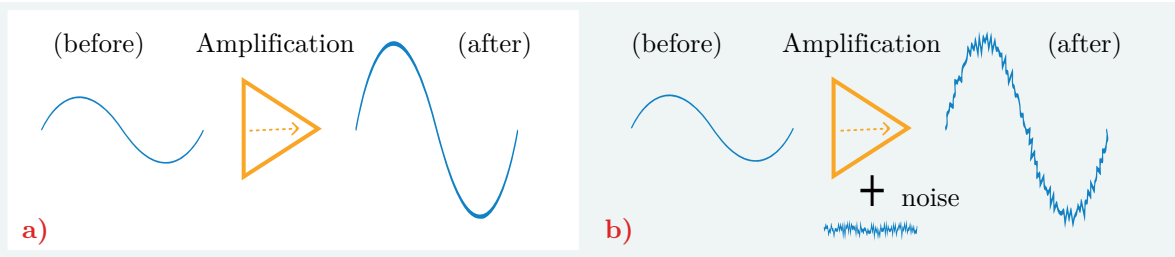

Figure 1.2: Amplification of a signal through a noisless (a) and noisy (b) amplifier.

To detect electromagnetic signals, different technologies are used depending on the signal's frequency, translating into different challenges to successfully design an amplifier. Based on this, the electromagnetic spectrum is separated in technological ranges as shown in Figure 1.1. In this thesis, the focus is on the short radio (MHz), microwave (GHz), and low THz frequencies.

An important general problem to solve in the signal amplification process is that the amplifier adds noise to the original signal as shown in Figure 1.2 producing loss of information. Therefore, the search for a physical system that allows amplification with the lowest possible addition of noise is required in order to improve the amplification technology. Furthermore, a good amplifier must have a large amplitude amplification (i.e. large gain) and work for a wide range of frequencies of interest (i.e. broad fractional bandwidth). These criteria are used to conclude on which amplification technology is better for amplification.

1.1 Radio and microwave amplification technologies

For radio and microwave amplification, semi- and super-conductor technologies are used. A comparison between the best current available technologies can be done by considering the main **amplification figures of merit**:

- **Noise temperature** (T_{n}) as the measure of noise to minimize. Without manipulation of the quantum state of the electromagnetic signal, it can not be smaller than $T_{\mathrm{n-sq}}$, called the standard quantum limit.

- **Power Gain** $G \equiv \frac{|A_{\mathrm{after}}|^2}{|A_{\mathrm{before}}|^2} \equiv 20\log_{10}(\frac{|A_{\mathrm{after}}|}{|A_{\mathrm{before}}|})$ dB, where A_{after} and A_{before} are the amplitudes of the signal after and before passing through the amplifier, respectively.

- **Fractional bandwidth** $B_f \equiv \frac{2(\nu_{\mathrm{max}}-\nu_{\mathrm{min}})}{\nu_{\mathrm{max}}+\nu_{\mathrm{min}}}$, where ν_{max} and ν_{min} are respectively the maximum and minimum frequencies around the maximum gain G_{max} where the gain dropped to[1] $G_{\mathrm{max}}/2$, meaning approximately a -3 dB drop for the quantity expressed in decibels.

The best semiconductor technology is the high-electron-mobility transistor (HEMT) achieving $T_{\mathrm{n}} \geq 3T_{\mathrm{n-sq}}$ for low frequencies but increasing rapidly as the frequency of the target signal ν_s increases [7]. Towards a solution to this noise problem, super-conductor technology

[1] For this reason, B_f is also called *fractional full width at half maximum*.

has shown to be promising. The best superconducting technologies are Josephson resonators, superconducting quantum interference devices (SQUIDs), superconducting qubits, transmission line resonators, and Josephson and kinetic inductance traveling-wave parametric amplifiers (KI-TWPAs) [8–19]. However, only the last two work in a broad B_f while reaching $T_{\mathrm{n}} \approx 3T_{\mathrm{n-sq}}$ and presenting large G. KI-TWPAs are better because they allow maximum total currents of the order of mA, three orders of magnitude larger than the Josephson traveling-wave parametric amplifiers [15].

Therefore, KI-TWPAs are a promising solution towards the design of amplifiers with the lowest possible addition of noise. It is for this reason that they are the devices analyzed in this thesis.

1.1.1 KI-TWPAs

A KI-TWPA consists of an electromagnetic transmission line (TL) in which instead of a normal conductor there is a superconductor. The result is that the inductance per unit length of the TL depends on the injected current because kinetic inductance (originated by the inertia of the current carriers) is added to the geometric one. This modifies the wave-equation of the current through the TL by adding a non-linear term, which allows mixing of amplitudes when more than one monochromatic signal is injected [5, 20]. Hence, it is possible to amplify the amplitude corresponding to ν_{s} if other signals, called pumps, are simultaneously injected. The case of only one single pump signal with frequency ν_p is analyzed in this thesis.

Different geometries and materials may be used to fabricate these transmission lines. The most common geometry up to date has been the coplanar waveguide (CPW), but the microstrip (MS), and the inverted microstrip (IMS) geometries have also been used. These three geometries are depicted in Figure 1.3. To choose the materials of the TL, the following criteria must be considered:

- **Superconducting strip**: To warrant a large kinetic inductance and hence large amplification, a superconductor with large normal-state resistance must be selected. The normal-state resistance corresponds to the resistance of the material at the critical temperature just before entering the superconducting state.

- **Substrate**: Due to the coupling of microwave radiation to a bath of two-level state defects in the dielectric, its loss tangent increases at low excitation voltages and temperatures at which the KI-TWPA operates. Measurements at this regime show that crystalline materials are the least lossy when compared to other materials [21]. However, an interesting material to explore is hydrogenated amorphous silicon (a-Si:H), which besides having the lowest loss tangent among other amorphous materials, it is easier to work with when fabricating devices [21].

The first KI-TWPA was presented in [20]. The device consisted on a long dispersion-engineered (a method used to avoid third and higher harmonics of the pump frequency ν_p) CPW of niobium titanium nitride (NbTiN) deposited over crystalline silicon. It covered the frequency range from 6 to 16 GHz with a gain of around 12 dB. Despite this excellent result, there were some problems with this implementation [14, 22, 23]:

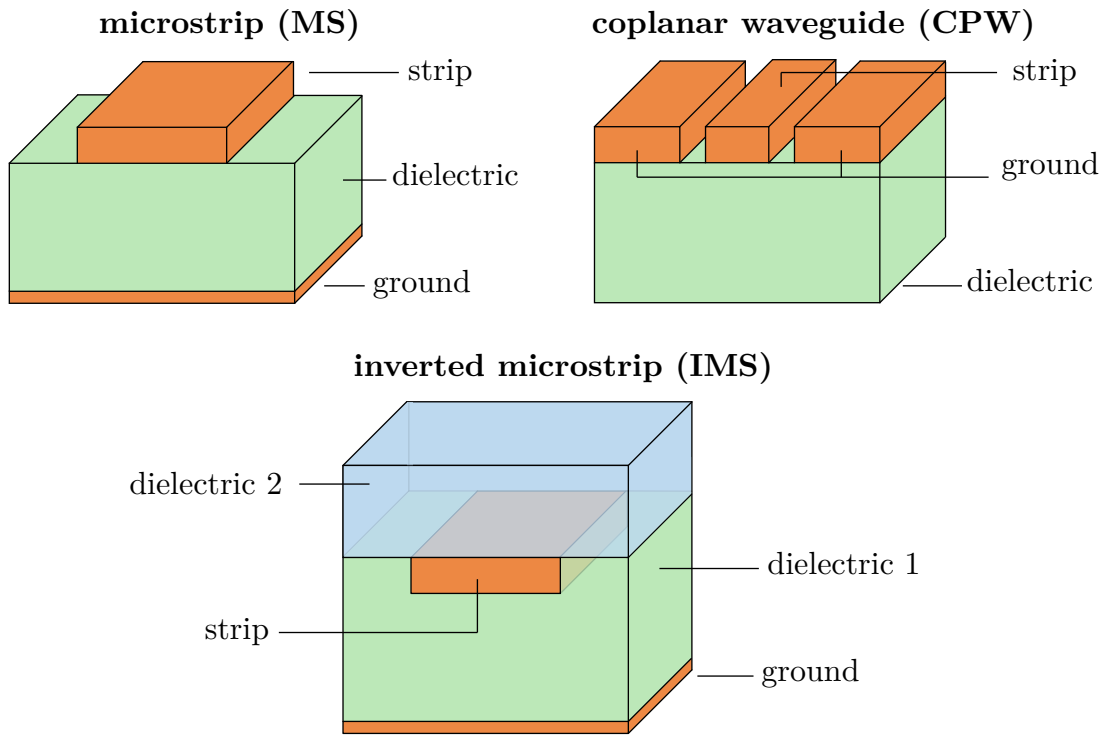

Figure 1.3: The most relevant transmission line geometries used for KI-TWPAs.

i) Selecting a CPW line has the advantage of an easier fabrication than MS lines, but limits the impedance that can be achieved. This first implementation had a characteristic impedance of 300 Ω which needs a matching to the 50 Ω input and output ports. This seemed to be the origin of large ripples seen in the transmission curve.

ii) A larger real characteristic impedance means that larger dissipation occurs which could warm up the device introducing noise.

iii) The device features a very long transmission line of about 0.8 m which makes it prone to defects along the transmission line.

Few other implementations, always below 16 GHz, have been reported since the introduction of the KI-TWPAs [14, 22–27]. The first implementations replicated the original concept verifying the potential and the problems of the device [23, 25]. Later, some modifications were introduced in the attempt of overcoming the main problems of the first ones.

One of the modifications introduced was changing the CPW for an IMS of NbTiN which allows, in principle, obtaining a 50 Ω line [24]. The conducting strip was deposited over the substrate, silicon dioxide (SiO_2) was deposited on top of the strip and finally the ground plane was deposited over the SiO_2 layer. The device was measured at 4 K showing some parametric amplification. Additionally, simulations showed that ripples in the gain may be present in the device even if the input and output ports are perfectly matched. This effect appears to be due to the non-homogeneous dispersion of the transmission line.

Two additional implementations have achieved KI-TWPAs with a 50 Ω transmission line and

a reduced length [14, 22]. One implementation reduced the necessary length by coupling the transmission line to quasi-fractal line-to-ground capacitors [22]. In this way the line achieves enhanced inductance and capacitance per unit length which translates into a parametric gain of 6 dB for just 10 cm of transmission line. A disadvantage of this implementation is the increased complexity of the fabrication process. The other implementation achieved the reduction in length by using a lumped-element transmission line fabricated as interdigitated slotline (another type of TL) elements [14]. A large gain was obtained with reduced ripples and lower pumping power. However, this kind of PAs are restricted in their size reduction, and can only be used at low frequencies since a chain of lumped elements can only be used as a TL at frequencies below $\nu_c = (\pi\sqrt{lc})^{-1}$, where l and c are the inductance and capacitance of the lumped elements, respectively.

The aforementioned KI-TWPAs were demonstrated for four-wave-mixing (FWM) where, besides the pump and target signals, an idler signal is naturally produced throughout the amplification process. Other signals and harmonics are also generated, but those do not contribute positively to the gain of the target signal and are either eliminated by engineering or neglected due to being too small. However, it has been demonstrated that the CPW KI-TWPA can also be used in a three-wave-mixing scheme by feeding the device with a DC current [26]. One of the most important advantages of this scheme is that it needs a reduced power of the pumping signal, decreasing dissipation and, hence, has the potential of reaching a reduced noise.

The CPW KI-TWPA has also been implemented using a monocrystalline NbTiN film deposited over a magnesium oxide (MgO) substrate [27]. It was demonstrated that such a device has a larger variation of the kinetic inductance when compared to a polycrystalline film. In this way, a larger gain could be achieved in principle, although gain measurements were not performed.

1.2 Mathematical model of KI-TWPAs

In order to design KI-TWPAs with large power gain and large fractional bandwidth, a non-linear wave equation for the electric current must be solved. In the literature, this is done by approximating the process of amplitude gain as a dynamical evolution occurring at a much larger length scale than the wavelength of the involved signals. Within this approximation, a set of non-linear amplitude equations is obtained [20, 28, 29]. This set of equations is usually too hard to solve analytically, and is hence solved numerically, at least for the general case of FWM.

The derivation of the amplitude equations in a FWM process has been done in the optics literature for waves traveling through fiber optics [28, 29]. However, in the KI-TWPAs literature, a similar set of amplitude equations has been used without reporting a complete formal derivation. This is a problem, since the derivations used in optics make use of properties of the electric and magnetic fields that do not apply in radio nor microwave TLs. In particular, the non-linear term in KI-TWPAs arises from the superconductor, and hence, it is in principle a different non-linearity than the Kerr materials used in optics.

Moreover, the amplitude equations of KI-TWPAs in the current literature neglect the atten-

uation constant (representing losses by reflections and dissipation) and the imaginary part of the characteristic impedance of the TL [20]. This is done with TL designs constituted by periodic elements where such approximations are wrong near the stopbands. Despite this, the equations are applied at frequencies near the stopbands, ignoring the problem. An attempt to introduce losses in the process has been reported in [15], but there are still some approximations not justified and not valid near the stopbands. Furthermore, there is no mathematical explanation of how the equations were obtained, making it impossible to re-derive the results.

It is concluded that the mathematical model used so far for KI-TWPAs is incomplete. Therefore, work toward solving this is required in order to understand better how amplification is obtained in KI-TWPAs, which would enable better designs of this type of parametric amplifiers.

In this thesis, this problem is tackled by formally solving the non-linear wave equation with a formal perturbative model called "multiple scales method", widely used in mathematical non-linear physics, and specially useful in traveling-wave equations [1, 29, 30].

1.3 Identification of the problem

The identified specific problem is:

- The theoretical study of the amplification process in KI-TWPAs is incomplete. Dissipation and reflections are not well understood and the deduction of the amplitude equations used to calculate the gain is unclear in the literature.

Therefore, to solve this problem, two specific solutions are developed as the core of this thesis:

- Study and apply the multiple scales method to solve non-linear wave equations.
- Simulate the parametric amplification process described by the amplitude equations.

1.4 Hypothesis

The hypothesis of this work is:

- By using the multiple-scales method of mathematical non-linear physics, appropriate equations to calculate the gain can be formally obtained.
- This can be done with and without losses (dissipation and reflections), allowing to better understand the amplification process of KI-TWPAs and enhance future designs.

1.5 Objectives of the thesis

The objectives to accomplish with this solution are:

- **General objective:** Develop a new theoretical framework to simulate and design KI-TWPAs.

- **Specific objective 1:** Realize a formal mathematical deduction of the amplitude equations including dissipation using the multiple scales method.
- **Specific objective 2:** Model specific TLs with the derived equations, comprehending how to change the design parameters in order to enhance the amplifier's performance in terms of gain and fractional bandwidth.

1.6 Outline of the thesis

In this chapter, the general problems associated with amplification of electromagnetic signals have been introduced. An overview of the technological advances in this regard has been explained, justifying the KI-TWPAs as promising devices for amplification. A specific problem in this research area has been identified and a specific solution has been proposed to be developed throughout the current thesis.

In order to accomplish the proposed solution, several fundamental concepts must be understood. These are presented in chapter 2. Later, in chapter 3, the method of multiple scales is used to formally derive different models of the amplitude equations from which the gain of the target signal is calculated. These results are applied in chapters 4, 5, and 6, where simulations for each model in different interesting cases are performed and analyzed.

In chapter 4 a deep analysis of the behavior of the different models in various cases is performed for a design with a CPW similar to the one fabricated in [20], helping to understand what are the optimal conditions for amplification of the target signal. From that knowledge, a design guide is explained for microstrip in chapter 5, showing the generality of the conclusions obtained in chapter 4, not constrained to CPW designs. Finally, chapter 6 shows results for a design with an artificial-CPW line fabricated by colleagues in the research group. Predictions to measurements are obtained, which are to be tested in the near future to validate the mathematical models developed in this thesis.

Chapter 2

Theoretical framework

The fundamental theoretical concepts to understand KI-TWPAs and the results developed in this thesis are explained in this chapter. First of all, the KI-TWPAs are devices that generate amplification of target signals through a so called *parametric amplification* process. Hence, understanding the meaning of this process is required, and it is the objective of section 2.1, where the concept is explained in general mathematical terms. Secondly, KI-TWPAs are superconducting devices. For this reason, a basic understanding of superconductors is needed to be able to correctly calculate the conductivity. This is explained in section 2.2. Additionally, KI-TWPAs are electromagnetic transmission lines. Therefore, in section 2.3 the basics of TL theory are explained in order to, later, merge with the superconductor properties and derive the non-linear wave equation for the electric current through KI-TWPAs, explaining how to correctly calculate the TL parameters for a general geometry, focusing in the calculations for MS and CPW. A non-linear relation between wavenumber and frequency is required to achieve amplification in KI-TWPAs. To do this, *dispersion engineered TLs*, also called *Floquet TLs*, are used and explained at the end of section 2.3. These TLs also have the benefit that, by the presence of stopbands, allow the suppression of undesired harmonics generated throughout the *four-wave-mixing* (FWM) process in KI-TWPAs. The latter is briefly explained in 2.4. Finally, the calculation of the gain of the target signal along KI-TWPAs is performed in the current literature by using amplitude equations whose deduction is not explicitly given. Hence, a mathematical framework that allows to obtain amplitude equations from the non-linear wave equation of KI-TWPAs is presented in section 2.5. This framework, called *method of multiple scales*, is the core for the development of the current thesis.

2.1 Parametric Amplification

This thesis is concerned with electromagnetic waves, which are oscillations in the electromagnetic field propagating through space-time. In particular, the focus in this thesis is about amplifying these oscillations. A way of achieving this amplification is by periodically changing a physical parameter of the system. Equations in which this happens are called **parametric equations**. This section presents the key features of this type of equations with a simple general example.

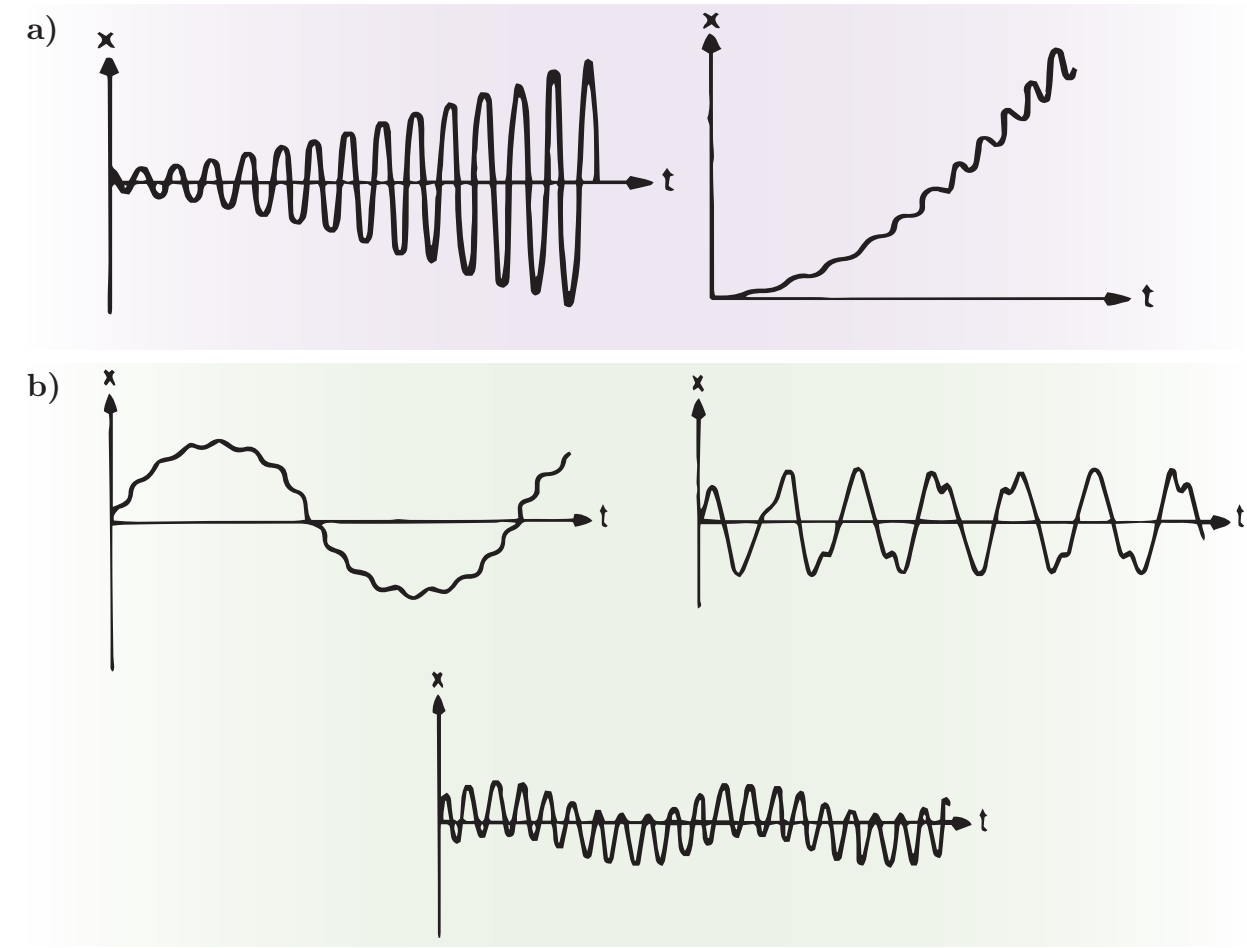

Figure 2.1: (a) Unbounded and (b) bounded solutions of the Mathieu equation. From the perspective of signal amplification, the cases of (a) are interesting: the left plot shows slow amplitude growth of a fast oscillating signal, and the right plot shows fast amplification of the mean value (addition of a "DC" component) as well as slow amplitude growth. These two cases represent parametric amplification. Image adapted from [1].

The simplest differential equation with periodic coefficients is the **Mathieu equation** [30,31],

$$\frac{\mathrm{d}^2x}{\mathrm{d}t^2} + (a - 2q\cos(2t))x = 0, \tag{2.1}$$

which can physically represent a swing with variable rope length or an inductance-capacitance electric circuit with variable distance between capacitor parallel plates. In any case, equation 2.1 is a harmonic oscillator with a modified coefficient, where x is the oscillating variable whose amplitude is to be amplified, t is the dimensionless evolution parameter of the equation (e.g. time or position), and $(a - 2q)$ is the physical parameter of the harmonic oscillator equation that is being periodically changed through the term $\cos(2t)$.

In order to achieve amplification with a parametric equation, the frequency of the external excitation must be carefully tuned to a resonant case. When this is done, **parametric resonance** occurs. In the case of Mathieu equation 2.1, parametric resonance takes place,

for any value of $q \in \mathbb{R}$, when the external excitation frequency equals $n/2$ times the natural frequency of the system, where $n \in \mathbb{Z}$. Nonetheless, parametric resonance can still happen for others frequencies depending on the value of q.

Parametric resonance, also known as **parametric amplification**, **parametric excitation** or **parametric pumping**, differs from forcing the system. In the former, the action appears as a time varying modification on a system's parameter in a homogeneous differential equation, while in the latter, the action appears as an inhomogeneous term added to the original equation. Furthermore, parametrically excited systems can produce a large response when the frequency of the excitation is away from the natural frequency of the system [30], which is not possible in forced systems.

The Mathieu equation 2.1 does not describe a complete physical system as no compensating energy-loss mechanism is involved. Hence, the oscillation amplitude grows exponentially when parametric resonance occurs, as shown in Figure 2.1.a. These are the type of solutions desired for amplification of signals in the physical process of FWM studied in this thesis, as opposed to the ones of Figure 2.1.b. Nonetheless, the case of FWM is more complex than equation 2.1, because it also describes the energy source (the pump) and hence the solution should not grow indefinitely. These additional complications are studied in section 2.3, where FWM is described as a parametric equation.

The conclusion from this section is that a parametric pump can be used to amplify the original oscillation, and hence, an equation like equation 2.1 is useful for the purpose of amplifying small electromagnetic signals, which is the matter of study in this thesis.

2.2 Superconductors

Superconductivity is an electrical state of matter that can be achieved through an electrical phase transition in conductors. Therefore, specific conditions of temperature and electric current must be fulfilled in order to keep the superconducting state for a fixed condition of pressure. The temperature T and current I are upper bounded by a **critical temperature** T_c, and **critical current** I_c, respectively. Hence, as long as $T \leq T_c$ and $I \leq I_c$, the material is in a superconducting state [2]. Unfortunately, the typical values of T_c are very small, around a few K, corresponding to the so called cryogenic temperatures. This makes the experimental realization of superconductors a hard task, which requires the use of complex cooling techniques developed along several years. There are some superconductors at higher temperatures, with $T_c \approx 160$ K [2], or even $T_c \approx 287$ K as reported in [32], close to room temperature (300 K). Nonetheless, these high temperature superconductors require extremely large values of pressure (267 GPa for the latter [32]), which is in general much more unpractical than using cooling systems like cryogenic fridges.

In superconductors, the carriers of electric current are not individual electrons, but instead Cooper pairs formed by couples of electrons paired together [2]. As electrons are spin-$\frac{1}{2}$ particles (hence, fermions), by addition of angular momenta the Cooper pairs can be spin-0 or spin-1 particles (hence, bosons). Having bosons instead of fermions as the carriers of current, means that Pauli's exclusion principle is avoided, implying that all Cooper pairs can be in the same quantum state. In particular, they can be in the lowest energy one, reducing

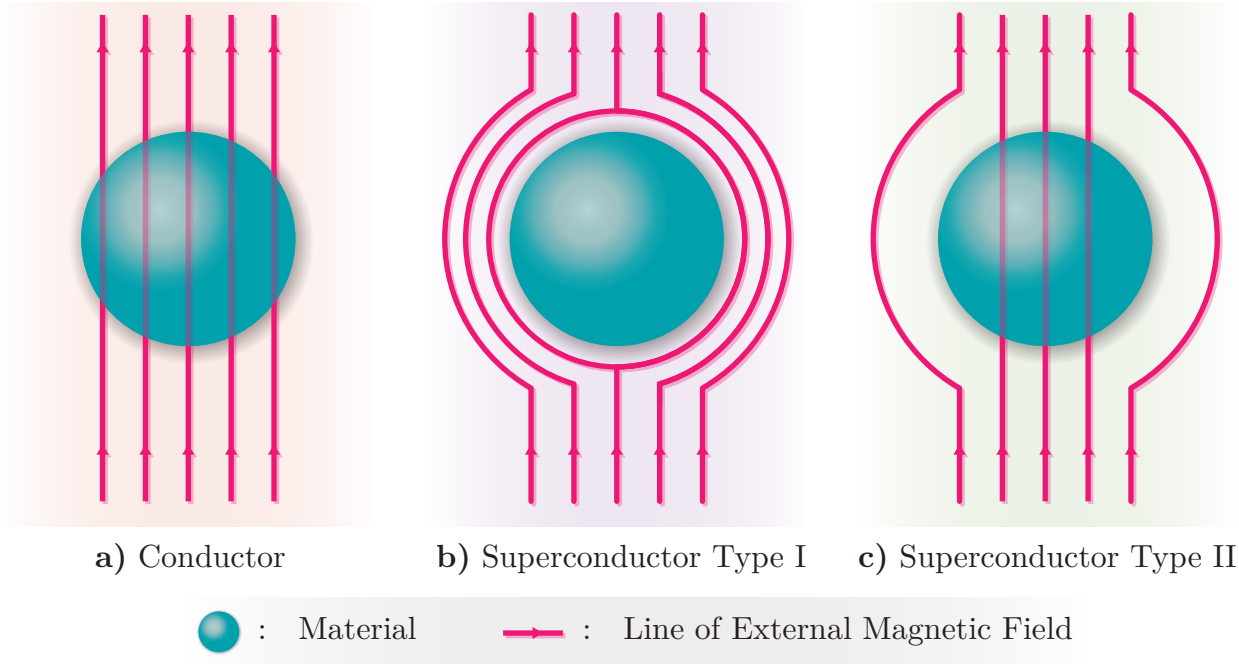

Figure 2.2: Material capable of conducting electricity and how to differentiate them based on the action of an external magnetic field. The magnetic field lines coming from external source always penetrate in the case of a normal conductor (a), are always repelled by a superconductor of type I (b), and can be partially repelled by a superconductor of type II (c) while locking some lines inside of it depending on the temperature conditions [2]. In this thesis we use superconductors type I in our modeling.

electrical resistance down to, in theory (unless quantum fluctuation are taken into account), zero at 0 K [2].

There are different types of superconductors, based on how they interact with external magnetic fields, as depicted in Figure 2.2. In KI-TWPAs, **type I superconductors** are used, and hence, are the ones considered throughout this thesis. Henceforth, when referring to superconductors, it is referred to type I superconductors, unless explicitly expressed otherwise.

Since the carriers of electric current are different in superconductors than normal conductors, the **complex conductivity**

$$\sigma = \sigma_1 - \mathrm{j}\sigma_2, \tag{2.2}$$

must also be calculated differently. This calculation is performed by the **Mattis-Bardeen equations** [33, 34],

$$\frac{\sigma_1}{\sigma_N} = \frac{2}{\hbar\omega}\int_{\Delta_g}^{\infty}[f(E) - f(E+\hbar\omega)]\mathcal{D}(E)\mathrm{d}E + \frac{1}{\hbar\omega}\int_{\Delta_g-\hbar\omega}^{-\Delta_g}[1-2f(E+\hbar\omega)]\mathcal{D}(E)\mathrm{d}E, \tag{2.3}$$

$$\frac{\sigma_2}{\sigma_N} = \frac{1}{\hbar\omega}\int_{\max\{\Delta_g-\hbar\omega,-\Delta_g\}}^{\Delta_g}\frac{[1-2f(E+\hbar\omega)](E^2+\Delta_g^2+\hbar\omega E)}{\sqrt{\Delta_g^2-E^2}\sqrt{(E+\hbar\omega)^2-\Delta_g^2}}\mathrm{d}E, \tag{2.4}$$

where

$$\mathcal{D}(E) = \frac{E^2 + \Delta_g^2 + \hbar\omega E}{\sqrt{E^2 - \Delta_g^2}\sqrt{(E+\hbar\omega)^2 - \Delta_g^2}}, \tag{2.5}$$

$f(E,T)$ is the Fermi-Dirac distribution dependent of energy E and temperature T,

$$f(E,T) = \frac{1}{1 + \mathrm{e}^{E/(k_B T)}}, \tag{2.6}$$

Δ_g is the energy gap of the superconductor (null for normal conductors), and σ_N is the normal-state conductivity, which corresponds to the conductivity just above the critical current I_c, where the material leaves the superconducting state to become a normal conductor.

The Mattis-Bardeen equations are needed to calculate the TL parameters for a KI-TWPA. Therefore, they are used to perform all the simulations shown later in chapters 4, 5, and 6.

2.3 Transmission Lines

2.3.1 Basics

A general TL of length D, as depicted in Figure 2.3.a, can be described as a continuous series of infinitesimally small lumped-element circuits described by Figure 2.3.b, where R is the resistance per unit length due to losses in the conductors (with finite conductivity), C is the capacitance per unit length due to the close proximity between conductors, G is the conductance per unit length due to losses in the dielectric material between conductors, and L is the total self-inductance per unit length between the conductors [3]. These circuit elements are distributed along the entire TL. Therefore, this model is called **transmission line model of distributed elements**. Consequently, the equations for electric current I and voltage V through the TL are the **telegraph equations**,

$$\frac{\partial V}{\partial z} = -L\frac{\partial I}{\partial t} - RI, \tag{2.7}$$

$$\frac{\partial I}{\partial z} = -C\frac{\partial V}{\partial t} - GV, \tag{2.8}$$

where z is the position along the TL, and t is the time. These equations can be easily decoupled by deriving once with respect to z, obtaining the linear homogeneous wave equations

$$\left(\frac{\partial^2}{\partial z^2} - CL\frac{\partial^2}{\partial t^2} - (CR+GL)\frac{\partial}{\partial t} - RG\right) I = 0, \tag{2.9}$$

$$\left(\frac{\partial^2}{\partial z^2} - CL\frac{\partial^2}{\partial t^2} - (CR+GL)\frac{\partial}{\partial t} - RG\right) V = 0. \tag{2.10}$$

In general, the current and voltage waves travel as packages of monochromatic waves, each with a different frequency. In other words, a general wave of current or voltage is not monochromatic, meaning that it contains many relevant frequencies in its time-Fourier domain. Nonetheless, because equations 2.9 and 2.10 are linear, it is possible to solve them

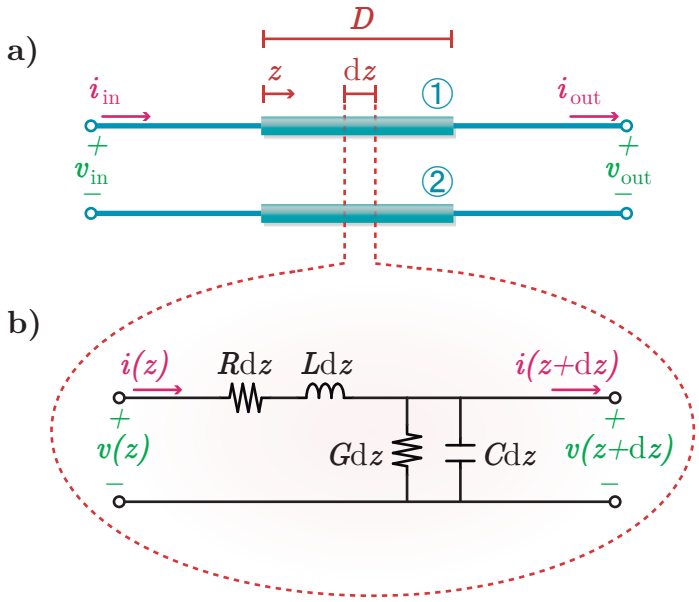

Figure 2.3: TL model of distributed elements. (a) A general transmission line of length D, where ① and ② are conductors at different electric potentials, allowing propagation of electromagnetic waves represented by waves of current $i(z,t)$ and voltage $v(z,t)$ across the line. (b) Zooming inside an infinitesimal portion dz of the line, circuit theory of lumped elements can be utilized as the wavelength is always much larger than dz obtaining the displayed equivalent circuit, where R, C, G, and L are the resistance, capacitance, conductance, and total self-inductance per unit length of the TL.

independently for each frequency component. Hence, for a given angular frequency ω, the solution is given by

$$I_\omega = \mathrm{Re}\{A_\omega^+ \mathrm{e}^{\mathrm{j}\omega t - \gamma_\omega z} + A_\omega^- \mathrm{e}^{\mathrm{j}\omega t - \gamma_\omega^* z}\}, \tag{2.11}$$

$$V_\omega = \mathrm{Re}\{B_\omega^+ \mathrm{e}^{\mathrm{j}\omega t - \gamma_\omega z} + B_\omega^- \mathrm{e}^{\mathrm{j}\omega t - \gamma_\omega^* z}\}, \tag{2.12}$$

where $A_\omega^{+(-)}$ and $B_\omega^{+(-)}$ are the complex amplitudes of current and voltage, respectively, traveling in the $+\mathbf{z}$ $(-\mathbf{z})$ direction; and γ_ω is the **propagation constant**, related to the TL parameters (R, G, L, C) by

$$\gamma_\omega = \sqrt{(R + \mathrm{j}\omega L)(G + \mathrm{j}\omega C)}. \tag{2.13}$$

Additionally, $A_\omega^{+(-)}$ and $B_\omega^{+(-)}$ are related between each other by

$$\frac{B_\omega^+}{A_\omega^+} = \frac{B_\omega^-}{A_\omega^-} = \eta_\omega, \tag{2.14}$$

where η_ω is the **characteristic impedance** of the TL, related to the TL parameters by

$$\eta_\omega = \sqrt{\frac{R + \mathrm{j}\omega L}{G + \mathrm{j}\omega C}}. \tag{2.15}$$

In general, γ and η (the ω subindex is dropped to simplify notation) are complex quantities,

$$\gamma = \alpha + \mathrm{j}\beta, \tag{2.16}$$

$$\eta = r + \mathrm{j}x, \tag{2.17}$$

where α is called **attenuation constant**, and β is the **wavenumber**. The real and imaginary parts of η (r and x, respectively) do not receive special names in the literature, but they are explicitly written here because this notation will be used throughout the rest of this thesis.

2.3.2 Geometries

Many different geometries to configure the two conductors and the intermediate dielectric material that define a TL (as depicted in Figure 2.3) can be realized. Two of the most used ones for KI-TWPAs are studied in this thesis: MS and CPW geometries, depicted in Figure 2.4. In a MS, the geometry is defined by the height h of the dielectric, the width w of the conducting strip, and the strip's thickness t, neglecting the thickness of the ground conducting plane. Similarly, in a CPW, the geometry is defined by the separation s between the central strip and the ground planes, the central strip's width w, and the thickness t of the conductors, considered equal for the grounds and the central strip.

Effective dielectric constant

Depending on the geometry used as TL, the effective dielectric constant for the waves propagating through the TL is not simply the complex dielectric constant ϵ_r of the dielectric material.

For a MS, the effective frequency-dependent dielectric constant is [35]

$$\tilde{\epsilon}_\nu = \left(\frac{\sqrt{\epsilon_r} - \sqrt{\epsilon_s}}{1 + 4F_1^{-1.5}(\nu)} + \sqrt{\epsilon_s} \right)^2, \tag{2.18}$$

where

$$F_1(\nu) = \frac{4h\nu}{c_0}\sqrt{\epsilon_r - 1}\left(\frac{1}{2} + \left(1 + 2\ln\left(1 + \frac{w}{h}\right)\right)^2\right), \tag{2.19}$$

and ϵ_s is the effective static dielectric constant given by [3]

$$\epsilon_s = \frac{\epsilon_r + 1}{2} + \frac{\epsilon_r - 1}{2\sqrt{1 + 12\frac{h}{w}}}. \tag{2.20}$$

Hence, the **complex effective frequency-dependent dielectric constant** is

$$\epsilon_\nu = \tilde{\epsilon}_\nu(1 - \mathrm{j}\tan\delta), \tag{2.21}$$

where $\tan\delta$ is the loss-tangent of the dielectric, which accounts for electromagnetic losses in the dielectric material [3].

For a CPW, for frequencies below the order of THz, the frequency dependence of the dielectric constant can be neglected [36]. Therefore, the **complex effective dielectric constant** is [36, 37]

$$\epsilon = \tilde{\epsilon}(1 - \mathrm{j}\tan\delta), \tag{2.22}$$

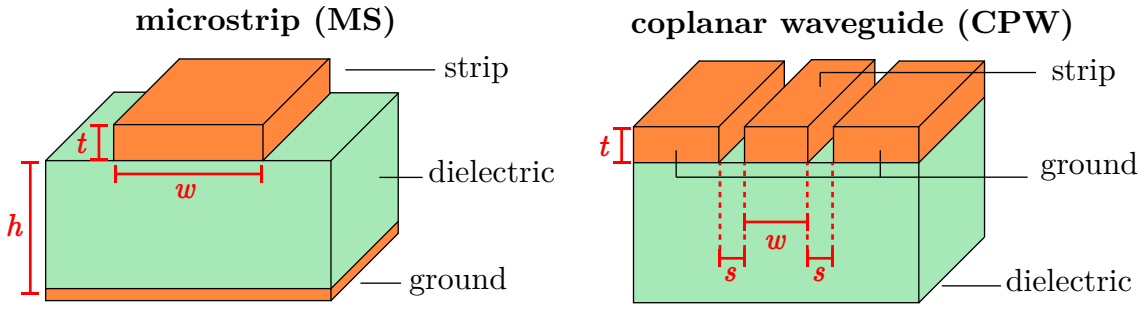

Figure 2.4: Transmission line geometries used for KI-TWPAs in this thesis.

where

$$\tilde{\epsilon} = \frac{\epsilon_r + 1}{2}. \tag{2.23}$$

Geometric factors

Two purely geometric factors are required to later calculate the transmission line parameters: g_1 and g_2. The former is characteristic of the field distribution external to the TL, and is related to the quasi-static capacitance of the TL [38] by

$$g_1 = \frac{\epsilon_0}{C_{\text{vac}}}, \tag{2.24}$$

where C_{vac} is the *vacuo* capacitance when the dielectric and substrate of the TL have their dielectric constants set to 1, as if replaced by empty space.

The second geometric factor, g_2, is characteristic of the field penetration into a superconductor (hence, $g_2 = 0$ for normal conductors) and is calculated for the n-th surface as [38]

$$g_{2,n} = g_1 \psi_n, \tag{2.25}$$

where

$$\psi_n = \frac{1}{2} \frac{\int_n |\mathbf{E}|^2 ds}{\int_{\text{ext}} |\mathbf{E}|^2 dA}, \tag{2.26}$$

and $\mathbf{E}$ is the electric field. The top integral of length element ds is along the cross-section of superconductor surface n, and the bottom integral of area element dA is across all area external to the superconductors (i.e. the infinite cross-sectional area, excluding the regions with superconductors).

Superficial impedance

From Figure 2.3.b, the series impedance Z and shunt admittance Y of a TL are defined by

$$Z = R + \mathrm{j}\omega L, \tag{2.27}$$
$$Y = G + \mathrm{j}\omega C. \tag{2.28}$$

The general forms of Z and Y are given by [38]

$$Z = \mathrm{j}(\beta_{\text{free}}\eta_{\text{free}})g_1 + 2\sum_n g_{2,n}Z_{s,n}, \tag{2.29}$$

$$Y = \mathrm{j}\frac{\beta_{\text{free}}}{\eta_{\text{free}}}\frac{\epsilon}{g_1}, \tag{2.30}$$

where β_{free} is the free-space wavenumber, η_{free} is the characteristic impedance of free-space, ϵ is the effective dielectric constant, and $Z_{s,n}$ is the surface impedance of superconductor surface n given by [38]

$$Z_s = \sqrt{\frac{\mathrm{j}\omega\mu_0}{\sigma}}\coth\left(\sqrt{\mathrm{j}\omega\mu_0\sigma}t_{\text{SC}}\right), \tag{2.31}$$

where t_{SC} is the thickness of the homogeneous superconducting film, and σ is the conductivity calculated in equation 2.2.

Calculation of geometric factors for a MS

For a microstrip of strip width w, substrate height h and metal thickness t_{SC}, the geometric factors are calculated as [38]

$$g_1 = \frac{\pi}{2}\frac{1}{\ln(2r_b/r_a)}, \tag{2.32}$$

$$g_2 = g_1\frac{1}{K_{\text{MS}}}\left(\mathcal{I} + \frac{\pi}{2}\right), \tag{2.33}$$

where

$$\mathcal{I} = \ln\left(\frac{2p + 2\sqrt{p(1-r_a)(p-r_a)} - (p+1)r_a}{r_a(p-1)}\right), \tag{2.34}$$

$$K_{\text{MS}} = \begin{cases} 2h\ln(r_b/r_a) & \text{if} \quad w/h < 2 \\ 2h\ln(2r_b/r_a) & \text{otherwise} \end{cases}, \tag{2.35}$$

$$\ln(r_a) \approx -1 - \frac{\pi w}{2h} - \frac{p+1}{\sqrt{p}}\tanh^{-1}\frac{1}{\sqrt{p}} - \ln\left(\frac{p-1}{4p}\right) \tag{2.36}$$

$$r_b \approx \begin{cases} r_{bo} & \text{if} \quad w/h \geq 5 \\ \tilde{r}_{bo} & \text{otherwise} \end{cases}, \tag{2.37}$$

$$r_{bo} = \Lambda + \frac{p+1}{2}\ln\Gamma, \tag{2.38}$$

$$\tilde{r}_{bo} = r_{bo} - \sqrt{(r_{bo}-1)(r_{bo}-p)} + (p+1)\tanh^{-1}\sqrt{\frac{r_{bo}-p}{r_{bo}-1}} - 2\sqrt{p}\tanh^{-1}\sqrt{\frac{r_{bo}-p}{p(r_{bo}-1)}} + \frac{\pi w}{2h}\sqrt{p}, \tag{2.39}$$

$$\Lambda = \sqrt{p}\left\{\frac{\pi w}{2h} + \frac{p+1}{2\sqrt{p}}\left[1 + \ln\left(\frac{4}{p-1}\right)\right] - 2\tanh^{-1}\frac{1}{\sqrt{p}}\right\}, \tag{2.40}$$

$$\Gamma = \max(\Lambda, p), \tag{2.41}$$

$$p = 2b^2 - 1 + 2b\sqrt{b^2 - 1}, \tag{2.42}$$

$$b = 1 + \frac{t_{\mathrm{SC}}}{h}. \tag{2.43}$$

Calculation of geometric factors for a CPW

For a CPW of inner strip width $w = 2a$, ground plane separation $w + 2s = 2b$ and thickness t_{SC}, the geometric factors are given by [38]

$$g_1 = \frac{K(k')}{4K(k)}, \tag{2.44}$$

$$g_{2,l} = g_1 \frac{1}{8K(k)K(k')(1-k^2)} \left[\frac{\pi}{a} + \frac{1}{a} \ln \frac{8a}{d_{\mathrm{SC}}} + \frac{1}{b} \ln \frac{b-a}{b+a} \right], \tag{2.45}$$

$$g_{2,g} = g_1 \frac{1}{4K(k)K(k')(1-k^2)} \left[\frac{\pi}{b} + \frac{1}{b} \ln \frac{8b}{d_{\mathrm{SC}}} + \frac{1}{a} \ln \frac{b-a}{b+a} \right], \tag{2.46}$$

where

$$d_{\mathrm{SC}} = \frac{t_{\mathrm{SC}}}{\pi}, \tag{2.47}$$

$$k = \frac{w_1}{w_2}, \tag{2.48}$$

$$k' = \sqrt{1 - k^2}, \tag{2.49}$$

$$w_1 \approx a + \frac{d_{\mathrm{SC}}}{2} - \frac{d_{\mathrm{SC}}}{2} \ln \frac{d_{\mathrm{SC}}}{a} + \frac{3}{2} d_{\mathrm{SC}} \ln 2 - \frac{d_{\mathrm{SC}}}{2} \ln \frac{a+b}{b-a}, \tag{2.50}$$

$$w_2 \approx b - \frac{d_{\mathrm{SC}}}{2} + \frac{d_{\mathrm{SC}}}{2} \ln \frac{d_{\mathrm{SC}}}{b} - \frac{3}{2} d_{\mathrm{SC}} \ln 2 + \frac{d_{\mathrm{SC}}}{2} \ln \frac{a+b}{b-a}, \tag{2.51}$$

and $K(k)$ is the complete elliptical integral of the first kind [39]. The sub-index l, g denote the central strip and ground surfaces, respectively.

The calculations of g_1 and g_2 for MS and CPW were performed in [38] by *conformal mapping techniques*.

2.3.3 Superconductors instead of conductors

Firstly, using superconductors instead of conductors implies that the calculation of the series impedance Z and shunt admittance Y are modified, because in superconductors $g_2 \neq 0$. Additionally, the conductivity is calculated with a different set of equations, modifying the surface impedance Z_s. These differences can be seen directly on equations 2.29, 2.30, and 2.31. Hence, the TL parameters are modified, since[1]

$$Z = R + \mathrm{j}\omega L_0, \tag{2.52}$$

$$Y = G + \mathrm{j}\omega C, \tag{2.53}$$

where L_0 is the inductance per unit length of the TL at null electric current, which introduces the second difference: current-dependence of the inductance per unit length L in

[1] In TLs with normal conductors, $L = L_0$, which justifies equation 2.27.

superconductors [5, 20], given by

$$L = L_0 \left(1 + \frac{I^2}{I_*^2}\right), \tag{2.54}$$

valid at temperatures $T \ll T_c$. Here, I_* determines the strength of the non-linear effect.

The origin of the current-dependence of the total inductance $L(I)$ is the inertia of the current carriers (Cooper pairs) in type I superconductors, which adds a so called **kinetic inductance** to the geometric one. From here, the "kinetic inductance" part of the name "KI-TWPA" is justified.

The term I_* is proportional to $I'_*/\sqrt{\alpha_*}$, where I'_* is a parameter comparable to the critical current I_c, and α_* is the ratio of kinetic inductance to total inductance [20].

The most important consequence of equation 2.54 is that the telegraph equations no longer have equations 2.9 and 2.10 as an equivalent set of equations. Instead, the equation for the electric current I is now a **non-linear wave equation**,

$$\left(\frac{\partial^2}{\partial z^2} - CL_0\frac{\partial^2}{\partial t^2} - (CR + GL_0)\frac{\partial}{\partial t} - RG\right) I = \frac{L_0}{3I_*^2}\left(G\frac{\partial}{\partial t} + C\frac{\partial^2}{\partial t^2}\right) I^3, \tag{2.55}$$

obtained from equations 2.7, 2.8, and 2.54.

It is useful to rewrite equation 2.55 as

$$\mathcal{L}I = \mathcal{N}I^3, \tag{2.56}$$

where $\mathcal{L}$ and $\mathcal{N}$ are, respectively, the differential operators acting on the linear and non-linear parts of the equation. The equation $\mathcal{L}I = 0$ corresponds to equation 2.9, the well known linear wave equation with general solution (for waves traveling in $+\mathbf{z}$)

$$I_{\text{linear}} = \frac{1}{2}\sum_n \left(A_n \mathrm{e}^{\mathrm{j}\omega_n t - \gamma_n z} + \text{c.c.}\right), \tag{2.57}$$

where "c.c." stands for "complex conjugate" and γ_n are the propagation constants that must fulfill the dispersion relation

$$\gamma_n^2 + CL_0\omega_n^2 - \mathrm{j}\omega_n(CR + GL_0) - RG = 0. \tag{2.58}$$

The solution can be obtained independently at each frequency in the linear wave equation, but if $\alpha_* \neq 0$ (i.e. $\mathcal{N} \neq 0$), the term I^3 allows for interaction between frequencies from where energy transfer can be achieved producing amplification of a target frequency. How much the target frequency is amplified depends on a specific parameter, the *pump signal*, which is the signal used as source of energy in the process. This whole process corresponds to *parametric amplification*, since a parametric equation for the current of the target signal I_s is obtained after replacing $I = I_s + I_i + I_p$, where I_i and I_p are the currents of the idler and pump signals, relevant in FWM [5]. Indeed, since

$$(I_s + (I_i + I_p))^3 = I_s^3 + 3I_s^2(I_i + I_p) + 3I_s(I_i + I_p)^2 + (I_i + I_p)^3, \tag{2.59}$$

equation 2.56 can be recast as

$$\mathcal{L}I_s - \mathcal{N}\left(I_s^3 + 3I_s^2(I_i + I_p) + 3I_s(I_i + I_p)^2\right) = -\mathcal{L}\left(I_i + I_p\right) + \mathcal{N}I_p^3, \tag{2.60}$$

where, if seen as an equation for the dependent variable $I_s(z,t)$, it is clear in the left-hand-side that some coefficients are oscillating in time and space, because they are proportional to combinations of I_i and I_p, which are waves themselves. Hence, at least a part of the equation for I_s is a parametric equation. Of course, the solution is more complex because of the right-hand-side of the equation acting as a forcing term for I_s, and because of the coupling between the different signals (the values of $I_s(z,t)$, $I_i(z,t)$ and $I_p(z,t)$ depend on each other). Nonetheless, this analysis helps to identify the non-linearity $\mathcal{N}I^3$ as the source of a parametric equation for $I_s(z,t)$, and hence, the possibility of achieving parametric amplification of $I_s(z,t)$.

This thesis approaches the problem of obtaining the gain in the target signal for the general dispersion relation where R and G can not be neglected, a case that has not been fully explored in the current literature[2].

2.3.4 Dispersion engineered transmission lines

In order to build a TL with a highly non-linear dispersion relation and with stopbands that avoid propagation of undesired signals at specific frequencies, a **Floquet TL**[3] is designed. This TL consists of a unit cell, with transfer matrix $\mathbb{M}$, infinitely repeated along the propagation direction. The unit cell is conformed by $m \in \mathbb{N}$ elements, each with a different transfer matrix $\mathbb{M}_k^{\text{cell}}$, $k \in \{1, 2, \ldots, m\}$. This configuration, depicted in Figure 2.5, is also called **dispersion engineered TL**.

Following the structure depicted in Figure 2.5.a, the unit cell transfer matrix is given by

$$\mathbb{M} \equiv \prod_{k=1}^{m} \mathbb{M}_k^{\text{cell}}. \tag{2.61}$$

Hence, as shown in Figure 2.5.b, subsequent values of voltage and current are related by the matrix equation

$$\begin{pmatrix} v_n \\ i_n \end{pmatrix} = \mathbb{M} \begin{pmatrix} v_{n+1} \\ i_{n+1} \end{pmatrix}, \tag{2.62}$$

where v_n, i_n are the voltage and current at the n-th step, respectively, i.e. just after n unit cells. From equation 2.62, the voltages and currents can be solved by noticing that the Floquet *ansatz* must hold in order to keep the periodic structure's translation symmetry [3], i.e.

$$\begin{pmatrix} v_{n+1} \\ i_{n+1} \end{pmatrix} = \mathrm{e}^{-\gamma d} \begin{pmatrix} v_n \\ i_n \end{pmatrix}, \tag{2.63}$$

[2] In [15], some study was done, but it is not complete. Some approximations are not justified nor valid at the operation frequencies of interest in KI-TWPAs made out of dispersion engineered TLs.

[3] Some literature refer to this as **Bloch TL** instead of *Floquet TL*, but mathematically *Floquet* is a more accurate name since a complex propagation constant is used instead of a purely imaginary one.

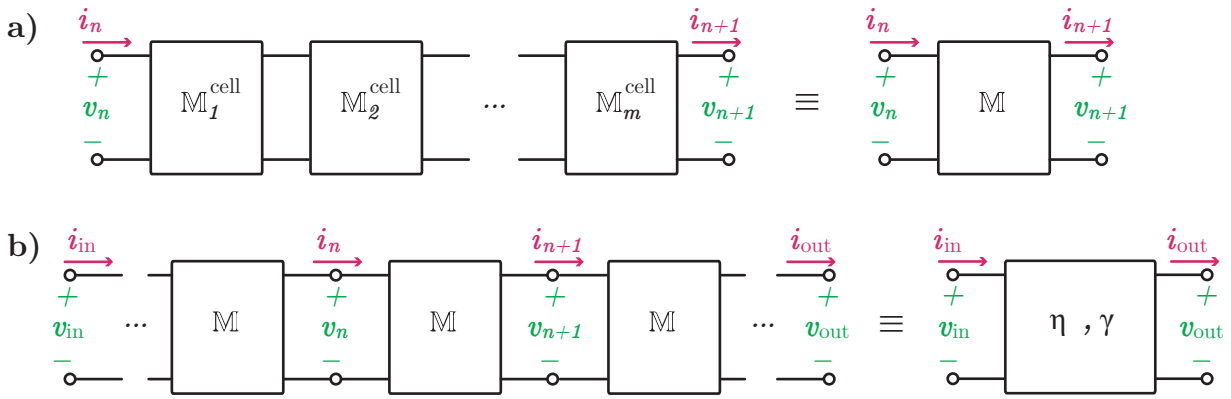

Figure 2.5: Representation of a periodic structure in its transfer matrices. (a) A sequence of m elements represented by the transfer matrices $\mathbb{M}_i^{\text{cell}}$ conform the unit cell of the periodic structure, with an equivalent transfer matrix $\mathbb{M}$. (b) The unit cell is infinitely repeated to form an equivalent transmission line [3], called Floquet transmission line, with (Floquet) characteristic impedance η and (Floquet) propagation constant γ.

where d is the length of the TL unit cell, and $\gamma = \alpha + \mathrm{j}\beta$ is the equivalent propagation constant through the Floquet TL, also called **Floquet propagation constant**. Here, α accounts for the losses due to successive reflections that appear throughout the inner structure of the unit cell, as well as the losses due to dissipation. Instead, β accounts for the spatial phase shift over the signal. Therefore, combining equations 2.62 and 2.63, the problem translates into an eigenvector-eigenvalue problem,

$$\mathbb{M} \begin{pmatrix} v_{\text{eig}} \\ i_{\text{eig}} \end{pmatrix} = \mathrm{e}^{\gamma d} \begin{pmatrix} v_{\text{eig}} \\ i_{\text{eig}} \end{pmatrix}, \tag{2.64}$$

which naturally defines an equivalent characteristic impedance η, called **Floquet characteristic impedance**, by

$$\eta \equiv \frac{v_{\text{eig}}}{i_{\text{eig}}}. \tag{2.65}$$

When solving the eigenvector-eigenvalue problem (equation 2.64), two solutions are obtained for γ, namely $\pm\gamma$ representing waves propagating towards $\pm z$, respectively, and η is given by [3, 4]

$$\eta_{\pm} = -\frac{M_{12}}{M_{11} - \mathrm{e}^{\pm\gamma d}}, \tag{2.66}$$

where M_{kl} is the matrix element of $\mathbb{M}$ at row k and column l. Nonetheless, when solving for γ, different combinations of $\pm\alpha, \pm\beta$ are allowed mathematically. Hence, to respect the stated definition[4]in which $+\gamma$ represents waves propagating towards $+z$, the solution with positive group speed $v_g \equiv 2\pi \left(\frac{\partial\beta}{\partial\nu}\right)^{-1}$ must be chosen [4]. In this case, $\mathrm{Re}\{\eta_+\} \geq 0$, and hence the power is confirmed to travel towards $+z$ [4].

[4]This is the convention used along this thesis. This and other conventions are thoroughly discussed in [4].

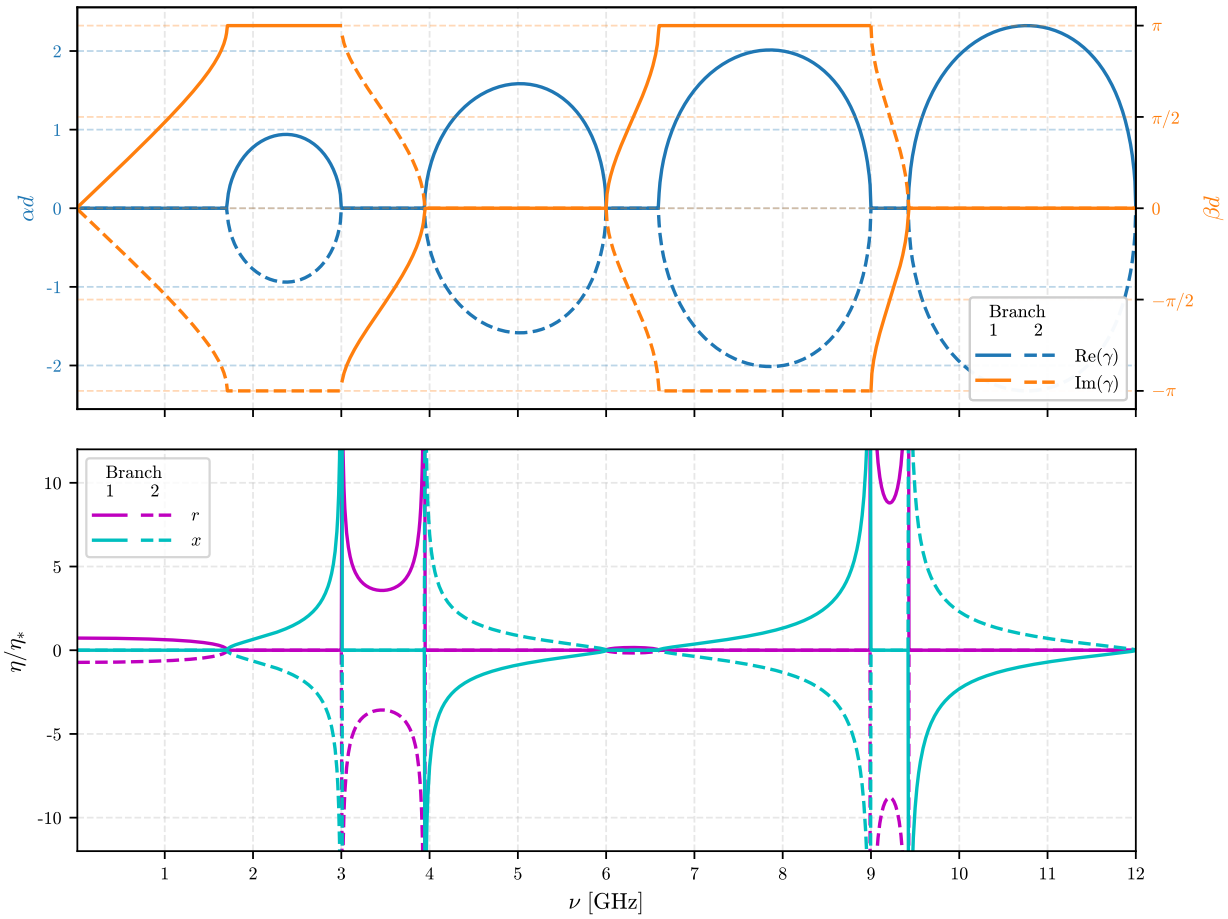

Figure 2.6: Dispersion relation within the reduced Brillouin zone (top) and corresponding effective characteristic impedance (bottom) obtained by a periodic structure with a unit cell constituted by a lossless transmission line of length $d = 5$ cm and a capacitor in the middle with capacitance $C_1 = 3$ pF. The transmission line used has a characteristic impedance $\eta_0 = 50\ \Omega$ and a propagation constant $\gamma_0 = \mathrm{j}2\pi\nu/c_0$, where c_0 is the speed of light in vacuum. The characteristic impedance η is shown in units of a reference value $\eta_* \equiv 50\ \Omega$. The continuous (segmented) lines correspond to the branch of solutions representing a wave propagating towards $+z$ ($-z$) according to the convention of positive group speed $v_g \equiv 2\pi \left(\frac{\partial\beta}{\partial\nu}\right)^{-1}$ analyzed in [4]. The correct separation of branches can be verified by noticing that $\alpha \geq 0$ and $r \geq 0$ for Branch 1, while $\alpha \leq 0$ and $r \leq 0$ for Branch 2. This periodic structure shows stopbands, identified by the frequency intervals where $\beta d = n\pi, n \in \mathbb{Z}$, and in this case (since a lossless transmission line was used) corresponding to the only intervals where $\alpha \neq 0$.

As an example of a Floquet TL, a periodic structure with a unit cell constituted by a lossless transmission line of length $d = 5$ cm and a capacitor in the middle with capacitance $C_1 = 3$ pF is considered. The two solution branches for γ and η are shown in Figure 2.6. The dispersion relation shown here is the folded one, i.e. within the reduced Brillouin zone. As long as β appears only as a phase factor $\mathrm{e}^{\mathrm{j}\beta z}$, it is not relevant to unfold the solution. However, if derivatives with respect to z appear, dropping β out of the phase factor, the unfolded solution is required to obtain correct calculations. Figure 2.7 shows how this is done in the example

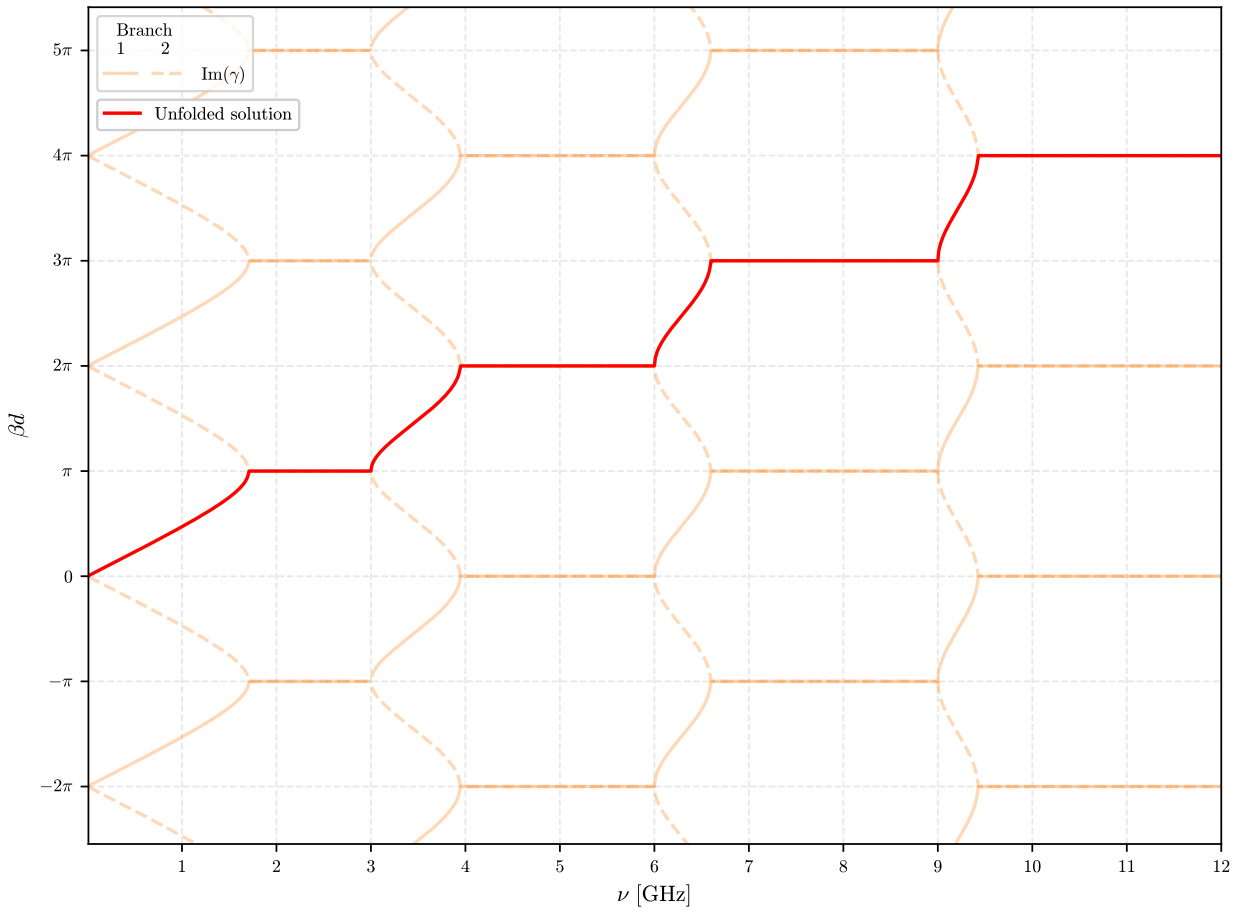

Figure 2.7: Unfolded dispersion relation for Fig. 2.6. Possible solutions for all Brillouin zones are displayed as semi-transparent orange curves with the same nomenclature described in Fig. 2.6, and the correct continuous solution to use for further calculations for Branch 1 is the unfolded β shown in red. The unfolded solution for Branch 2 is just the negative of the red curve shown. If βd is only used as a phase factor, any of the possible solutions for Branch 1 (2) can be used to correctly described a wave propagating towards $+z$ ($-z$) since a difference $\pm 2\pi$ is irrelevant in any phase, but if derivatives of this phase factor are to be calculated, the unfolded solution must be used. To verify that the unfolding shown is the correct solution, it suffices to notice that in the limit of neglecting the capacitance C_1 by either making $C_1 \to 0$ or $d \to \infty$ the dispersion relation of the homogeneous transmission line is recovered as the effective one.

of Figure 2.6.

All of what has been explained in this section allows to obtain effective values of η and γ to represent the whole TL without having to care about the inner periodic structure. Thereafter, the TL parameters can be obtained by applying the inverse relation from equations 2.13 and 2.15, while considering equations 2.52 and 2.53, i.e. by

$$Z = \gamma\eta, \tag{2.67}$$

$$Y = \frac{\gamma}{\eta}, \tag{2.68}$$

and hence, the problem of parametric amplification reduces back to solving equation 2.55, but now with a non-linear dispersion relation and stopbands to be designed to enhance the process. The frequencies that are necessary to suppress are explained in the next section.

2.4 Four-wave-mixing

FWM consists in a process described by a non-linear wave equation where the non-linear term is cubic in the variable I behaving as wave. In this case, the term with I^3 obtains units of energy after multiplying by I. Hence, in terms of energy, the process consists in general of four mutually interacting waves. At the quantum level, this means that the energy transfer occurs fundamentally by exchange of pairs of photons, rather than single ones [28]. However, this does not restrict the amount of different waves (at different frequencies) that can interact. The non-linear electric current wave equation 2.55 is an example of a FWM process.

When a target signal and a pump signal, with respective angular frequencies ω_s and ω_p, are injected in a FWM system, many other frequencies are generated through the process. The main signals resultant of this, are depicted in Figure 2.8, where the fact that the target signal of interest has a much smaller amplitude than the pump has been applied to neglect some frequencies [5]. The most relevant of the generated signals is the idler one, with angular frequency ω_i, which is needed to obtain amplification of the target signal [28]. Due to the non-linear term $\propto I^3$, only odd harmonics are generated. The 3$^{\text{rd}}$ pump's harmonic ($3p$ signal) is undesired, because a lot of energy is being transferred from the pump into this signal, instead of the target signal. The other pump's harmonics are also undesired, but they are not as relevant as the 3$^{\text{rd}}$ one, as can be seen in Figure 2.8. Therefore, the TL should ideally suppress the $3p$ signal making it fall into a stopband. This is one of the objectives when designing a Floquet TL for KI-TWPAs.

In literature, the FWM is very well known in optical systems. But in MW systems, it is still in study. As a solution to equation 2.55, a set of amplitude equations has been used[5] [20]

$$\frac{\partial A_s}{\partial z} = \frac{\mathrm{j}\beta_s}{8I_*^2}\left[A_s(|A_s|^2 + 2|A_i|^2 + 2|A_p|^2) + A_i^* A_p^2 \mathrm{e}^{-\mathrm{j}\Delta\beta}\right], \tag{2.69}$$

$$\frac{\partial A_i}{\partial z} = \frac{\mathrm{j}\beta_i}{8I_*^2}\left[A_i(2|A_s|^2 + |A_i|^2 + 2|A_p|^2) + A_s^* A_p^2 \mathrm{e}^{-\mathrm{j}\Delta\beta}\right], \tag{2.70}$$

$$\frac{\partial A_p}{\partial z} = \frac{\mathrm{j}\beta_p}{8I_*^2}\left[A_p(2|A_s|^2 + 2|A_i|^2 + |A_p|^2) + 2A_p^* A_s A_i \mathrm{e}^{\mathrm{j}\Delta\beta}\right], \tag{2.71}$$

where

$$\Delta\beta = \beta_s + \beta_i - 2\beta_p, \tag{2.72}$$

the complex amplitudes are denoted by A, and the subindices s, p, and i correspond to *(target) signal*, *pump*, and *idler*, respectively.

These amplitude equations, though, neglect α and x, which also implies setting $R = G = 0$ in the non-linear wave equation. This is justified away from the stopbands, but not close

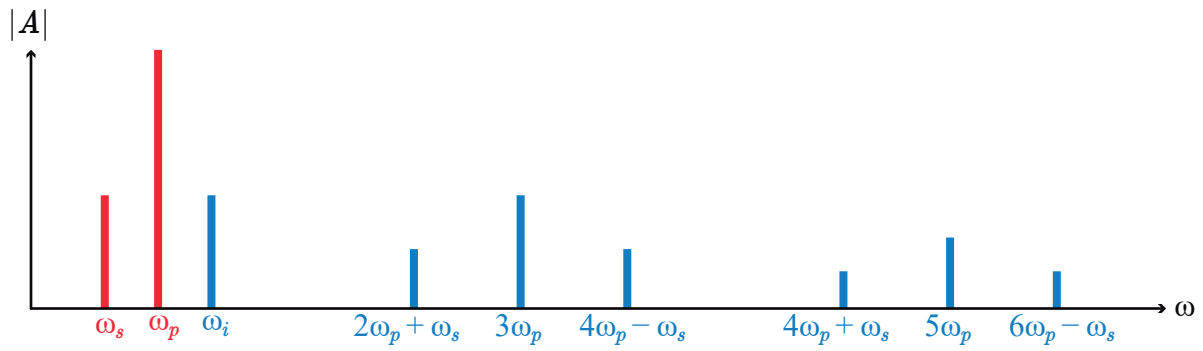

Figure 2.8: Fourier spectrum of the main signals relevant in the FWM process as shown in [5]. In red are the represented the physically injected signals, while in blue are signals generated in the FWM process. From the generated ones, the idler signal with angular frequency ω_i and the third pump's harmonic with angular frequency $3\omega_p$ are the most relevant, depicted by larger amplitudes $|A|$. Many more signals appear at higher frequencies, but these are less relevant because of their much smaller amplitudes.

to them. This fact is extremely important since these are the operation zones needed to achieve high amplification, because of the high non-linear dispersion relation around them. The development of more accurate models that do not neglect α and x, is the central work of this thesis. The only work that has approached this task so far is [15], but the study is incomplete and leaves some approximations unjustified. Furthermore, the procedure followed in [15] is much less mathematically rigorous than the one used along this thesis. The latter is described in the next section.

2.5 Multiple scales method

The mathematical formalism used in this thesis to derive the sets of amplitude equations for the current signals in FWM is the **multiple scales method**. It is a perturbative method applicable to solve non-linear equations. The method is described in general terms in this section, and later applied in chapter 3 to solve equation 2.55.

The multiple scales method consists in following the next steps [29, 40]:

1. Determine the scales of each term of the equation in order to solve differentiating in orders of magnitude[6] (scales) as explained in the next step.

2. Separate the dynamical independent variables (like time and position) in the corresponding different scales, treating each of them as independent variables. For example,

$$\frac{\partial}{\partial z} \mapsto \frac{\partial}{\partial z} + \epsilon \frac{\partial}{\partial z_1} + \epsilon^2 \frac{\partial}{\partial z_2} + ..., \tag{2.73}$$

[5]The factor 8 in the denominator of these equations is replaced by a 2 in [20]. Nonetheless, this has been identified as a typo in that reference. This can be checked by either performing the calculations (as done for this thesis) or comparing with similar results from non-linear optics [28].

[6]In FWM this is relevant because the the amplitude changes are appreciable in a larger scale than that of the wavelengths.

where

$$z_n = \epsilon^n z, \tag{2.74}$$

are all treated as independent variables.

3. Expand the dependent variable $y(z)$ in different orders such that the zeroth order involves only linear terms (not necessarily all of them), which defines a linear equation with differential operator $\mathcal{L}$.

4. Identify the order at which the non-linear term affects the dynamics and balance the equation at the desired order of solution. This will give the correct perturbative form to the equation.

5. To solve at first order, an equation $\mathcal{L}y^{(1)} = \mathcal{N}(y^{(0)})^x$ must be solved, where $y^{(0)}$ and $y^{(1)}$ are the solutions at zeroth and first order, respectively, and $x \in \mathbb{R}$ is a power at which $y^{(0)}$ might be raised to, depending on the type of non-linear equation. In order to guarantee the solubility of the problem for $y^{(1)}$, the operator $\mathcal{L}$ must be invertible and then $y^{(1)} = \mathcal{L}^\dagger \mathcal{N} y^{(0)}$ is the solution. However, the solution must respect the multiple scales and can not diverge, which means that secular terms must be avoided. To achieve this goal, the slow scales of the solution $y(z, z_1, \ldots, z_n)$ (scale at which the non-linear term acts) must fulfill conditions such that the projection of $\mathcal{N}y^{(0)}$ on the eigenbasis of $\mathcal{L}^\dagger$ results null. In oscillatory systems, the slow part of $y(z, z_1, \ldots, z_n)$ is usually its oscillation amplitude $A(z_1, \ldots, z_n)$, and the described conditions receive the name of **amplitude equations**.

6. Solve the amplitude equations, specific to the problem. This is much simpler to do than directly solving the initial non-linear equation. It can usually be done numerically, and in some cases, analytically.

7. After solving for the solution at first order, $y^{(1)}$, a similar process can be followed to continue solving at higher orders. Nonetheless, for the current thesis, the first order is enough.

These steps, from 1 to 6, will be followed with detail to solve the non-linear wave equation 2.55, where the dependent variable is the electric current $I(z)$ traveling along the KI-TWPA.

2.6 Summary

In this chapter, the fundamental concepts needed to understand the problem to solve in KI-TWPAs have been explained. From these concepts, the non-linear wave equation for the electric current $I(z)$ along the device has been derived, while being identified as a parametric equation and a FWM process, meaning that an amplification of the target signal should be possible. Additionally, the procedure and equations needed to calculate the TL parameters of a superconducting Floquet TL (consisting in periodic elements) have been given. In this Floquet TL, a highly non-linear dispersion relation can be obtained, while generating stopbands at frequencies where undesired signals would otherwise be generated in the FWM process. Hence, the task of optimizing the amplification of the target signal has been reduced

to a design problem. Finally, to obtain the gain of the target signal, the non-linear wave equation for $I(z)$ has to be solved. In order to achieve this, the method of multiple scales has been presented, which allows to reduce the problem into sets of amplitude equations to be derived in detail in chapter 3.

Chapter 3

Solution to the non-linear wave equation in four-wave-mixing

In this chapter, the non-linear wave equation 2.55 will be solved by using the multiple scales method explained in chapter 2. Different models will be derived depending on the dominant orders of magnitude of each of the equation terms. In the limiting case of $\alpha = 0$ and $x = 0$, the *Old model* used in the literature should be recovered. This model, in the case where the signals are only the target signal (s), the idler (i), and the pump (p), is defined by the amplitude equations 2.69, 2.70, and 2.71. In particular, the models derived in this chapter will focus on orders of magnitude that are often achieved with Floquet TLs near the stopbands, which are the operation points for the pump signal. This will be clear in chapter 4, where the models are applied in a real design of a KI-TWPA.

Throughout this and subsequent chapters, the frequency range over which a model is valid is called "zone", unless explicitly stated otherwise. These zones should not be confused with the Brillouin zones from subsection 2.3.4.

3.1 Models and zones

Firstly, recall that the non-linear wave equation for the electric current I, is given by equation 2.55:

$$\left(\frac{\partial^2}{\partial z^2} - CL_0\frac{\partial^2}{\partial t^2} - (CR + GL_0)\frac{\partial}{\partial t} - RG\right) I = \frac{L_0}{3I_*^2}\left(G\frac{\partial}{\partial t} + C\frac{\partial^2}{\partial t^2}\right) I^3,$$

or more compactly,

$$\mathcal{L}I = \mathcal{N}I^3.$$

The order of magnitude of each term in the non-linear current equation depends on the frequency of the current wave. The total current I contains many frequency components, but the dominant one is that of the pump. Hence, depending on the pump frequency, different terms of the equation are to be considered at first order in the perturbative analysis. The

orders (scales) are separated by a positive factor $\epsilon \ll 1$ that comes from the fact that $\tilde{I} \equiv \frac{I}{I_*} < 1$ and $\tilde{I} = \tilde{I}^{(0)} + \epsilon\tilde{I}^{(1)} + \epsilon^2\tilde{I}^{(2)} + \ldots$, i.e. the total dimensionless current is expanded in orders of ϵ. Therefore, three main regimes are identified for the problem in study, each dominating in a different **zone** of frequencies. Each regime is defined by a unique model:

1. Model "**New1**" (over zone 1):

$$\left(\frac{\partial^2}{\partial z^2} - CL_0\frac{\partial^2}{\partial t^2}\right)\tilde{I} = \epsilon\left(\frac{L_0C}{3}\frac{\partial^2}{\partial t^2}\right)\tilde{I}^3. \tag{3.1}$$

2. Model "**New2**" (over zone 2):

$$\left(\frac{\partial^2}{\partial z^2} - CL_0\frac{\partial^2}{\partial t^2}\right)\tilde{I} = \epsilon(CR + GL_0)\frac{\partial}{\partial t}\tilde{I} + \epsilon\left(\frac{L_0C}{3}\frac{\partial^2}{\partial t^2}\right)\tilde{I}^3. \tag{3.2}$$

3. Model "**New3**" (over zone 3):

$$\left(\frac{\partial^2}{\partial z^2} - CL_0\frac{\partial^2}{\partial t^2}\right)\tilde{I} = \epsilon RG\tilde{I} + \epsilon(CR + GL_0)\frac{\partial}{\partial t}\tilde{I} + \epsilon\left(\frac{L_0C}{3}\frac{\partial^2}{\partial t^2}\right)\tilde{I}^3. \tag{3.3}$$

In general, the zone 1 corresponds to frequencies far from the stopbands, while zones 2 and 3 appear as one gets closer and closer to the stopbands. More zones could be defined, as it will appear clear in the next chapter, but such analysis exceeds the reach of the present thesis. See annexed A for a more detailed derivation of the models and zones.

The "**Old**" model used in the literature corresponds to any of the "**New**" models but changing the value of the TL parameters (R, G, C, L_0) for ones that neglect $x \equiv \mathrm{Im}\{\eta\}$ and $\alpha \equiv \mathrm{Re}\{\gamma\}$. This can be seen by noticing that all three models converge to the same in the limiting case of $x = \alpha = 0$, because then $RG = CR + GL_0 = 0$.

The models identified in this section correspond to the first step in the multiple scales method.

3.2 Solution to each model

After applying steps 2 to 5 of the multiple scales method (see annexed A), for each of the New models, the general form of the amplitude equations (at first order in ϵ) are obtained for each of the N signals involved in the FWM process.

1. **Model New1**: from equation 3.1, the amplitude equation for the $m-$th signal is

$$\frac{\partial A_m}{\partial z} = \frac{f_m e^{j\beta_m z}}{3\cdot 8\cdot I_*^2}\left\langle e^{j\omega_m t}\left|\left(\sum_n^N A_n e^{j(\omega_n t-\beta_n z)} + \text{c.c.}\right)^3\right.\right\rangle. \tag{3.4}$$

2. **Model New2**: from equation 3.2, the amplitude equation for the $m-$th signal is

$$\frac{\partial A_m}{\partial z} = -2\alpha_m A_m + \frac{f_m e^{j\beta_m z}}{3\cdot 8\cdot I_*^2}\left\langle e^{j\omega_m t}\left|\left(\sum_n^N A_n e^{j(\omega_n t-\beta_n z)} + \text{c.c.}\right)^3\right.\right\rangle. \tag{3.5}$$

3. **Model New3**: from equation 3.3, the amplitude equation for the $m-$th signal is

$$\frac{\partial A_m}{\partial z} = \mathrm{j} g_m A_m - 2\alpha_m A_m + \frac{\mathrm{j} f_m \mathrm{e}^{\mathrm{j}\beta_m z}}{3 \cdot 8 \cdot I_*^2} \left\langle \mathrm{e}^{\mathrm{j}\omega_m t} \left| \left(\sum_n^N A_n \mathrm{e}^{\mathrm{j}(\omega_n t - \beta_n) z} + \mathrm{c.c.} \right)^3 \right\rangle \right. . \tag{3.6}$$

In all the previous equations,

$$f_m = \frac{1}{2\beta_m} \left(\alpha_m^2 - \beta_m^2 - \frac{|\gamma_m|^2}{|\eta_m|^2} (r_m^2 - x_m^2) \right), \tag{3.7}$$

$$g_m = \frac{\alpha_m^2 r_m^2 - \beta_m^2 x_m^2}{\beta_m (r_m^2 + x_m^2)}. \tag{3.8}$$

The Old model is recovered on each new model by imposing $\alpha_m = 0$ and $x_m = 0$. This makes $g_m = 0$ and $f_m = -\beta_m$. Nonetheless, this imposition is wrong, even as an approximation, for zones 2 and 3.

Next sections will specify the number of waves N considered in the initial ansatz, obtaining different sets of equations.

3.3 Pump alone (p case)

When there is only one signal, e.g. the pump, there is only one amplitude equation, given by

$$\frac{\partial A_p}{\partial z} = \mathrm{j} g_p A_p \xi_3 - 2\alpha_p A_p \xi_2 + \mathrm{j} \frac{f_p}{8 I_*^2} A_p |A_p|^2, \tag{3.9}$$

where

$$\xi_2 = \begin{cases} 1 & \text{for New2 or New3} \\ 0 & \text{for New1} \end{cases}, \tag{3.10}$$

$$\xi_3 = \begin{cases} 1 & \text{for New3} \\ 0 & \text{for New1 or New2} \end{cases}, \tag{3.11}$$

are binary parameters to select the model.

By writing $A_p \equiv |A_p| \mathrm{e}^{\mathrm{j}\phi_p}$, equation 3.9 can be separated in its real and imaginary parts, obtaining

$$\frac{\partial |A_p|}{\partial z} = -2\alpha_p |A_p| \xi_2, \tag{3.12}$$

$$\frac{\partial \phi_p}{\partial z} = g_p \xi_3 + \frac{f_p}{8 I_*^2} |A_p|^2, \tag{3.13}$$

from which it is clear that no amplification can be obtained, since the solution to equation 3.12 is $|A_p(z)| = \xi_2 \left| A_p^0 \right| \mathrm{e}^{-2\alpha_p z}$. Indeed, no external energy source is included, and hence, there is no way for the p signal to gain energy and be amplified.

Recalling step 5 of the multiple scales method, the first order solution of the electric current is given by $\mathcal{L}I^{(1)} = \mathcal{N}(I^{(0)})^3$ with only the pump signal, $I^{(0)} = \frac{1}{2}(A_p e^{j(\omega_p t - \beta_p z)} + \text{c.c.})$, in this case. Hence, by applying the time-Fourier transform, the solutions for $I^{(1)}$ correspond to signals at frequencies that result from the combinations allowed from $(I^{(0)})^3$. In this case, this means only the angular frequency $3\omega_p$. Hence, the generation of the third harmonic is deduced from this analysis. This harmonic could be now included in the initial ansatz of $I^{(0)}$ to obtain a more precise answer at first order from the amplitude equations.

3.4 Target signal and pump ($s - p$ case)

When there are two signals, e.g. the pump and the target signal, the amplitude equations are

$$\frac{\partial A_s}{\partial z} = j g_s A_s \xi_3 - 2\alpha_s A_s \xi_2 + j\frac{f_s}{8I_*^2} A_s(|A_s|^2 + 2|A_p|^2), \tag{3.14}$$

$$\frac{\partial A_p}{\partial z} = j g_p A_p \xi_3 - 2\alpha_p A_p \xi_2 + j\frac{f_p}{8I_*^2} A_p(2|A_s|^2 + |A_p|^2). \tag{3.15}$$

By writing $A_m \equiv |A_m| e^{j\phi_m}$, these equations can be separated in their real and imaginary parts. In particular, the real parts give

$$\frac{\partial |A_s|}{\partial z} = -2\alpha_s |A_s| \xi_2, \tag{3.16}$$

$$\frac{\partial |A_p|}{\partial z} = -2\alpha_p |A_p| \xi_2, \tag{3.17}$$

which are identical equations to equation 3.12. Hence, the same type of solution is obtained, showing that no gain is obtained in any direction (not towards the pump nor the target signal). This is because another signal, the generated idler signal, is necessary in order to exchange energy quanta between the signals, as explained in chapter 2.

In this case, the zeroth order ansatz is

$$I^{(0)} = \frac{1}{2}(A_s e^{j(\omega_s t - \beta_s z)} + A_p e^{j(\omega_p t - \beta_p z)} + \text{c.c.}). \tag{3.18}$$

Therefore, the angular frequency combinations obtained from $(I^{(0)})^3$ are $3\omega_s, 3\omega_p, \pm 2\omega_p \pm \omega_s, \pm 2\omega_p \mp \omega_s, \pm\omega_p \pm 2\omega_s$, and $\pm\omega_p \mp 2\omega_s$, where the idler angular frequency $\omega_i \equiv 2\omega_p - \omega_s$ is included. Hence, each of this signals could be inserted in the initial ansatz to obtain a better solution at first order. Nonetheless, for the case of interest, in which the target signal is much smaller in amplitude than the pump signal, many of these frequency components can be neglected. Indeed, from the Fourier spectrum of a FWM process, shown in Figure 2.8 in chapter 2, it is known that the dominant components are, first the idler, and second the pump's third harmonic. Therefore, these are the only two to be considered in further analysis.

It is very interesting to notice how all these signals, generated through the FWM process, can be derived with this mathematical approach. Furthermore, it is easy to realize that if

the $3p$ signal is included in the initial ansatz, a combination $3\omega_p + \omega_p + \omega_p \equiv 5\omega_p$ is obtained from $(I^{(0)})^3$. Then, it is possible to derive all the frequencies shown in the Fourier spectrum of Figure 2.8, as well as the ones neglected in that plot.

3.5 Inclusion of the idler signal ($s - p - i$ case)

In the $s - p$ case, if the generated idler is included in the initial ansatz, the amplitude equations change to

$$\frac{\partial A_s}{\partial z} = \mathrm{j}g_s A_s \xi_3 - 2\alpha_s A_s \xi_2 + \mathrm{j}\frac{f_s}{8I_*^2}\left[A_s(|A_s|^2 + 2|A_i|^2 + 2|A_p|^2) + A_i^* A_p^2 \mathrm{e}^{\mathrm{j}\Delta\beta z}\right], \tag{3.19}$$

$$\frac{\partial A_i}{\partial z} = \mathrm{j}g_i A_i \xi_3 - 2\alpha_i A_i \xi_2 + \mathrm{j}\frac{f_i}{8I_*^2}\left[A_i(2|A_s|^2 + |A_i|^2 + 2|A_p|^2) + A_s^* A_p^2 \mathrm{e}^{\mathrm{j}\Delta\beta z}\right], \tag{3.20}$$

$$\frac{\partial A_p}{\partial z} = \mathrm{j}g_p A_p \xi_3 - 2\alpha_p A_p \xi_2 + \mathrm{j}\frac{f_p}{8I_*^2}\left[A_p(2|A_s|^2 + 2|A_i|^2 + |A_p|^2) + 2A_p^* A_s A_i \mathrm{e}^{-\mathrm{j}\Delta\beta z}\right], \tag{3.21}$$

where $\Delta\beta \equiv \beta_s + \beta_i - 2\beta_p$.

By writing $A_m \equiv |A_m|\mathrm{e}^{\mathrm{j}\phi_m}$, these equations can be separated in their real and imaginary parts. In particular, the real parts give

$$\frac{\partial |A_s|}{\partial z} = -2\alpha_s |A_s|\xi_2 - \frac{f_s}{8I_*^2}|A_i||A_p|^2 \sin\Theta(z), \tag{3.22}$$

$$\frac{\partial |A_i|}{\partial z} = -2\alpha_i |A_i|\xi_2 - \frac{f_i}{8I_*^2}|A_s||A_p|^2 \sin\Theta(z), \tag{3.23}$$

$$\frac{\partial |A_p|}{\partial z} = -2\alpha_p |A_p|\xi_2 + 2\frac{f_p}{8I_*^2}|A_s||A_i||A_p| \sin\Theta(z), \tag{3.24}$$

where $\Theta(z) \equiv \Delta\beta z - \Delta\phi(z)$, and $\Delta\phi(z) \equiv \phi_s + \phi_i - 2\phi_p$. The phase $\Theta(z)$ is the **total phase mismatch** that consists in a **linear phase mismatch** $\Delta\beta z$ and a **non-linear phase mismatch** $\Delta\phi(z)$. The phase mismatch is relevant, because depending on its value, transfer of energy occurs from the pump toward the target and idler signals ($\Theta \in (0, \pi)$), or viceversa ($\Theta \in (-\pi, 0)$), noticing that $f_m < 0$. Moreover, in the very special cases of $\Theta = 0, \pm\pi$, no transfer of energy happens between the signals. Therefore, thanks to the existence of the phase mismatch, these amplitude equations that included the idler signal, predict the possibility of amplifying the target signal. Furthermore, the ideal situation occurs when $\Theta = \frac{\pi}{2}$, maximizing the transfer rate of energy toward the target signal.

3.6 Inclusion of $3\omega_p$ ($s - p - i - 3p$ case)

The $s - p - i$ case can be improved by including the $3p$ signal in the initial ansatz. Hence, the amplitude equations become

$$\frac{\partial A_s}{\partial z} = \mathrm{j}g_s A_s \xi_3 - 2\alpha_s A_s \xi_2 + \frac{f_s}{8I_*^2}\left[A_s(|A_s|^2 + 2|A_i|^2 + 2|A_p|^2 + 2|A_{3p}|^2) + A_i^* A_p^2 \mathrm{e}^{\mathrm{j}\Delta\beta z} + 2A_i^* A_p^* A_{3p} \mathrm{e}^{\mathrm{j}\Delta\beta_2 z}\right], \tag{3.25}$$

$$\frac{\partial A_i}{\partial z} = \mathrm{j}g_i A_i \xi_3 - 2\alpha_i A_i \xi_2 + \frac{f_i}{8I_*^2}\left[A_i(2|A_s|^2 + |A_i|^2 + 2|A_p|^2 + 2|A_{3p}|^2) + A_s^* A_p^2 \mathrm{e}^{\mathrm{j}\Delta\beta z} + 2A_s^* A_p^* A_{3p} \mathrm{e}^{\mathrm{j}\Delta\beta_2 z}\right], \tag{3.26}$$

$$\frac{\partial A_p}{\partial z} = \mathrm{j}g_p A_p \xi_3 - 2\alpha_p A_p \xi_2 + \frac{f_p}{8I_*^2}\left[A_p(2|A_s|^2 + 2|A_i|^2 + |A_p|^2 + 2|A_{3p}|^2) + 2A_p^* A_s A_i \mathrm{e}^{-\mathrm{j}\Delta\beta z} + 2A_s^* A_i^* A_{3p} \mathrm{e}^{\mathrm{j}\Delta\beta_2 z} + A_{3p}(A_p^*)^2 \mathrm{e}^{\mathrm{j}\Delta\beta_3 z}\right], \tag{3.27}$$

$$\frac{\partial A_{3p}}{\partial z} = \mathrm{j}g_{3p} A_{3p} \xi_3 - 2\alpha_{3p} A_{3p} \xi_2 + \frac{f_{3p}}{8I_*^2}\left[A_{3p}(2|A_s|^2 + 2|A_i|^2 + 2|A_p|^2 + 2|A_{3p}|^2) + \frac{1}{3}A_p^3 \mathrm{e}^{-\mathrm{j}\Delta\beta_3 z} + 2A_s A_i A_p \mathrm{e}^{-\mathrm{j}\Delta\beta_2 z}\right], \tag{3.28}$$

where $\Delta\beta_2 \equiv \beta_s + \beta_i + \beta_p - \beta_{3p}$, and $\Delta\beta_3 \equiv 3\beta_p - \beta_{3p}$.

A deeper mathematical analysis of the involved phases in this process could be done, but it escapes the scope of this thesis. Instead, in the current thesis, these analysis are given from the results obtained by simulations, whose results will be presented in chapters 4, 5, and 6.

3.7 Important remarks

From the previous mathematical analysis, two important general remarks are to be kept in mind.

1. The relevant constant factor for amplification is f_m. Hence, the larger it can be, the better, in order to obtain gain of the target signal. This can be seen in the derived amplitude equations by noticing that the coupling terms are all proportional to f_m.

2. The term g_m affects only the phase mismatch, but not directly the equation for $|A_m|$. This is seen from the lack of g_m in the derived equations for $|A_m|$. Hence, if there is any relevant difference in the simulations between the New3 and New2 models, it is due to the effect of g_m on the phase mismatch Θ.

3.8 General considerations

The TLs studied in chapters 4, 5, and 6 consist of a central TL, with propagation constant $\gamma_0 \equiv \alpha_0 + \mathrm{j}\beta_0$ and characteristic impedance $\eta_0 \equiv r_0 + \mathrm{j}x_0$, that contains small sections of different strip width that are periodically repeated. Therefore, the complete TL is a Floquet TL with effective propagation constant $\gamma \equiv \alpha + \mathrm{j}\beta$ and effective characteristic impedance $\eta \equiv r + \mathrm{j}x$. This Floquet TL produces frequency stopbands, defined by $\delta\alpha \equiv \alpha - \alpha_0 \neq 0$, and a non-linear dispersion relation $\beta(\nu)$ near the stopbands, identified by $\delta\beta \equiv \beta - \beta_0 \neq 0$. The latter is very important, because it allows to tune the linear phase mismatch $\Delta\beta z \equiv \beta_s z + \beta_i z - 2\beta_p z$, relevant for the amplification of the target signal, as discussed in section 3.5.

3.9 Summary

In this chapter, the amplitude equations for different models applicable to different cases (different amount of signals considered) have been formally deduced applying the multiple scales method. From these derivations, it was also possible to deduce the generated signals, including the idler and the third pump's harmonic. Amplification was shown to occur only if the idler signal is considered in the FWM process. Moreover, a key quantity that determines whether amplification occurs or not was obtained, the *phase mismatch*. From here, all what is left is to simulate to analyze the results, which is the objective of chapters 4, 5, and 6.

Chapter 4

CPW simulations: zones and models

A CPW design based on what was experimentally tested by Eom [20] is used in this chapter. Nonetheless, lack of precision in the provided data made impossible to reproduce the exact same design. Hence, a similar one is designed for this chapter, expecting similar results. Additionally, a deep analysis of the different models and corresponding zones is done throughout this chapter.

4.1 Design

The design consists in a Floquet TL whose unit cell (shown in Figure 4.1.a) is conformed by a main central homogeneous TL of width w_0 and three small sections of TL of length D_1, D_1, and D_2 where the width is enlarged to $w_1 > w_0$. These small sections of width w_1 are called dispersive loads, since they produce the stopbands and the non-linear dispersion relation. The dispersive loads have a center-to-center separation of length $D_0 \gg D_1, D_2$. This is the reason to call the TL of width w_0 as the "*main*" line, and the sections of width w_1 as "*loads*". This type of Floquet unit cell is the type used in [20] and [5].

The design parameters that were used are given in Tables 4.1 and 4.2. The former shows the general values for the CPW geometry used, i.e. the strip-to-ground spacing s, the superconductor thickness t, the superconductor's critical temperature T_c, the operation temperature T, the superconductor's normal resistivity $\rho_N \equiv 1/\sigma_N$, the substrate's dielectric constant ϵ_r, and the substrate's loss-tangent $\tan\delta$. The design parameters consider the use of NbTiN as the superconducting material, and Si as the substrate material. Table 4.2, instead, shows the parameters that define the unit cell of the Floquet TL, including the total length $d \equiv 3D_0$. The **characteristics** of the central line, i.e. the propagation constant $\gamma_0 \equiv \alpha_0 + \mathrm{j}\beta_0$ and the characteristic impedance $\eta_0 \equiv r_0 + \mathrm{j}x_0$ as functions of the frequency, are shown in Figure 4.2.

In this design, $D_0 = \lambda_{\text{per}}/2$, where λ_{per} is the wavelength (calculated for the central line) with corresponding frequency ν_{per}. Hence, if $D_2 = D_1$, this produces stopbands around frequencies multiple of ν_{per}, i.e. around $n\nu_{\text{per}}, n \in \mathbb{N}$. This selection is done thinking in suppression of the third pump's harmonic with frequency $3\nu_p$. Therefore, the operating pump frequency would be $\nu_p \approx n\nu_{\text{per}}/3$ for a selected $n \in \mathbb{N}$. In order to produce a high

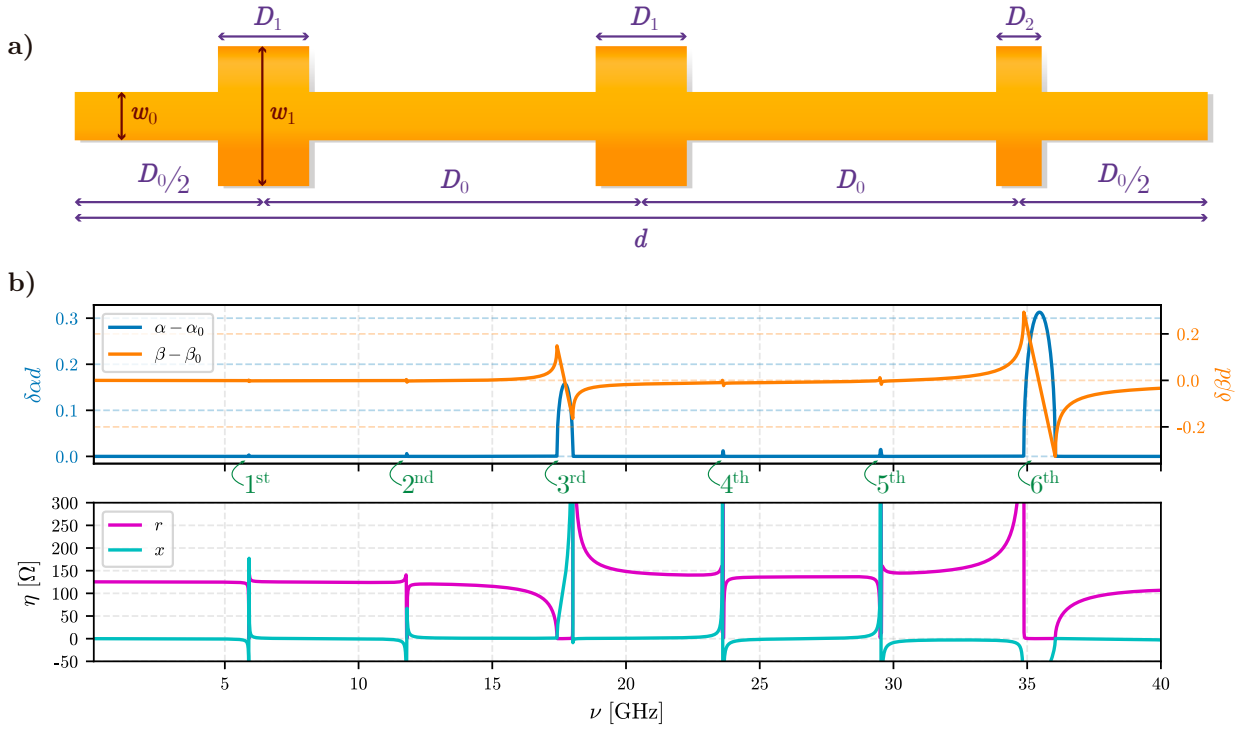

Figure 4.1: (a) Floquet transmission line consisting of a central line of width w_0 and dispersive loads of width w_1. These values, together with the lengths D_0, D_1, and D_2, are given in Table 4.2. (b) Characteristics of the Floquet transmission line for the CPW design. Six stopbands are shown, enumerated (in green) from the 1st up to the 6th. These are determined by $\delta\alpha \equiv \alpha - \alpha_0 \neq 0$, where the subindex "0" indicates "central line". A non-linear dispersion relation is observed, i.e. $\delta\beta \equiv \beta - \beta_0 \neq 0$, and it is steeply changing around the stopbands.

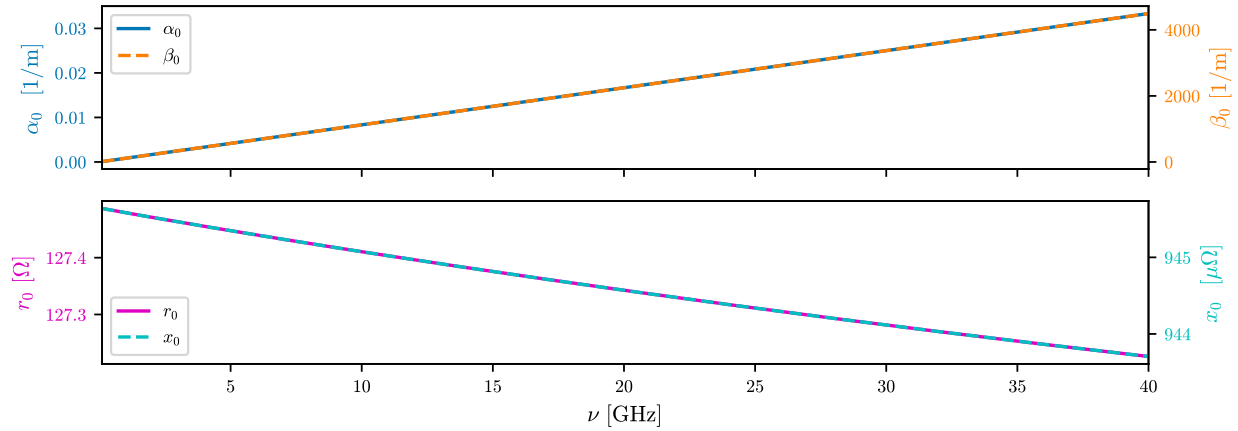

Figure 4.2: Characteristics of the central transmission line (without the dispersive loads) for the CPW design. The attenuation constant, α_0, and the imaginary part of the characteristic impedance, x_0, are nonzero because of dissipation.

s (μm)	t (nm)	T_c (K)	T (K)	ρ_N ($\mu\Omega\cdot$ cm)	ϵ_r –	$\tan\delta$ –
1	35	14.7	0	100	11.44	$1.48351 \cdot 10^{-5}$

Table 4.1: CPW design parameters. The central line's width is $w_0 = 1$ μm.

w_0 (μm)	w_1 (μm)	D_0 (mm)	D_1 (μm)	D_2 (μm)	d (mm)
1	3.4	1.578	60	50	4.734

Table 4.2: Unit cell values that define the Floquet transmission line designed with CPW.

non-linear dispersion relation around these values of ν_p, the dispersive loads are made of a different length every third occurrence, i.e. $D_2 \neq D_1$, which produces smaller stopbands around $n\nu_{\text{per}}/3, n \in \mathbb{N} \setminus \{m\nu_{\text{per}} : m \in \mathbb{N}\}$ [5, 20]. This result can be seen in Figure 4.1.b by observing the position of the stopbands given by $\delta\alpha \equiv \alpha - \alpha_0 \neq 0$, where the subindex "0" indicates "central line". Moreover, it is observed that $\delta\beta \equiv \beta - \beta_0 \neq 0$ and it is steeply changing around the stopbands, which implies a large non-linear dispersion $\beta(\nu)$, which in turn, means a large range of possible linear phase mismatches $\Delta\beta z \equiv \beta_s z + \beta_i z - 2\beta_p z$ for the non-linear amplitude equations, depending on the frequencies of each signal, which allows to enhance the amplification of the target signal [20].

The design is such that for pump frequencies ν_p near the 1$^{\text{st}}$ and 2$^{\text{nd}}$ stopbands, the third harmonic $3\nu_p$ falls inside the 3$^{\text{rd}}$ and 6$^{\text{th}}$ stopbands, respectively. This makes the energy transfer to mainly occur from the pump to the target signal and idler, since $3\nu_p$ is not propagated. Since Eom's paper [20] shows results for ν_p near the 2$^{\text{nd}}$ stopband, this situation is analyzed first in the next section.

4.2 Pump frequency near 2$^{\text{nd}}$ stopband

In order to maximize amplification, freedom in the selection of $\Delta\beta$ is required. This is achieved in zones where $\delta\beta(\nu)$ changes significantly, which happens to be very close to the stopbands. Focusing near the 2$^{\text{nd}}$ stopband, $\delta\beta$ is large enough (despite of looking small compared to near the 6$^{\text{th}}$), as it can be seen in Figure 4.3. In that figure it is also clear that r is close to constant around the 2$^{\text{nd}}$ stopband, useful to avoid losses due to impedance mismatch at the input and output of the KI-TWPA. The study will be done with ν_p smaller than the frequencies of the 2$^{\text{nd}}$ stopband. In order to know which model to use, the zones of dominance for each model are shown in Figure 4.4, where it is clear that the magnitude of the normalized current $\tilde{I} \equiv I/I_*$ can modify the zones, and hence, the model to use. Taking this into consideration, different interesting values of ν_p are selected to simulate the gain of the target signal using all the models for the $s-p-i$ and $s-p-i-3p$ cases, considering $I \approx A_p^0 = 0.2I_*$. These results are shown in Figure 4.5. It is observed that, when the $3p$ signal propagates ($\nu_p = 11.61$ GHz and $\nu_p = 11.62$), the $s-p-i$ wrongly predicts large gain. The difference is very large for the New1, New2, and Old models. Nonetheless, it is not too

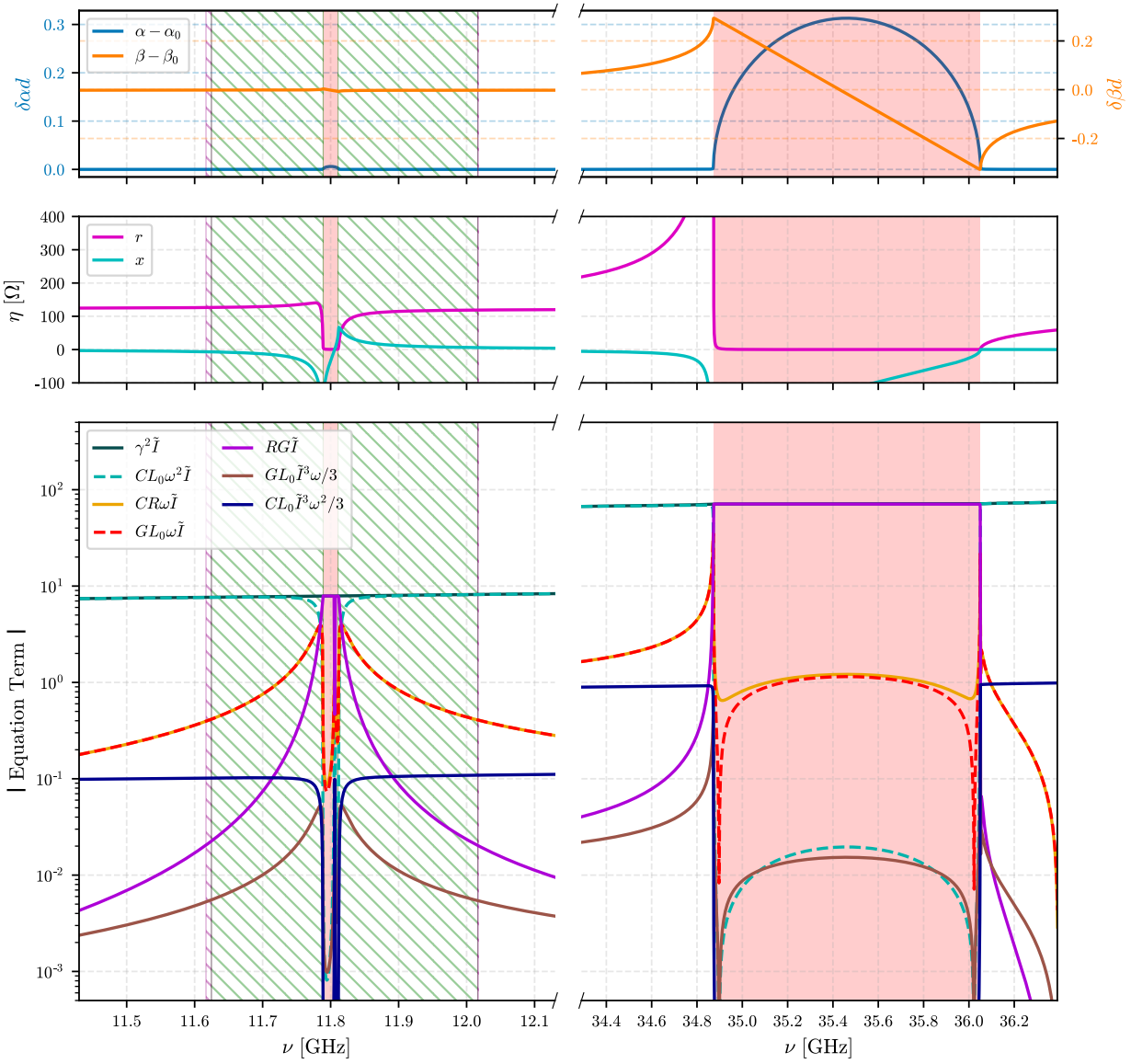

Figure 4.3: Dispersion relation $\{\alpha(\nu), \beta(\nu)\}$ and characteristic impedance $\eta(\nu)$ from Figure 4.1.b, zoomed in around the 2$^{\text{nd}}$ (left column) and 6$^{\text{th}}$ (right column) stopbands (marked as red zones). The magnitudes of the different terms of equation 2.55 are also shown for the case $\tilde{I} \equiv I/I_* = 0.2$. The green dashed zones on the left, correspond to frequencies where its third harmonic 3ν falls in the stopband shown on the right. The purple dashed zones on the left correspond to frequencies such that 3ν falls in a zone outside the stopbands where $|RG\tilde{I}| > |CL_0\tilde{I}^3\omega^2/3|$.

significant in the New3 model (although still exists). At $\nu_p = 11.62$, the $3\nu_p$ frequency is not very well propagated, because it falls in a zone where $|RG\tilde{I}| > |CL_0\tilde{I}^3\omega^2/3|$, meaning that the non-linear effect is not dominant for $3\nu_p$, and the phase mismatch is dominated by the $|RG|$ term in the amplitude equations. Therefore, the difference between the $s-p-i$ simulation and the $s-p-i-3p$ one, is very small in this case. This effect can be seen more clearly in Figure 4.6, where $|A_{3p}|$ is much smaller for $\nu_p = 11.62$ GHz than for $\nu_p = 11.61$

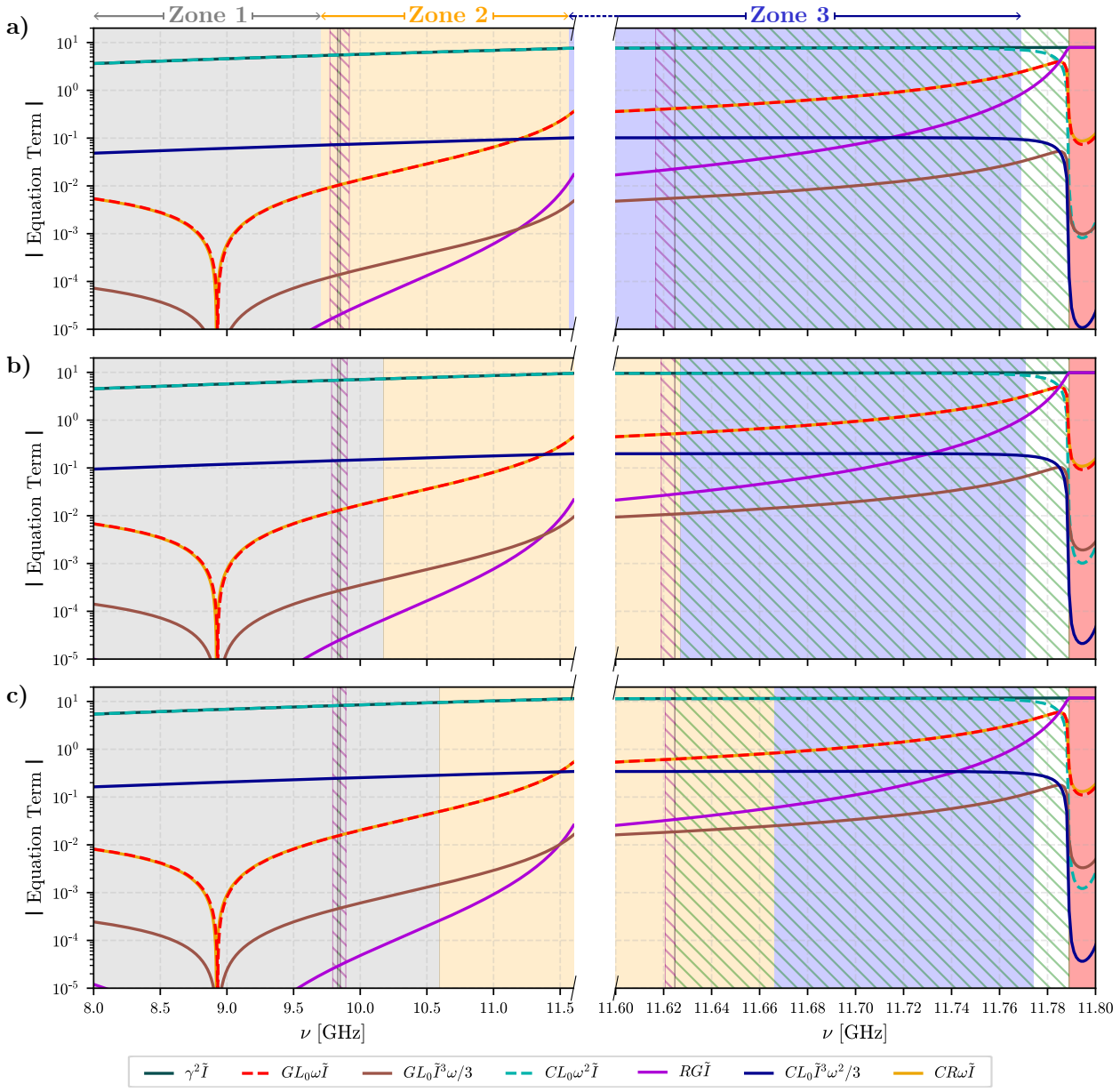

Figure 4.4: Magnitudes of the terms of equation 2.55 near the 2nd stopband. The zones 1, 2, and 3 define the range of frequencies where the models New1, New2, and New3 dominate the dynamics, respectively. The magnitudes of the total current are (a) $\tilde{I} = 0.2$, (b) $\tilde{I} = 0.25$, and (c) $\tilde{I} = 0.3$. It is observed that the zones depend on $\tilde{I}$, moving closer to the stopband as the current magnitude increases. Simultaneously, the region where $|RG\tilde{I}| > |CL_0\tilde{I}^3\omega^2/3|$ shrinks close to the stopband, extending the region where the non-linear term (cause of the amplification) dominates over $|RG\tilde{I}|$.

GHz, in the New3 model.

For pump frequencies that eliminate its 3rd harmonic, $\nu_p = 11.63, 11.68, 11.73$ GHz in Figure 4.5, the $s-p-i$ and $s-p-i-3p$ simulations give the same results in gain of the target signal. Except for the Old model, which does not detect the stopbands in its equation, and hence,

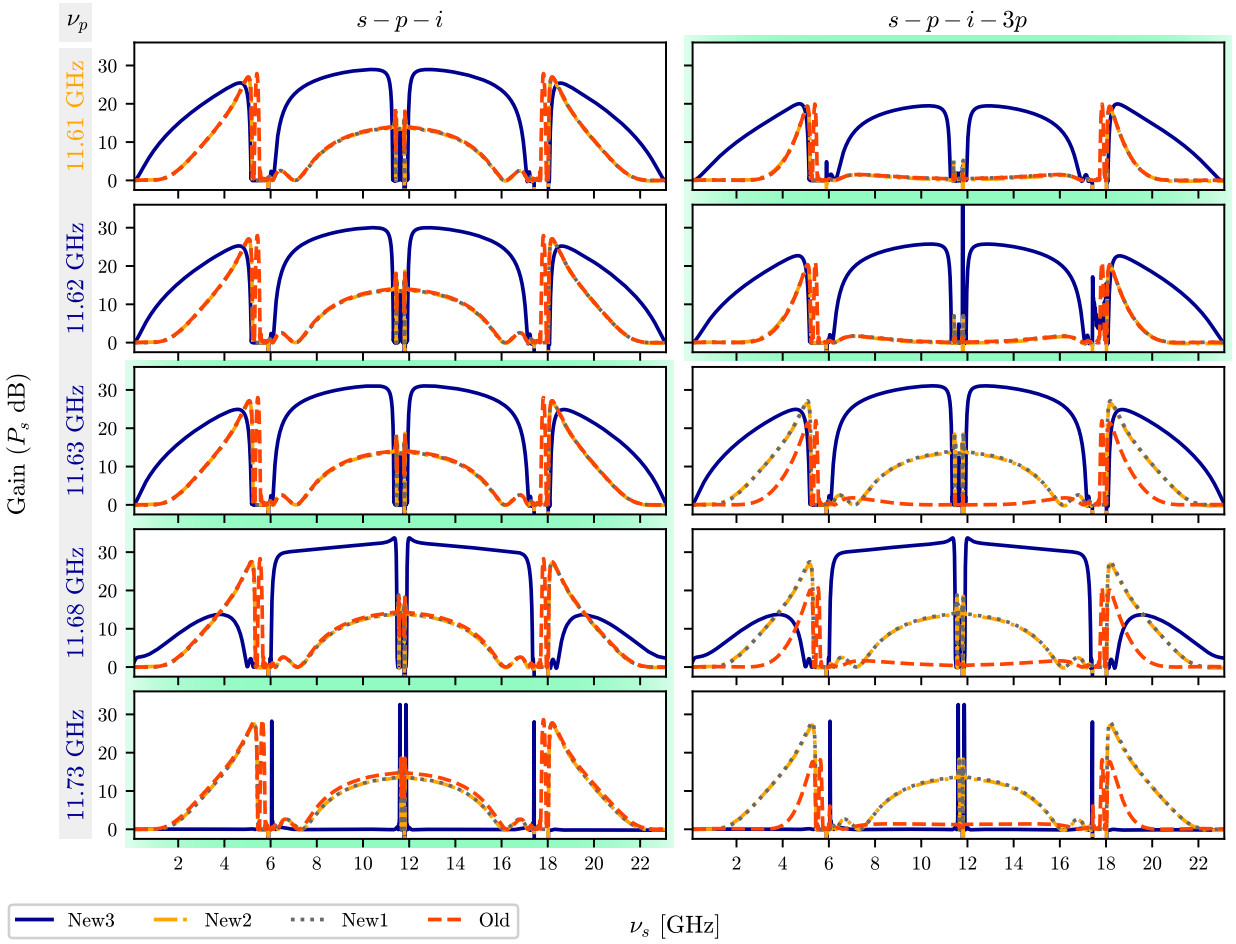

Figure 4.5: Gain of the target signal after traveling $z/d = 150$ unit cells for different values of pump frequency ν_p near the 2nd stopband, using an initial pump amplitude $A_p^0 = 0.2I_*$. The values of ν_p are colored as the corresponding zones from Figure 4.4. The gain obtained with the model associated to each zone shares the same color coding, and the Old model is also plotted in orange. Between the results using $s-p-i$ or $s-p-i-3p$, the case that better represents the dynamics is highlighted in green, which is determined by whether the third harmonic $3\nu_p$ falls in a stopband or not.

does not eliminate the $3p$ signal when it should. This is a good result because it showcases convergence of different simulations in the expected cases. Nonetheless, the $s-p-i$ model is technically more accurate, as it avoids the problem of selecting the correct model for the $3p$ signal that should be tackled in a more detailed model than the presented in this thesis (where each frequency would use the model corresponding to its own, instead of using the one given by the pump, justified here because it dominates in amplitude). Figure 4.6, for $\nu_p = 11.63$ GHz shows how the $|A_{3p}|$ amplitude is negligible because of the stopband, while the Old model shows the amplitude it would have if no stopband where present there for the $3p$ signal.

Focusing on $\nu_p = 11.63$ GHz, Figure 4.7 shows how the New3 model predicts a stable mis-

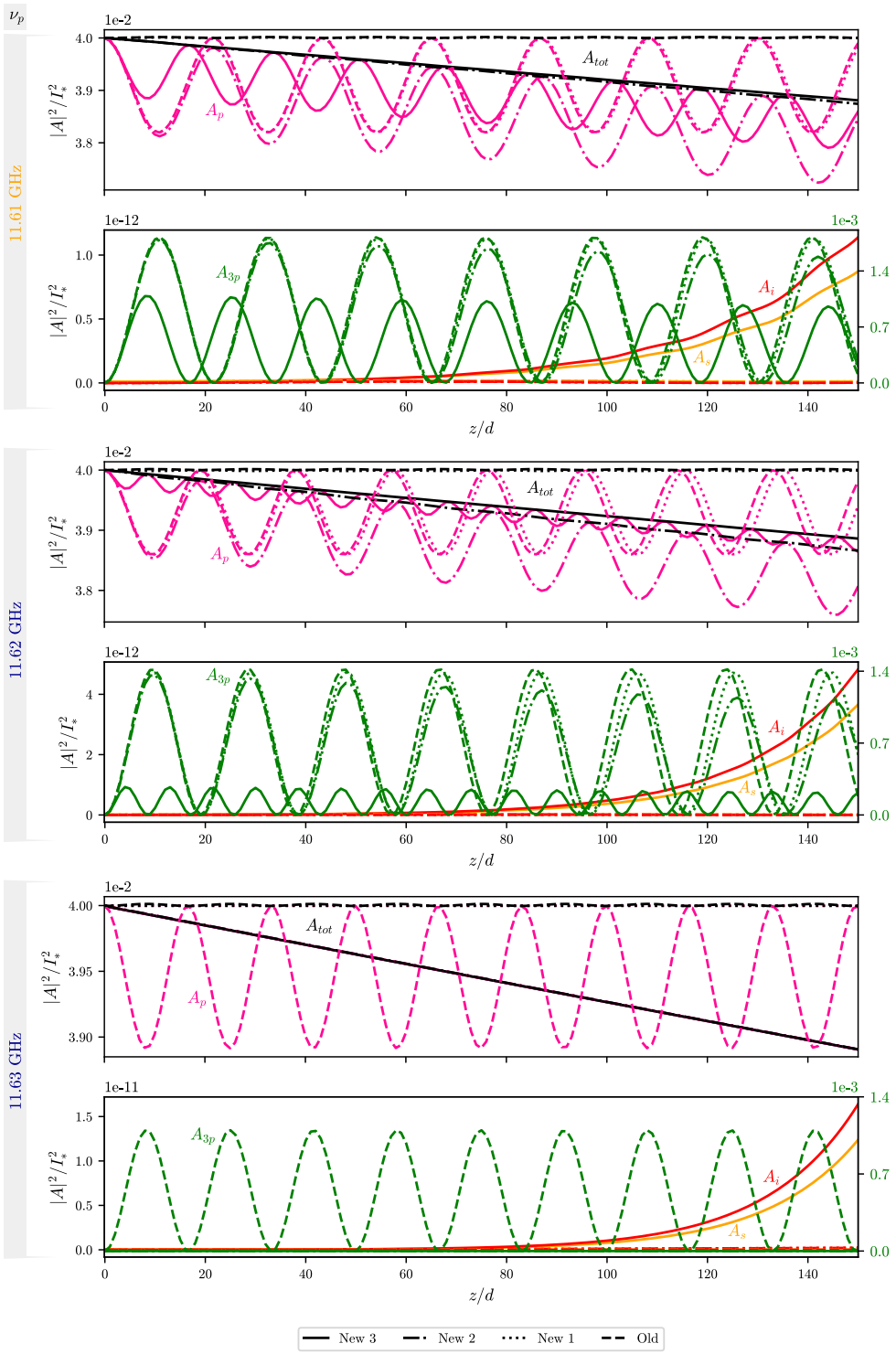

Figure 4.6: Evolution of the amplitudes along $z/d = 150$ unit cells for three key different pump frequencies, $\nu_p = 11.61$ GHz in zone 2, $\nu_p = 11.62$ GHz in zone 3 and in the purple dashed region, and $\nu_p = 11.63$ GHz in zone 3 and in the green dashed region. The initial pump amplitude is $A_p^0 = 0.2I_*$. The case $s - i - p - 3p$ is showed in all plots. It is observed that the $3\nu_p$ signal can be diminished and even neglected depending on the operating region of ν_p.

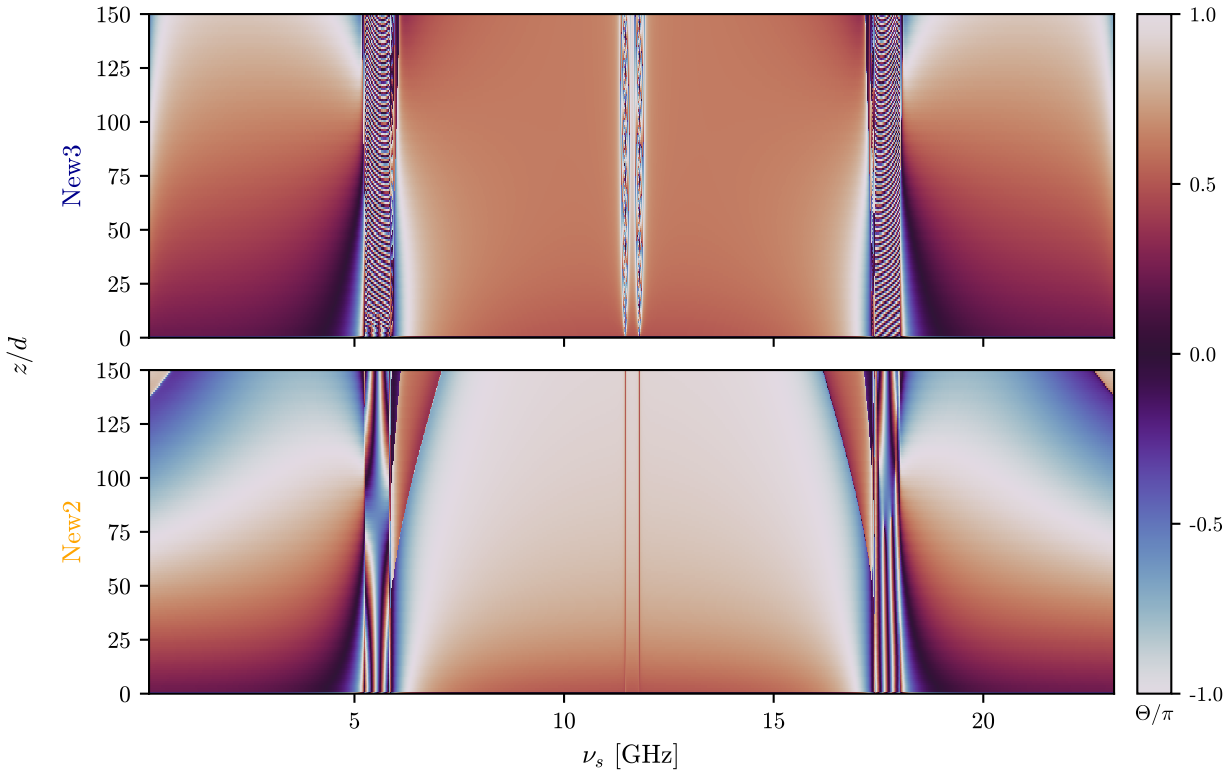

Figure 4.7: Phase mismatch $\Theta(z)$ for target signal frequencies ν_s around the pump frequency $\nu_p = 11.63$ GHz for the New3 and New2 models. It is observed that $\Theta(z)$ is better stabilized near $\pi/2$ along all the evolution in the New3 model, meaning an energy transfer from the pump to the idler and target signals close to the optimal along all z.

match $\Theta(z)$ along z, which is around the optimal value $\pi/2$ for energy transfer towards the target and idler signals. In contrast, the New2 model is not so stable and shows oscillations of $\Theta(z)$ that, in turn, generates various maximums and minimums in the final gain, as seen in Figure 4.5. Therefore, it is concluded in this case that the RG term helps to stabilize the mismatch $\Theta(z)$, allowing to reach higher gain. Figure 4.8 shows how the gain is produced for the New2 and New3 models due to the mismatch $\Theta(z)$ plotted in Figure 4.7.

Finally, still focusing on $\nu_p = 11.63$ GHz, the initial pump amplitude is swept from $0.05I_*$ to $0.4I_*$, obtaining the results showed in Figure 4.9. There, the gain G_s, the maximum gain, the fractional bandwidth B_f, and the **over-5dB-fractional bandwidth** B_{o5f} are plotted. The latter is defined as the range of frequencies around the maximum gain that give a gain over 5 dB, divided by the central frequency of that range.

It must be kept in mind that, although at $\left|A_p^0\right| = 0.2I_*$ the New3 model is the dominant in this case, for larger values of $\left|A_p^0\right|$ this may change, and to be completely sure which model to consider, a more extensive analysis of the zones must be realized. This analysis is not done here as there is still experimental validation required for the models derived in this thesis.

The results shown and explained in this section are qualitatively similar to the experimental

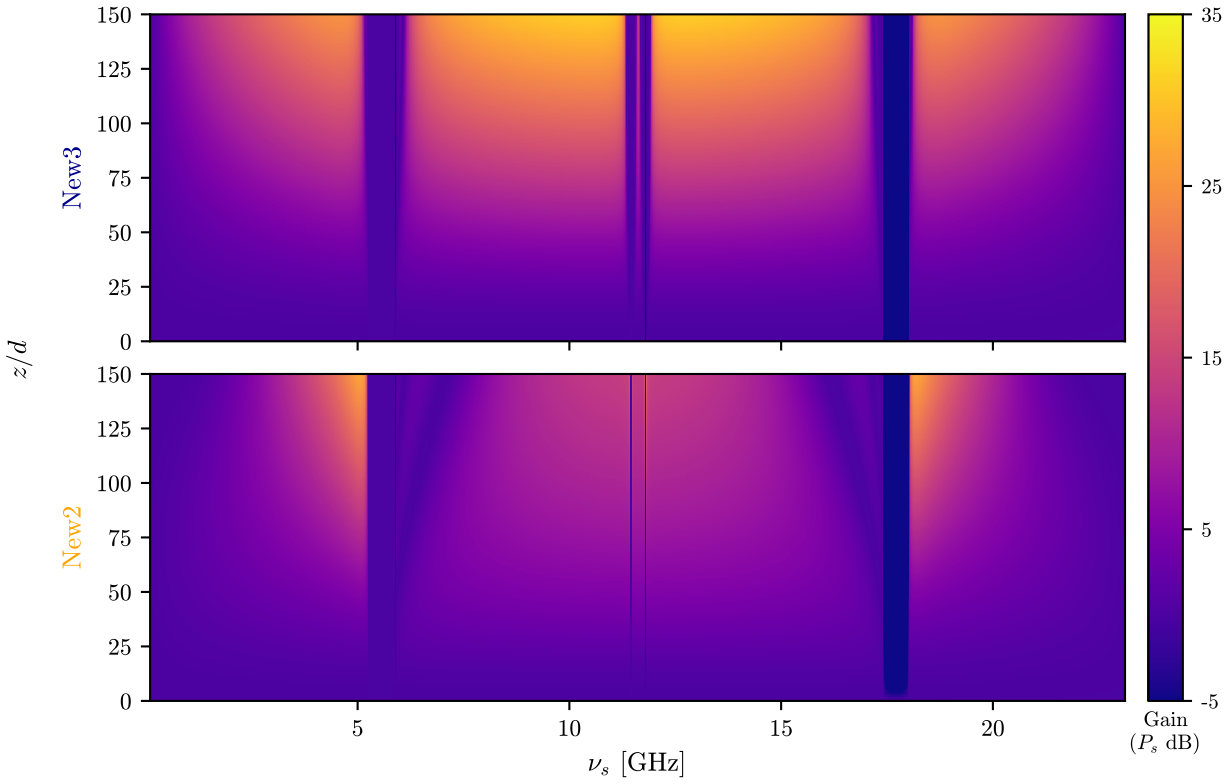

Figure 4.8: Gain of the target signal along z for the same case whose phase mismatch $\Theta(z)$ is plotted in Figure 4.7. The corresponding gain at $z/d = 150$ unit cells is included in Figure 4.5, where the New1 and Old models are also plotted.

ones given by Eom in [20]. Nonetheless, as the designs are not exactly the same, some differences are expected. A particular difference with Eom, is that in his paper no gain could be found near the first stopband, which is not the case of the design presented here[1] (see next section).

On the other hand, the Old model was used in the simulations reported in Eom's paper, in which some parameters were left free in order to better adjust the simulated curves to the experimental data (the specific parameters are not described in the manuscript). The need of performing such adjustment is expected from the results shown in this thesis, where it is clear that the Old model predicts very different curves than the New3 model (see Figure 4.5). It is expected that, if operating in the zone 3, no parameter adjustment would be required when simulating with the New3 model, meaning an improvement with respect to the Old one.

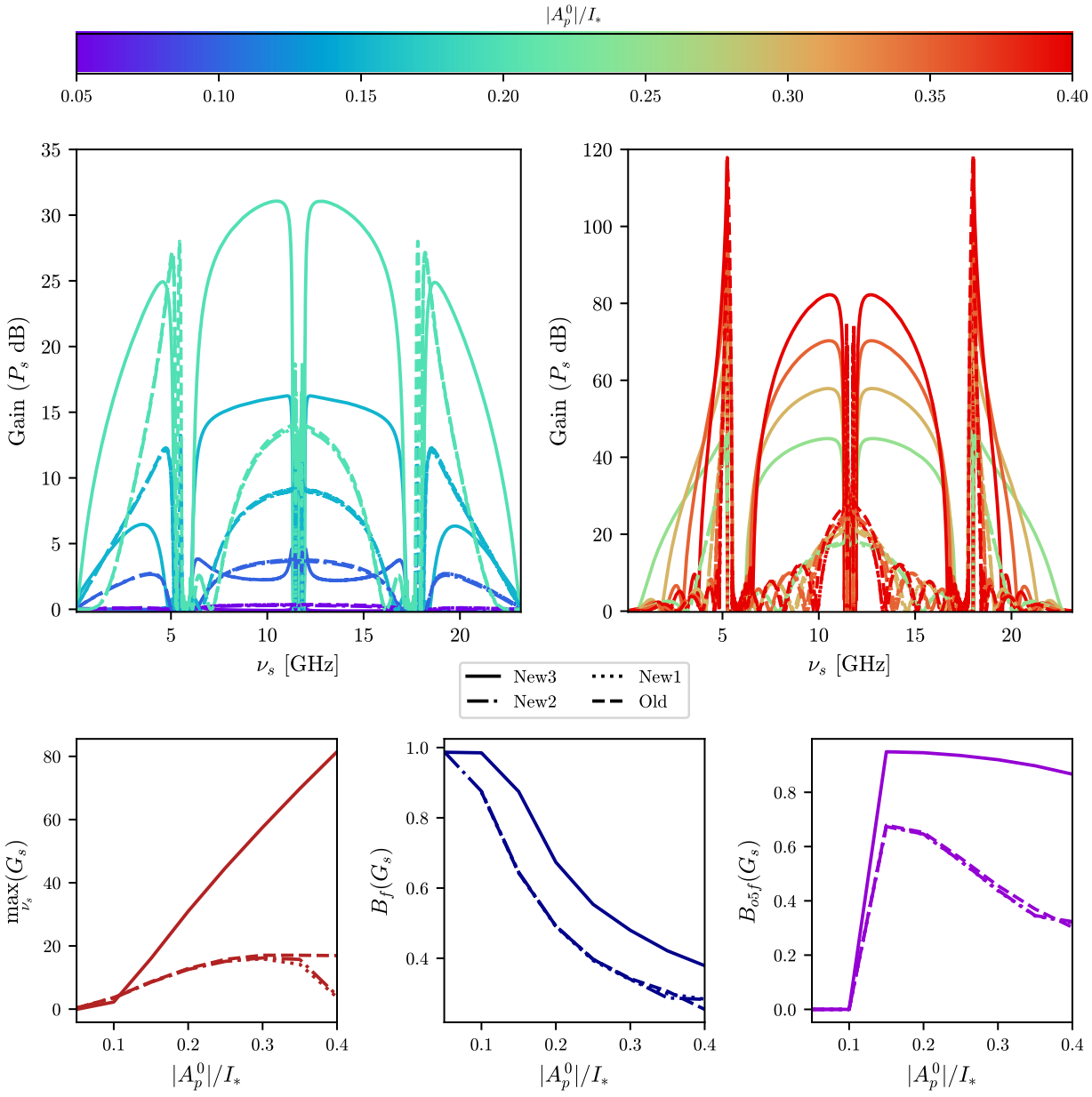

Figure 4.9: Gain of the target signal at $z/d = 150$ and $\nu_p = 11.63$ GHz for various values of initial pump amplitude A_p^0 (top). The maximum gain around the pump frequency, before falling to zero close to 6 GHz and 17 GHz and excluding the center zone where the gain changes curvature, is shown in the bottom left plot. The corresponding fractional bandwidth B_f, and over-5dB-fractional bandwidth B_{o5f} are also shown.

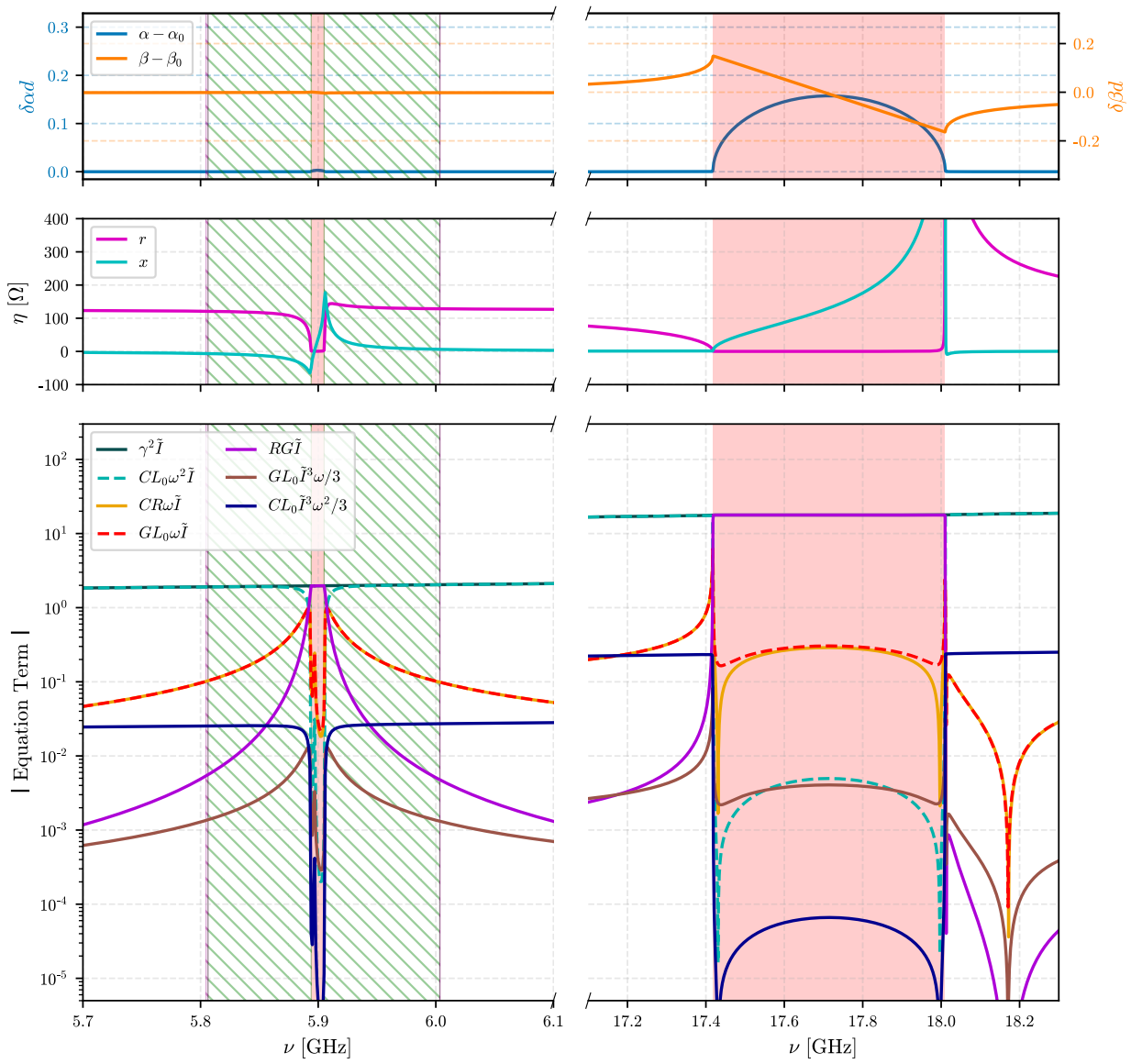

Figure 4.10: Dispersion relation $\{\alpha(\nu), \beta(\nu)\}$ and characteristic impedance $\eta(\nu)$ from Figure 4.1.b, zoomed in around the 1st (left column) and 3rd (right column) stopbands (marked as red zones). The magnitudes of the equation terms are also shown for the case $\tilde{I} \equiv I/I_* = 0.2$. The green dashed zones on the left, correspond to frequencies where its third harmonic 3ν falls in the stopband shown on the right. The purple dashed zones on the left correspond to frequencies such that 3ν falls in a zone outside the stopbands where $|RG\tilde{I}| > |CL_0\tilde{I}^3\omega^2/3|$.

4.3 Pump frequency near 1st stopband

Focusing in selecting ν_p near the 1st stopband, the same type of analysis than explained previously for the 2nd stopband can be done. Figure 4.10 shows a zoom of the characteristics of

[1] Although, during the testing stage of similar designs, there were cases in which no gain could be found near the first stopband, due to a too small $\delta\beta$.

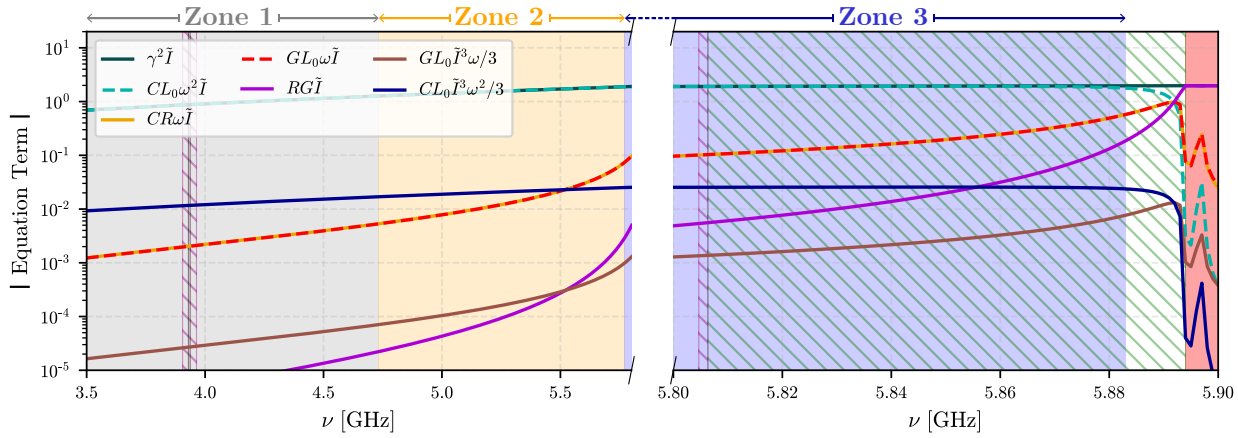

Figure 4.11: Magnitudes of the terms of equation 2.55 near the 1st stopband for $\tilde{I} = 0.2$. The zones 1, 2, and 3 define the range of frequencies where the models New1, New2, and New3 dominate the dynamics, respectively.

the Floquet TL around the frequencies of interest. Figure 4.11 shows the zones for candidate frequencies to be used as ν_p, at $\tilde{I} \approx |A_p^0|/I_* = 0.2$, which is a reasonable value to use in an experiment. Based on what was learned from the previous results and analysis for the 2nd stopband, $\nu_p = 5.81$ GHz is chosen, because it is very close to the critical point where $|RG\tilde{I}| > |CL_0\tilde{I}^3\omega^2/3|$ starts happening, but not there yet. This means that a stabilized $\Theta(z)$ close to optimal should be reached, because ν_p is also in zone 3, while suppressing the $3p$ signal. Indeed, the analysis shows to be successful as very good results are shown in Figure 4.12. In that figure, the results of B_f and B_{o5f} are, in general, larger (i.e. better) than the ones shown in Figure 4.9. This occurs because the bandwidth of interest when operating near the first stopband presents no other stopbands, unlike of when operating near the second stopband.

4.4 Conclusions

In order to improve the gain of the target signal, the pump frequency must be in zone 3, while the third pump's harmonic must be suppressed by a stopband. Additionally, the order of magnitude of the $RG\tilde{I}$ term must be smaller than the one of the $CL_0\tilde{I}\omega^3/3$ term in the non-linear wave equation for the electric current. Fulfilling these design criteria, large amplification of the target signal is expected as long as the dispersion relation $\beta(\nu)$ is highly non-linear around the pump frequency. This last condition is the one that determines whether the operation near the first or the second stopbands produces better results. For the particular design presented in this chapter, both situations predicted very large gain, but the operation near the first stopband achieved in general a larger fractional bandwidth because there were no additional stopbands in the bandwidth of interest. In conclusion, in order to maximize not only the gain, but also the fractional bandwidth, it is recommended to design for operation near the first stopband, at least with the Floquet TL presented in this chapter.

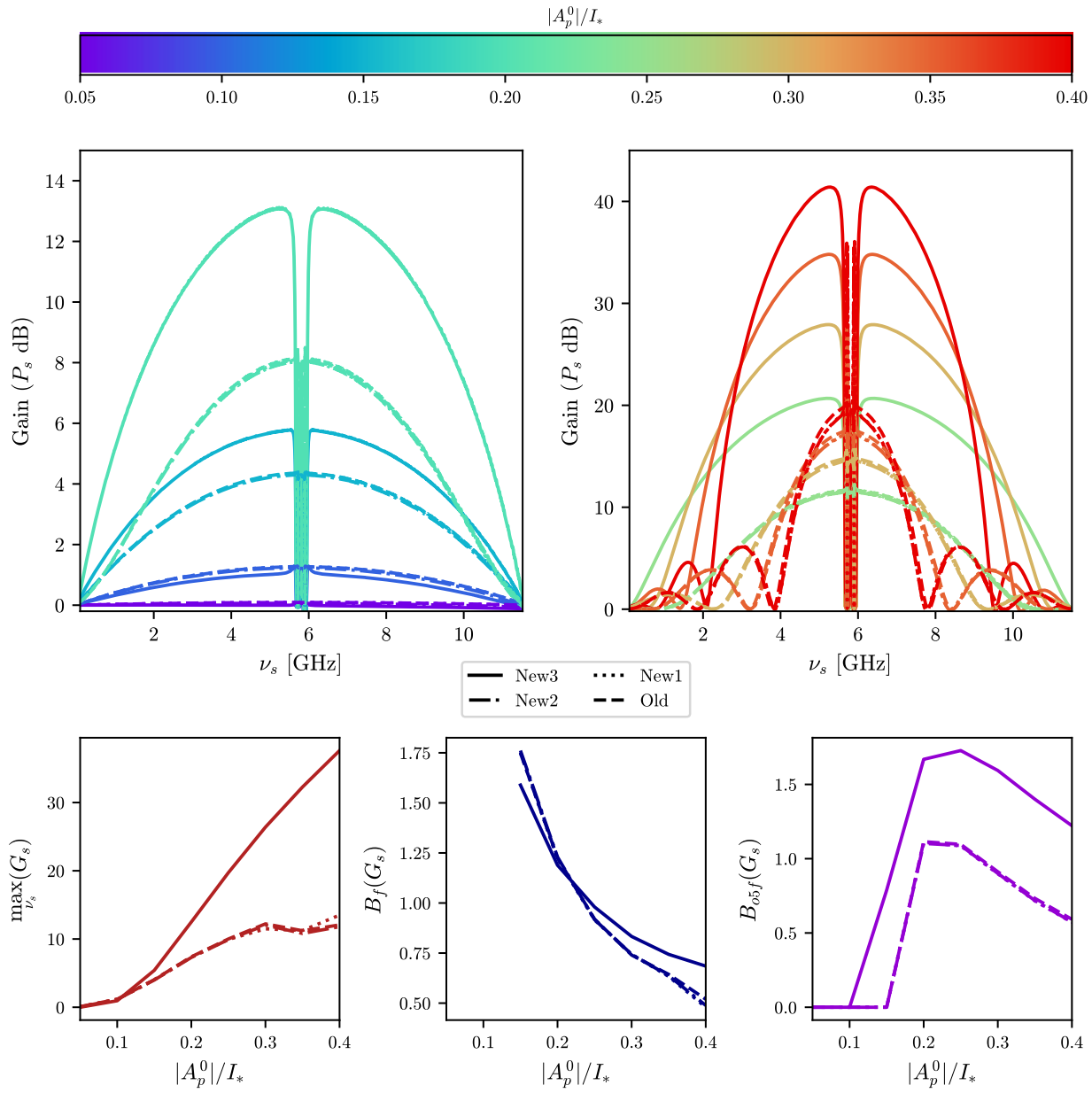

Figure 4.12: Gain of the target signal at $z/d = 150$ and $\nu_p = 5.81$ GHz for various values of initial pump amplitude A_p^0 (top). The maximum gain around the pump frequency, excluding the center zone where the gain changes curvature, is shown in the bottom left plot. The corresponding fractional bandwidth B_f, and over-5dB-fractional bandwidth B_{o5f} are also shown. For $\left|A_p^0\right| < I_*$, the gain is too small along all the values of ν_s plotted, and hence it is not possible to calculate B_f, justifying the missing points.

Chapter 5

Microstrip simulations: a design guide

In this chapter, all the knowledge acquired in chapter 4 is used to make a good design of a KI-TWPA. The new design has large gain and fractional bandwidth, but uses a MS geometry for the TL. This helps to showcase the generality of the analysis and conclusions obtained before, not bounded to a CPW design. Additionally, this is useful because an ideal TL with $r = 50\ \Omega$ is much more practical to achieve with a MS design. Finally, this chapter serves as a general design guide for KI-TWPAs.

5.1 Step 1: obtain large $\delta\beta$

Firstly, an ideal MS design has $\mathrm{Re}\{\eta\} \equiv r = 50\ \Omega$. The Floquet TL to use, depicted in Figure 5.1.a, is of the same type as the already used and explained with detail in chapter 4 for the CPW design. Then, for a MS, $w_1 > w_0$ implies that $r_0 > r_1$, where the subindices "0" and "1" refer to the central line and the dispersive loads, respectively. Therefore, the real part of the Floquet characteristic impedance r is a value $r_1 < r < r_0$. Consequently, a value of r_0 slightly above 50 Ω is required in order to obtain a value of $r \approx 50\ \Omega$. Hence, a MS design with the characteristics of the central line shown in Figure 5.2 is obtained with $w_0 = 1\ \mu$m and the design parameters shown in Table 5.1, where the substrate's height h, the superconducting strip's thickness t, the superconductor's critical temperature T_c, the operation temperature T, the superconductor's normal resistivity ρ_N, the substrate's dielectric constant ϵ_r, and the loss-tangent $\tan\delta$ are presented. The design parameters consider the use of NbTiN as the superconducting material, and a-Si:H as the substrate material. Ideally, a smaller value of h should be used, but this would imply the need for a smaller value of w_0 in order to keep the same r_0, which is not practical since $w_0 = 1\ \mu$m is near the limit of feasible fabrication.

On the other hand, if a smaller value of r_0, even closer to 50 Ω, were to be used, a smaller value of w_1 (closer to w_0) would be needed in order to maintain $r \approx 50\ \Omega$, which would result in smaller stopbands and a smaller non-linear dispersion relation $\delta\beta(\nu)$ near the stopbands. Hence, at first glance, this means that a smaller gain of the target signal would be achieved, and it could even get negligible if $\delta\beta(\nu)$ is too small. However, in some cases this could be favorable by moving the stopbands' ranges in such a way that the regions of frequencies for ν_p that suppress its third harmonic $3\nu_p$ are in a better zone, defined from the orders of

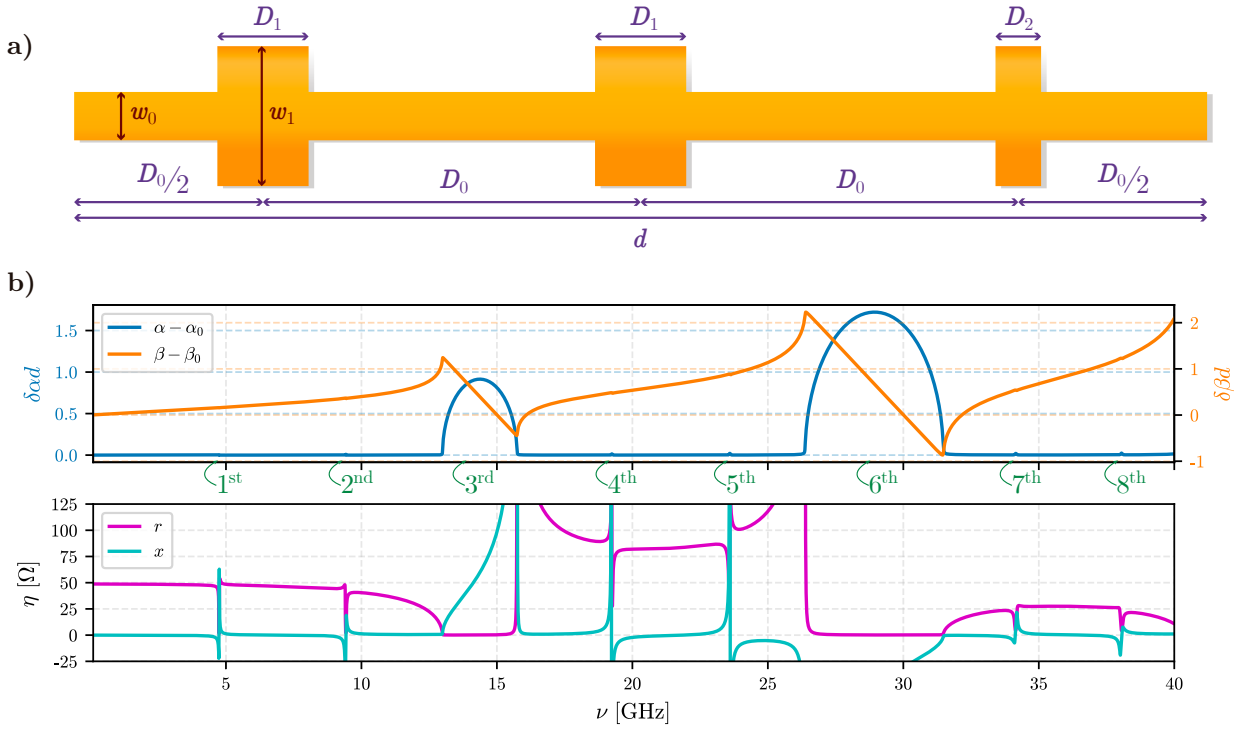

Figure 5.1: (a) Floquet transmission line consisting of a central line of width w_0 and dispersive loads of width w_1. These values, together with the lengths D_0, D_1, and D_2, are given in Table 4.2. (b) Characteristics of the Floquet transmission line for the microstrip design. Eight stopbands are shown, enumerated (in green) from the 1st up to the 8th.

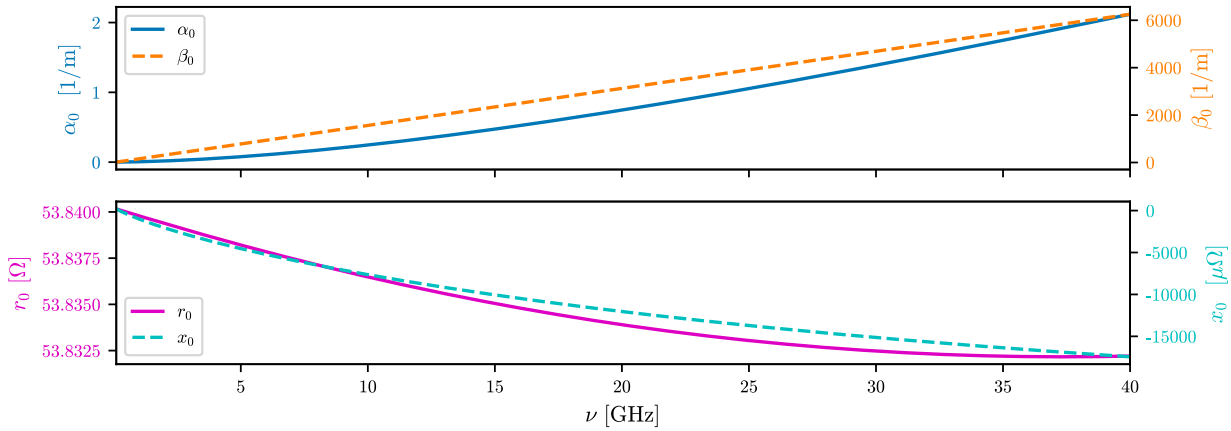

Figure 5.2: Characteristics of the central transmission line (without the dispersive loads) for the microstrip design.

magnitude of the non-linear wave equation terms, while still keeping large enough $\delta\beta(\nu)$. The latter situation, though, is in general not happening or its effect is overcome by the larger $\delta\beta(\nu)$ obtained otherwise. Therefore, the general advice is to still design for a large $\delta\beta(\nu)$. This means, in the case of a MS design, to make w_1 considerably larger than w_0. In general

h (nm)	t (nm)	T_c (K)	T (K)	ρ_N ($\mu\Omega\cdot$ cm)	ϵ_r –	$\tan\delta$ –
300	60	14.7	4	132	11.44	$1.48351 \cdot 10^{-5}$

Table 5.1: Microstrip design parameters. The central line's width is $w_0 = 1$ μm.

w_0 (μm)	w_1 (μm)	D_0 (mm)	D_1 (μm)	D_2 (μm)	d (mm)
1	4	1.34	100	95	4.02

Table 5.2: Unit cell values that define the Floquet transmission line designed with microstrip.

terms, this means to make $|r_0 - r_1|$ a large value.

Understanding the previous analysis, it is justified to design the MS Floquet TL with the unit cell parameters shown in Table 5.2, where $w_1 = 4w_0$. This generates the characteristics shown in Figure 5.1.b.

5.2 Step 2: suppress $3\omega_p$ with ω_p in zone 3 where the non-linear term is larger than RG term

From the designed given in the previous section, the orders of magnitude of the non-linear equation terms in the frequency regions of interest are calculated and shown in Figures 5.3 and 5.4. The green dashed regions are the regions where to put the pump frequency ν_p in order to suppress the $3p$ signal (with frequency $3\nu_p$), and hence, obtain larger gain of the target signal.

The design must be done in such a way that the green dashed regions are large enough so that it includes regions where $|CL_0\tilde{I}^3\omega/3| > |RG\tilde{I}|$, which are the regions that, if the pump frequency is there, generate gain of the target signal, based on the results and analysis from chapter 4. This depends on the value used for $I \approx \left|A_p^0\right|$, and it is easier to achieve for larger I. Hence, the design must be done thinking in the smallest value of $\left|A_p^0\right| \approx I$ that will be used. A reasonable value is $\left|A_p^0\right| = 0.2I_*$. Although, it must be kept in mind that, using smaller values of initial pump magnitude $\left|A_p^0\right|$ implies that the gain of target signal will increase more slowly as the wave travels through the KI-TWPA. Hence, if a specific amount of gain is desired, a situation with smaller $\left|A_p^0\right| \approx I$ requires longer total length of the Floquet TL, i.e. more unit cells.

The design explained so far for the MS geometry, is one of the best obtained during the design process in which the parameters were being tuned. This explains why the green dashed regions are so wide in Figures 5.3 and 5.4, including large regions where $|CL_0\tilde{I}^3\omega/3| > |RG\tilde{I}|$ is fulfilled. This was mainly achieved by setting a value D_2 very similar to D_1, as can be seen in Table 5.2. Indeed, after trial and error, it was found that when D_2 is not close to D_1, like for example, if $D_2 = D_1/2$, the widths of the 3$^{\text{rd}}$ and 6$^{\text{th}}$ stopbands are smaller, which imply

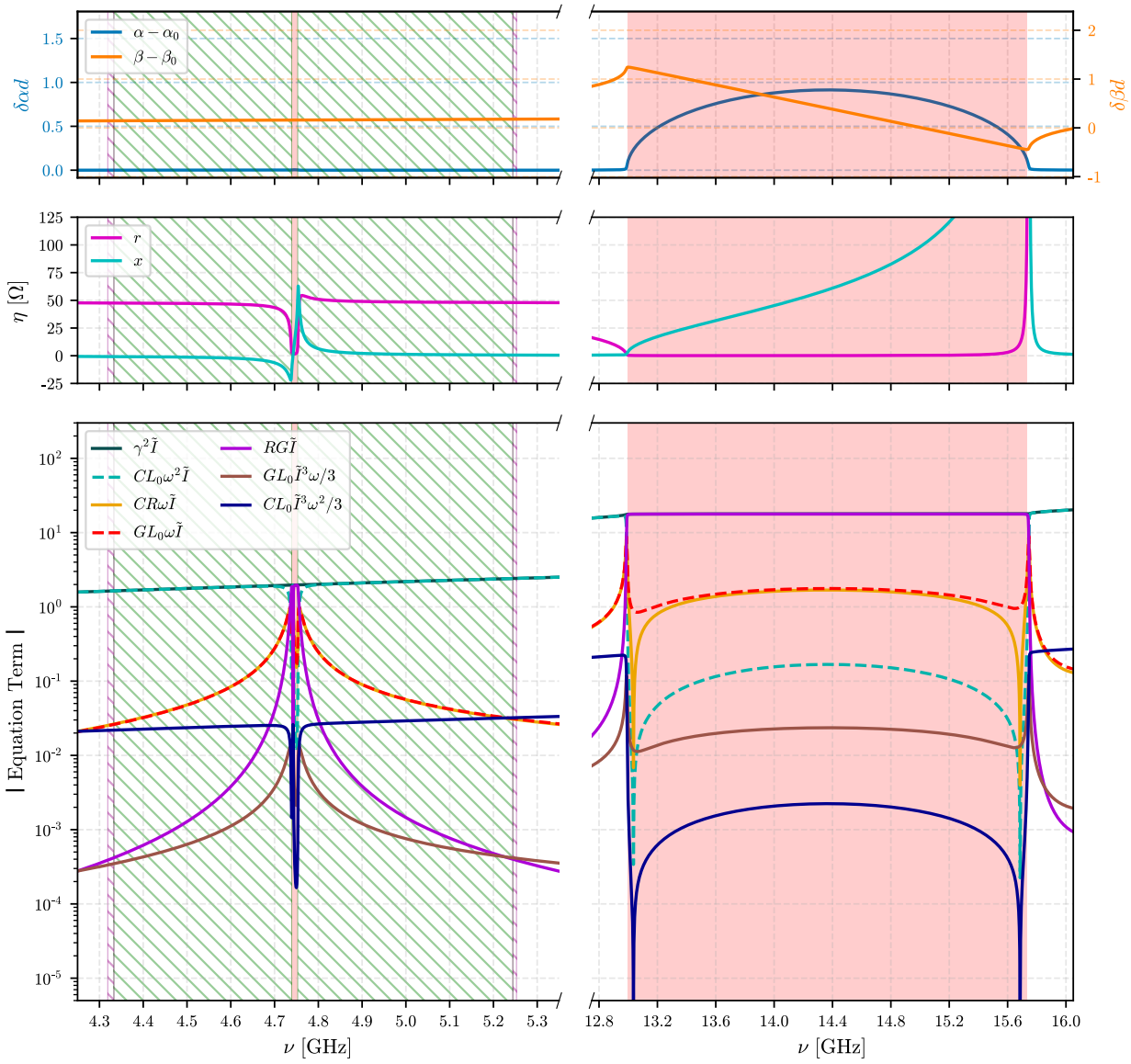

Figure 5.3: Dispersion relation $\{\alpha(\nu), \beta(\nu)\}$ and characteristic impedance $\eta(\nu)$ from Figure 5.1.b, zoomed in around the 1st (left column) and 3rd (right column) stopbands (marked as red zones). The magnitudes of the equation terms are also shown for the case $\tilde{I} \equiv I/I_* = 0.2$. The green dashed zones on the left, correspond to frequencies where its third harmonic 3ν falls in the stopband shown on the right. The purple dashed zones on the left correspond to frequencies such that 3ν falls in a zone outside the stopbands where $|RG\tilde{I}| > |CL_0\tilde{I}^3\omega^2/3|$.

smaller ranges for the dashed green regions.

Furthermore, the pump frequency ν_p not only should be in a green dashed region where $|CL_0\tilde{I}^3\omega/3| > |RG\tilde{I}|$, but should also be in the zone 3 (see Figures 5.5 and 5.6). This zone gets smaller as $\left|A_p^0\right| \approx I$ is increased. Hence, the optimal design must be done considering the values of $\left|A_p^0\right|$ to be used in the experiment, because for larger values a transition from zone 3 into zone 2 might occur, resulting less gain.

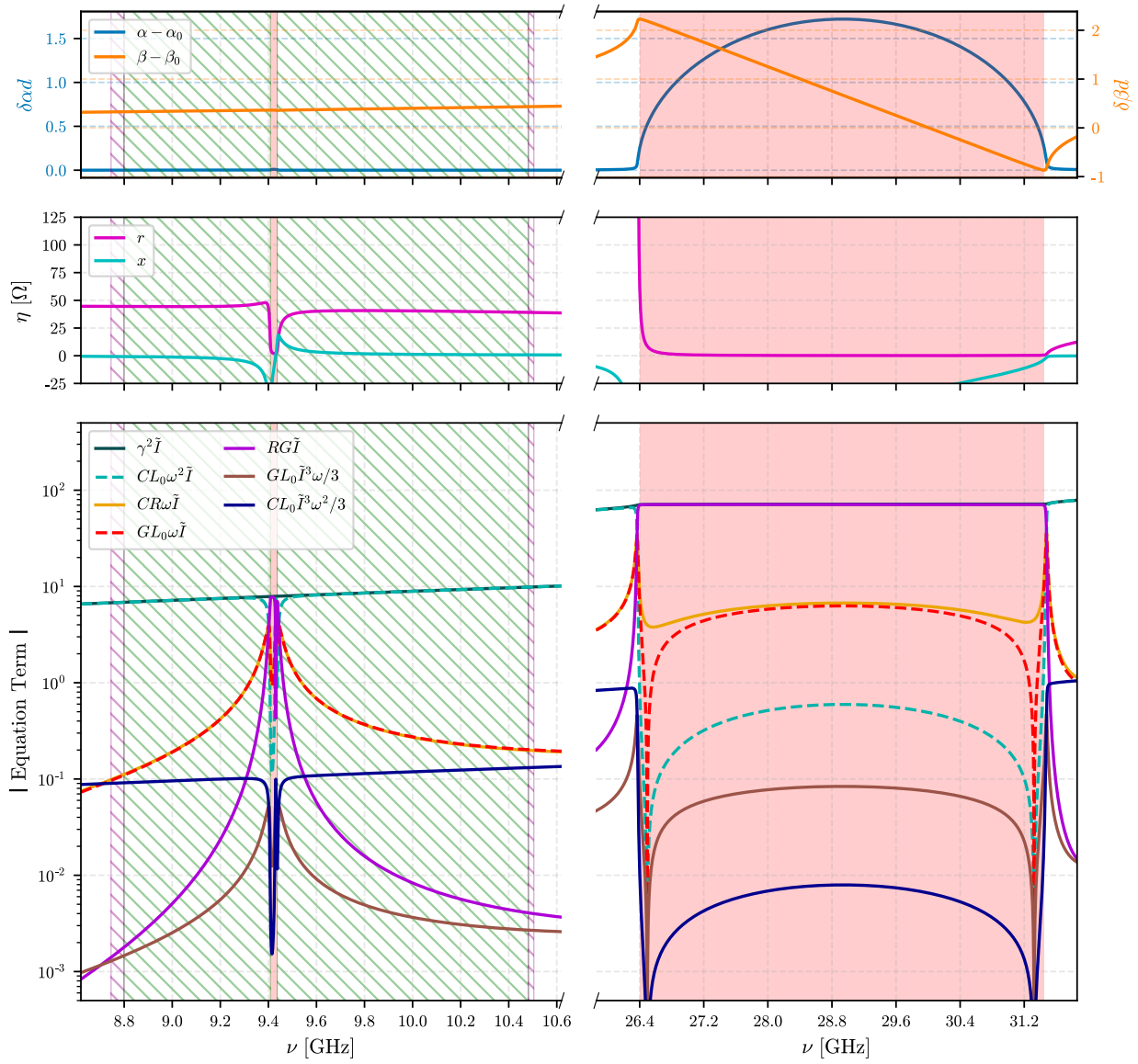

Figure 5.4: Dispersion relation $\{\alpha(\nu), \beta(\nu)\}$ and characteristic impedance $\eta(\nu)$ from Figure 5.1.b, zoomed in around the 2$^{\text{nd}}$ (left column) and 6$^{\text{th}}$ (right column) stopbands (marked as red zones). The magnitudes of the equation terms are also shown for the case $\tilde{I} \equiv I/I_* = 0.2$. The green dashed zones on the left, correspond to frequencies where its third harmonic 3ν falls in the stopband shown on the right. The purple dashed zones on the left correspond to frequencies such that 3ν falls in a zone outside the stopbands where $|RG\tilde{I}| > |CL_0\tilde{I}^3\omega^2/3|$.

Finally, in order to avoid a too large gap at the center of the gain versus frequency plots, ν_p should be positioned the closest possible to the corresponding stopband, keeping inside the zone 3 and fulfilling $|CL_0\tilde{I}^3\omega/3| > |RG\tilde{I}|$. This situation can be enhanced, i.e. one can get closer to the stopband with ν_p, as $\left|A_p^0\right|$ is increased. However, using values of $\left|A_p^0\right| > 0.2$ means getting closer to the critical current $I_c \approx I_*\sqrt{\alpha_*}$, and caution must be taken in order to not leave the superconducting state of the conductors in the KI-TWPA.

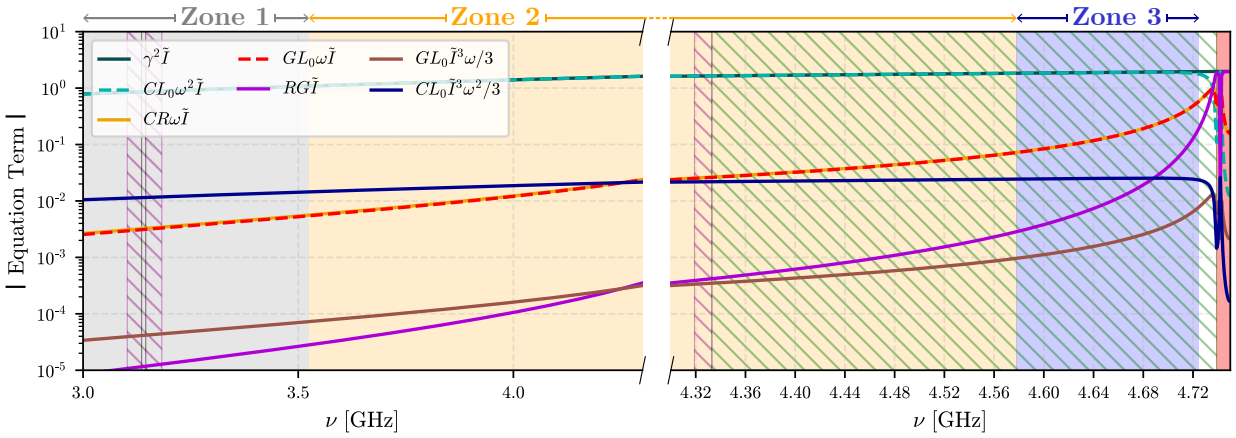

Figure 5.5: Magnitudes of the equation terms near the 1st stopband for $\tilde{I} = 0.2$. The zones 1, 2, and 3 define the range of frequencies where the models New1, New2, and New3 dominate the dynamics, respectively.

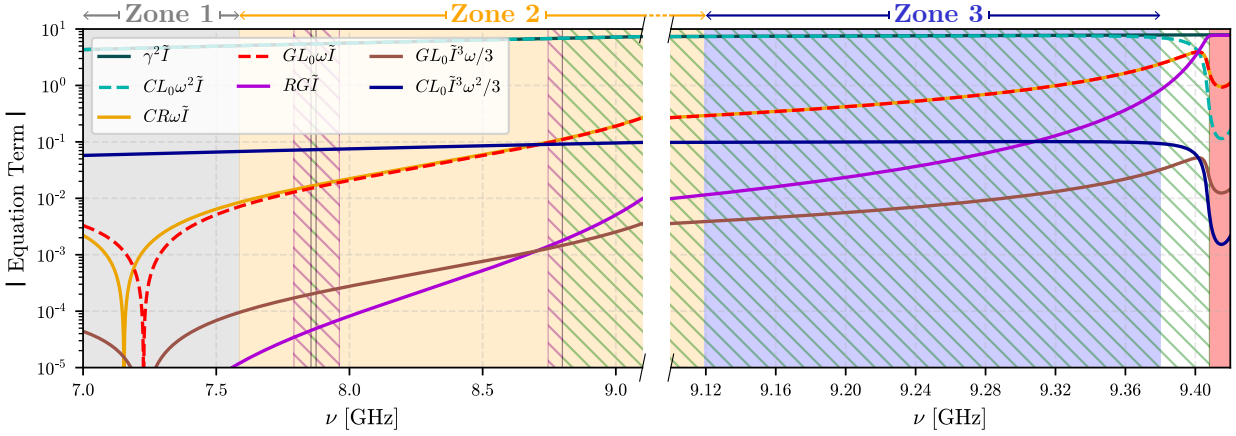

Figure 5.6: Magnitudes of the equation terms near the 2nd stopband for $\tilde{I} = 0.2$. The zones 1, 2, and 3 define the range of frequencies where the models New1, New2, and New3 dominate the dynamics, respectively.

5.3 Gain results

Following the process explained in previous sections, the realized design is fully justified with a high expectation of achieving large gain of the target signals. Indeed, operating near the 1st stopband with $\nu_p = 4.67$ GHz, very good results are obtained and shown in Figure 5.7, showcasing large gain and fractional bandwidth. Operating near the 2nd stopband with $\nu_p = 9.3$ GHz, some good results in gain are obtained (see Figure 5.8), but the fractional bandwidths are smaller, sometimes even not possible to straightforwardly define due to deformation of the gain shape. The deformation at the lower values of $\left|A_p^0\right|$ is attributed to the fact that the pump frequency is not close enough to the stopband, which changes the frequency values at

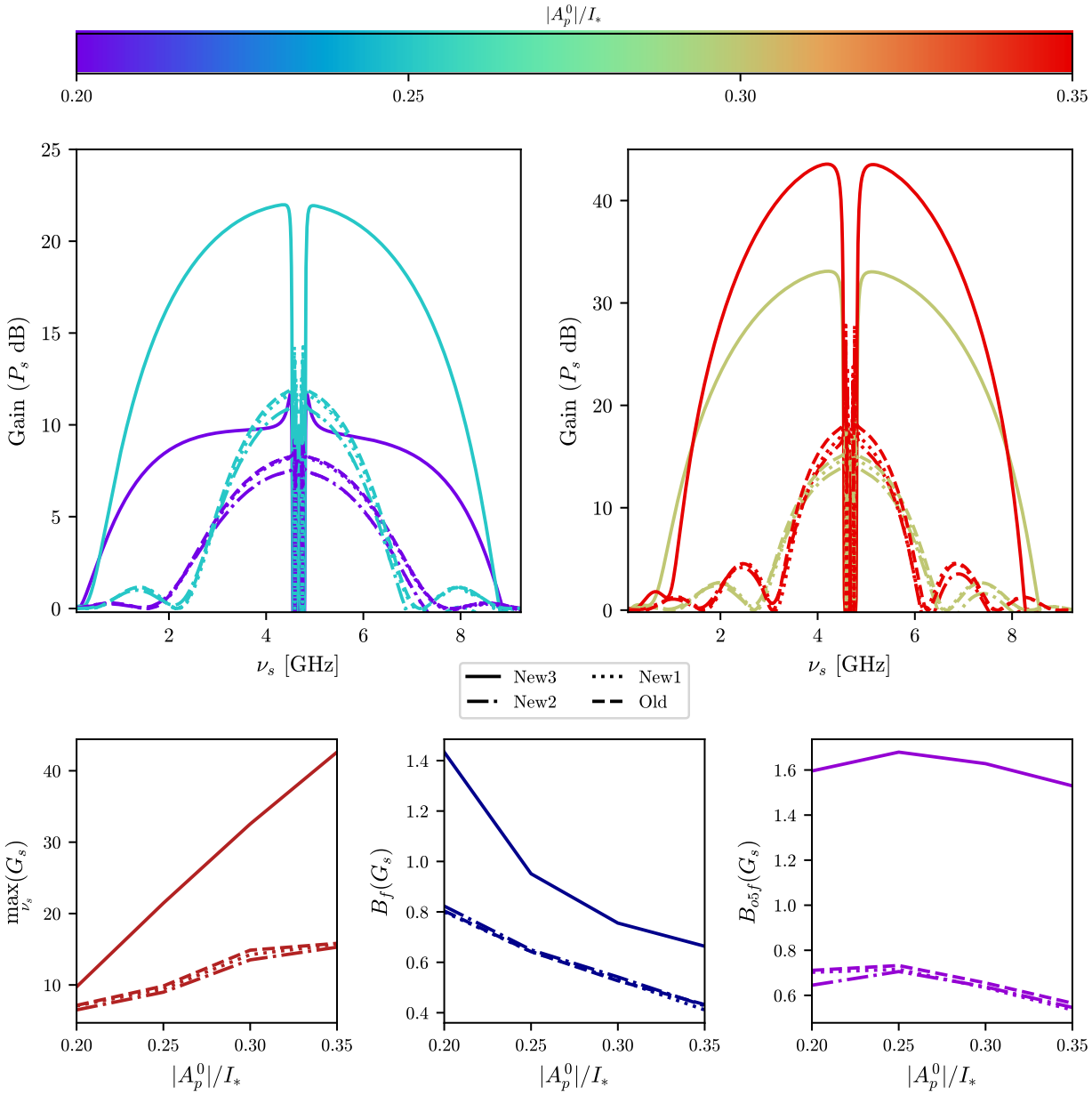

Figure 5.7: Gain of the target signal at $z/d = 150$ and $\nu_p = 4.67$ GHz for various values of initial pump amplitude A_p^0 (top). The maximum gain around the pump frequency, excluding the center zone where the gain changes curvature, is shown in the bottom left plot. The corresponding fractional bandwidth B_f, and over-5dB-fractional bandwidth B_{o5f} are also shown.

which the linear phase shift $\Delta\beta$ is greater. Instead, the reduction in fractional is explained by the fact that the 6$^{\text{th}}$ stopband designed was too big, occupying too much of the range of frequencies near the operation frequency of ν_p.

With this information, there are two possible options to enhance the gain when operating near 10 GHz. The first one is to make a redesign, changing the values of D_0 so that the

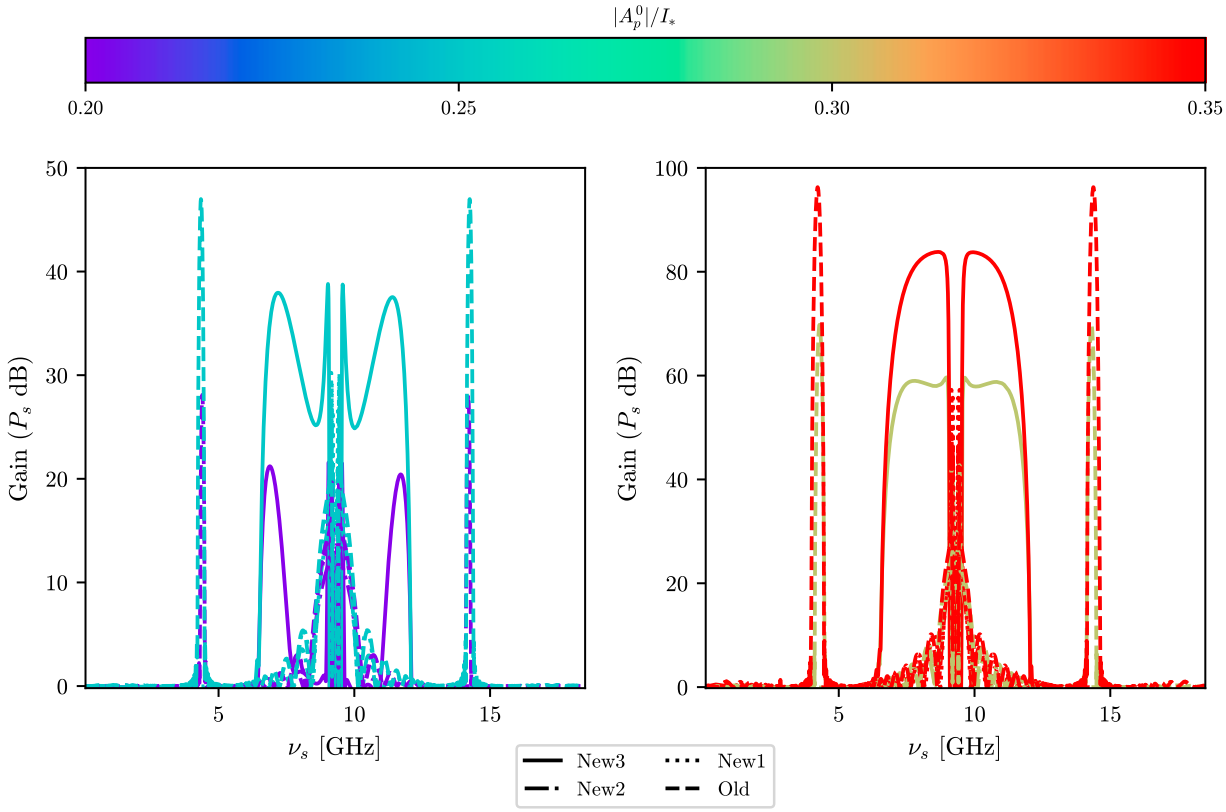

Figure 5.8: Gain of the target signal at $z/d = 150$ and $\nu_p = 9.3$ GHz for various values of initial pump amplitude A_p^0. The maximum gain around the pump frequency, as well as the corresponding fractional bandwidth B_f, and over-5dB-fractional bandwidth B_{o5f} are not calculated here because it is not straightforward to define them in this case where the shapes differ too much from Lorentzian curves, unlike previous results.

first stopband appears at around 10 GHz. The second one is to optimize the design for the second stopband, disregarding the operation near the first stopband, by following the steps described throughout this chapter in order to make the 6^{th} stopband smaller.

5.4 Conclusions

By following the design steps described in this chapter, large gains of the target signal were obtained. The operation near the first stopband resulted specially good, showing also large fractional bandwidth and large over-5dB-fraction bandwidth. In accordance with the conclusions of chapter 4, the apparent (as they are harder to define with precision) fractional bandwidths obtained when operating near the second stopband, are smaller. Furthermore, the shape of the gain plot got distorted beyond the acceptable. This happened because, during the design process, the focus was on obtaining large $\delta\beta$, which resulted in a too large third stopband that occupies too much range of the bandwidth of interest. Therefore, if the operation frequency is desired to be around 10 GHz, a redesign must be done, either by disregarding the operation near the first stopband around 5 GHz or by moving the stopbands

so that the first one were to be around 10 GHz. If a decent gain is desired for operation near both of the stopbands, though, a finer tuning of the parameters is to be done, following the steps described in chapter 5.

Chapter 6

Artificial-CPW simulations: for future experimental validation of the models

In the Microwave Lab of the Radio Astronomical Instrumentation Group research group in which this thesis was developed, a colleague, Daniel Valenzuela (PhD student), designed a Floquet transmission line using **artificial CPW** instead of CPW in order to obtain a 50 Ω impedance [6]. What an artificial CPW line is, escapes the scope of this thesis. However the structure of the design is shown in Figure 6.1. Furthermore, the data from this design is used in this chapter in order to predict the gain results to soon measure in the lab, and thus, validate the models developed in this thesis.

Daniel's design and its characteristics are shown in Figures 6.2 and 6.3, whose unit cell parameters are given in Table 6.1. This design was made to operate amplifying frequencies near the 1st stopband. Hence, the analysis will be focused in this region.

6.1 Pump frequency near 1st stopband

The characteristics of the design near the 1st stopband are shown in Figure 6.4. The zones for different values of $\tilde{I} \approx \left|A_p^0\right|/I_*$ are shown in Figures 6.5 and 6.6, showing that for a given pump frequency ν_p (to be selected) the corresponding zone can change quickly by increasing $\left|A_p^0\right|$. But also, a separation if the purple dashed region occurs, which would drastically ruin the amplification if ν_p were set there.

Three interesting values of ν_p are detected for future experimental verification:

1. $\nu_p = 1.71$ GHz, which is inside a green dashed region a bit far from the 1st stopband (the one close to the stopband is in a region with $|RG\tilde{I}| > |CL_0\tilde{I}^3\omega^2/3|$, hence no gain should be obtained based on the previous analysis) fulfilling that $3\nu_p$ falls inside the 2nd stopband.

2. $\nu_p = 2.15$ GHz, which is the closest to the 1st stopband before entering the critical zone where $|RG\tilde{I}| > |CL_0\tilde{I}^3\omega^2/3|$. At this value of ν_p, since it is in a dashed purple region, the third harmonic $3\nu_p$ is not suppressed, but it is diminished. Nonetheless, its results

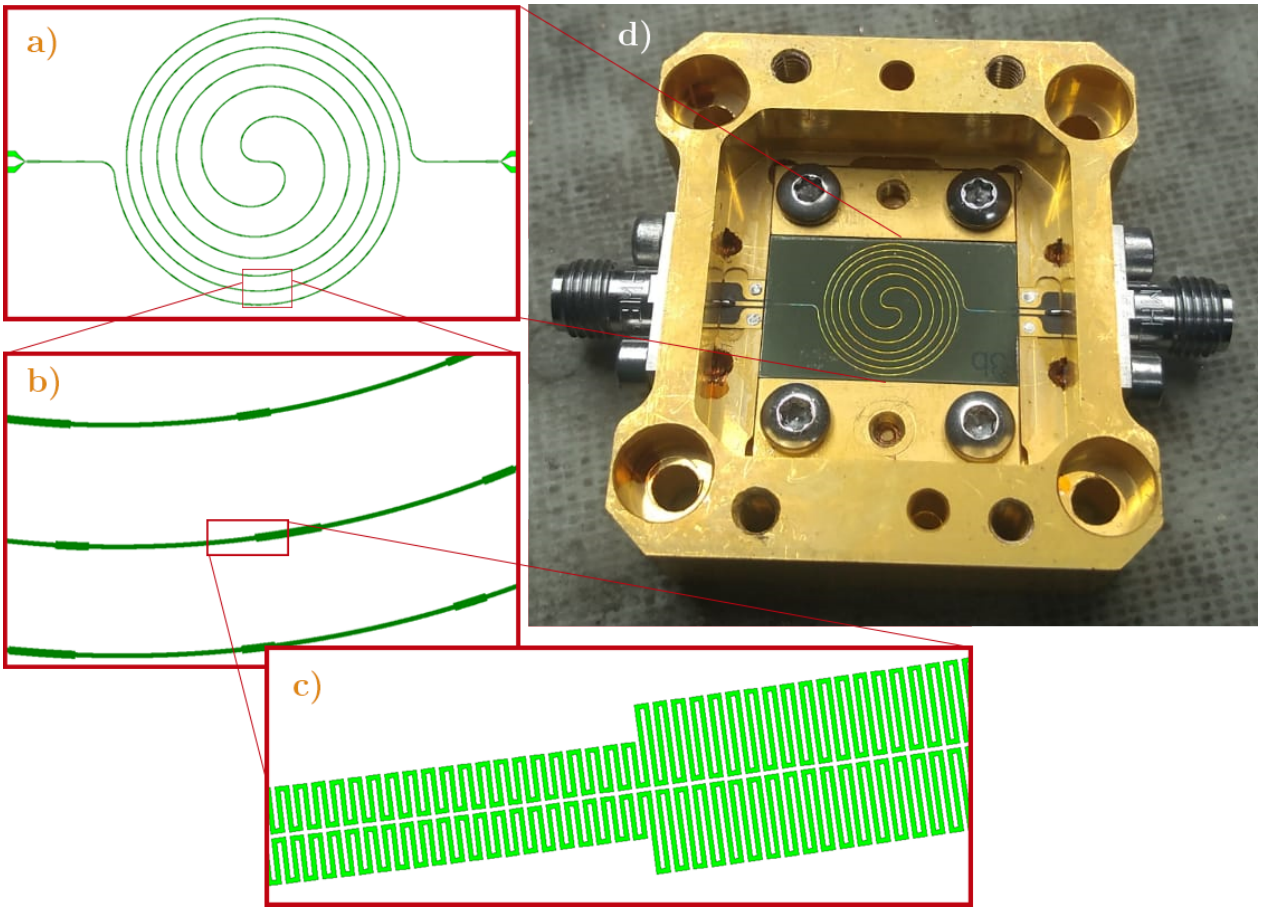

Figure 6.1: Fabricated artificial-CPW. (a) Top view of the sample with the TL in spiral configuration in order to make better use of the available space. The substrate is colored in green, and the superconductor is white. (b) Zoom on a small section of the TL showing the Floquet structure. (c) Further zoom that shows the inner structure of the TL segments that define an artificial-CPW. (d) Photo to the fabricated device placed in a holder. Images given by Daniel Valenzuela [6].

in gain must be taken with caution, because other signals generated from A_{3p} are being blindly ignored here.

3. $\nu_p = 2.495$ GHz, which is even further the zone 3 (a new zone that also considers the effect of the $GL_0\tilde{I}^3\omega/3$ term should be used here[1]). Nonetheless, the design was made taken this value in consideration while using the Old model. Hence, the prediction for this case using all the models described in this thesis are shown to later see in the experiment which is closer. It is important though, that not obtaining the result predicted by the New3 model, does not rule out the model, because as explained before, a different model should be used there.

The gains for each pump frequency of interest and a sweep of initial pump amplitudes are shown in Figure 6.7. This data is left in this thesis to later analyze once the experimental

[1]This analysis is beyond the scope of this thesis.

D_0 (mm)	D_0' (mm)	D_0'' (mm)	D_1 (mm)	d (mm)
1.566	0.78	0.798	0.24	4.71

Table 6.1: Unit cell values that define the Floquet transmission line designed with artificial-CPW. Data given by Daniel Valenzuela, a colleague (PhD student) from the research group.

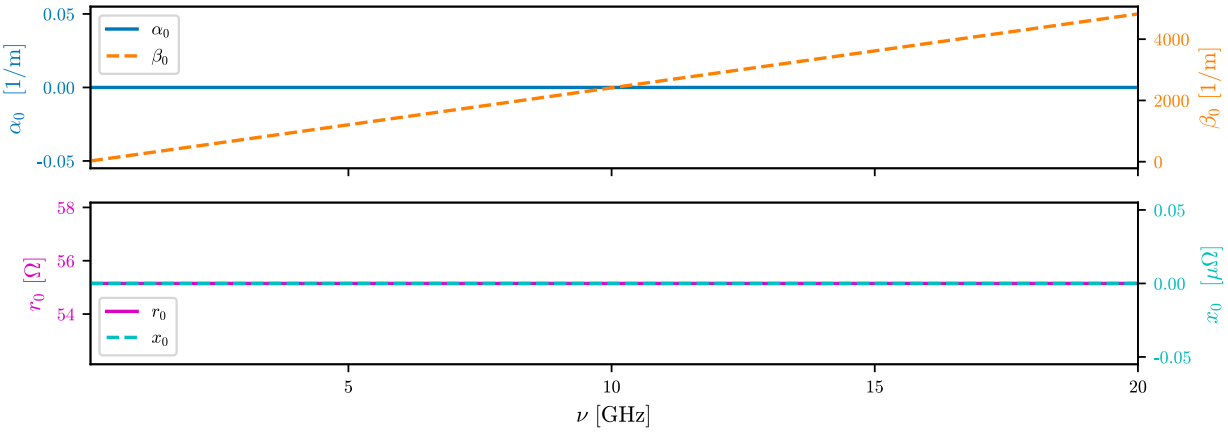

Figure 6.2: Characteristics of the central transmission line (without the dispersive loads) for the microstrip design. Unlike the previous designs, the dissipation effects have been neglected in here, resulting in $\alpha_0(\nu) = x_0(\nu) = 0$. Data given by Daniel Valenzuela [6].

measurements are obtained. Nonetheless, from the results shown and the knowledge acquired throughout this thesis, the case of $\nu_p = 1.71$ GHz is the one recommended to obtain the best results in gain of the target signal.

6.2 Conclusions

Very different results of gain were obtained, depending on the frequency operation region. Results, different than the obtained in chapters 5 and 5, were obtained because in this new case, the design was already done, not considering all the design methods and conclusions reported in this thesis. In fact, the design was done using the Old model, with the objective of operating in a zone not studied in this thesis. However, the nearest zone studied corresponds to zone 3, whose model predicts no gain, contrary to all the others derived. The operation regions simulated are very different in nature and hence, are very interesting for experimental verification. Nonetheless, based on the design guide constructed in chapter 5, the artificial-CPW design presented here is very far from optimal. Of course, the future experimental results will unveil the final conclusions.

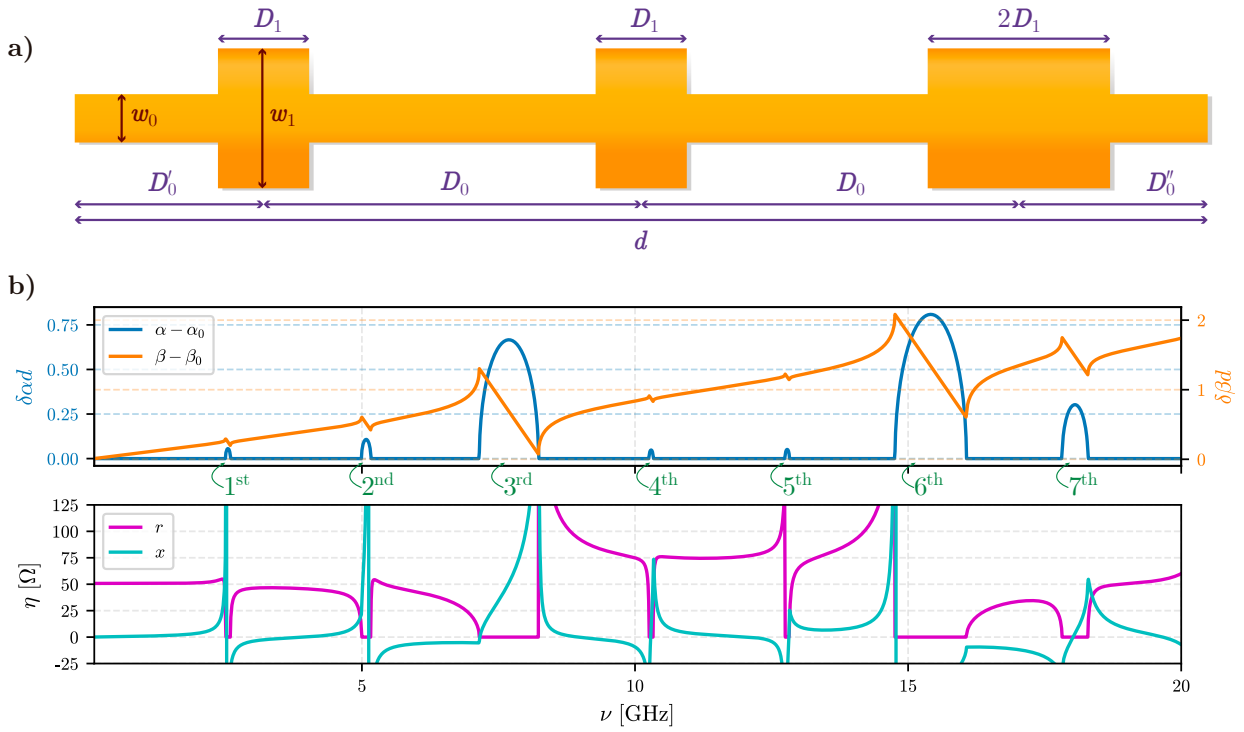

Figure 6.3: (a) Floquet transmission line consisting of a central line of width w_0 and dispersive loads of width $w_1 > w_0$. The lengths D_0, D'_0, D''_0 and D_1 are given in Table 4.2. (b) Characteristics of the Floquet transmission line for the artificial-CPW design, given by Daniel Valenzuela [6]. Seven stopbands are shown, enumerated (in green) from the 1^{st} up to the 7^{th}.

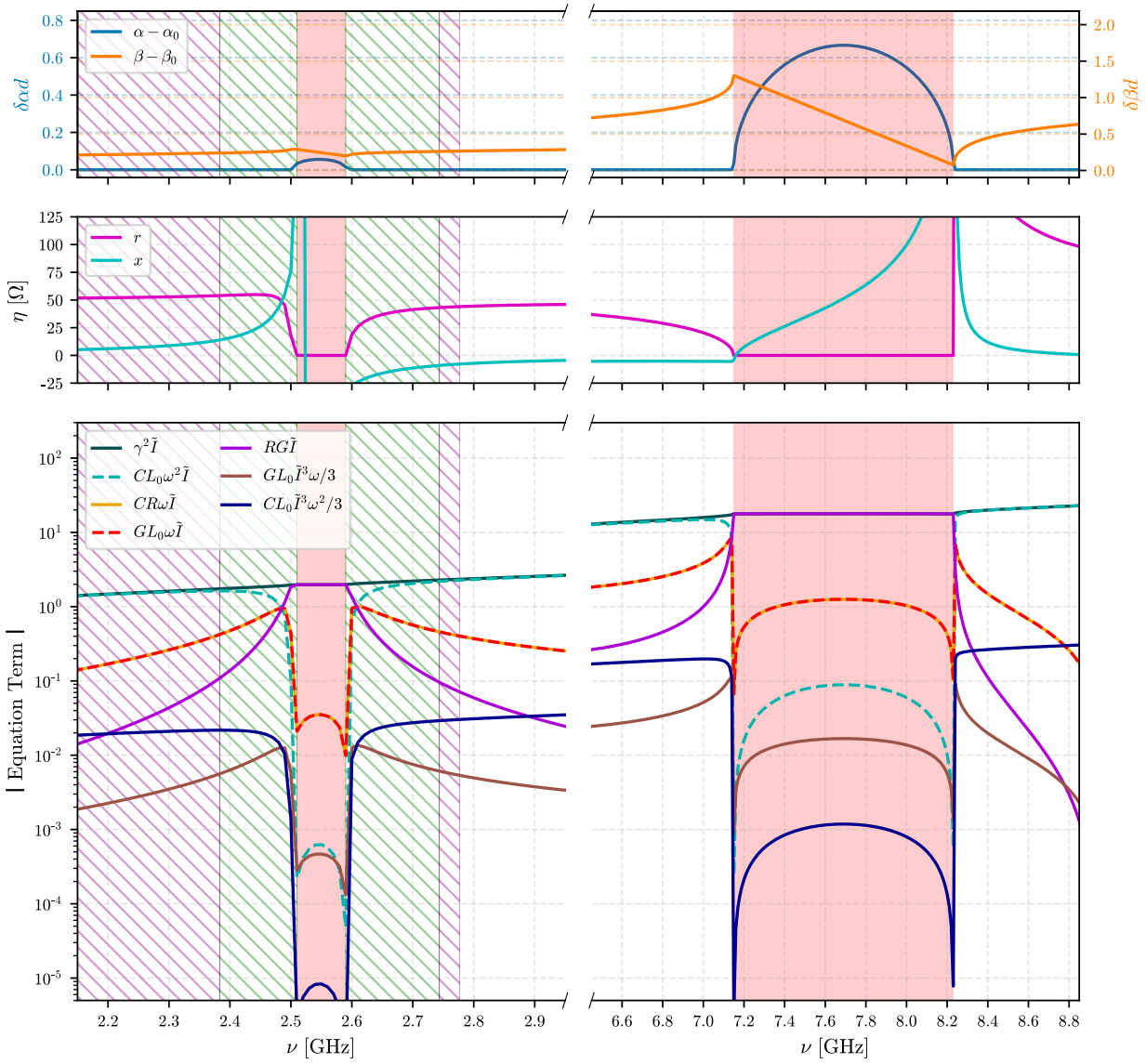

Figure 6.4: Dispersion relation $\{\alpha(\nu), \beta(\nu)\}$ and characteristic impedance $\eta(\nu)$ from Figure 6.3.b, zoomed in around the 1st (left column) and 3rd (right column) stopbands (marked as red zones). The magnitudes of the equation terms are also shown for the case $\tilde{I} \equiv I/I_* = 0.2$. The green dashed zones on the left, correspond to frequencies where its third harmonic 3ν falls in the stopband shown on the right. The purple dashed zones on the left correspond to frequencies such that 3ν falls in a zone outside the stopbands where $|RG\tilde{I}| > |CL_0\tilde{I}^3\omega^2/3|$.

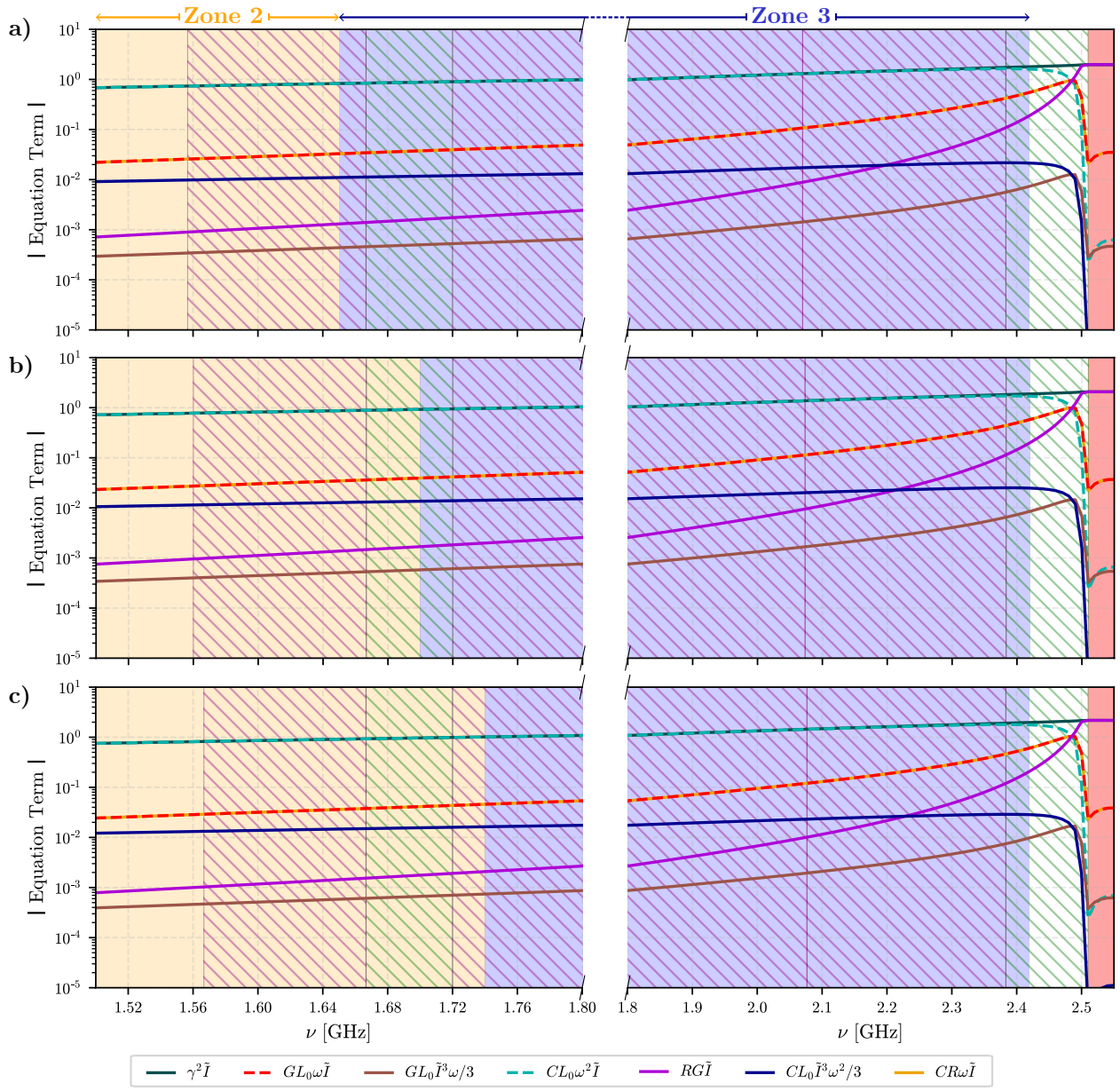

Figure 6.5: Magnitudes of the equation terms near the 1st stopband. The zones 1, 2, and 3 define the range of frequencies where the models New1, New2, and New3 dominate the dynamics, respectively. The magnitudes of the total current are (a) $\tilde{I} = 0.2$, (b) $\tilde{I} = 0.21$, and (c) $\tilde{I} = 0.22$. The green dashed region around 1.7 GHz corresponds to frequencies ν such that 3ν falls inside the 2nd stopband. It is observed that this green dashed region on the left column can be in the zone 2 or zone 3, depending on $\tilde{I}$.

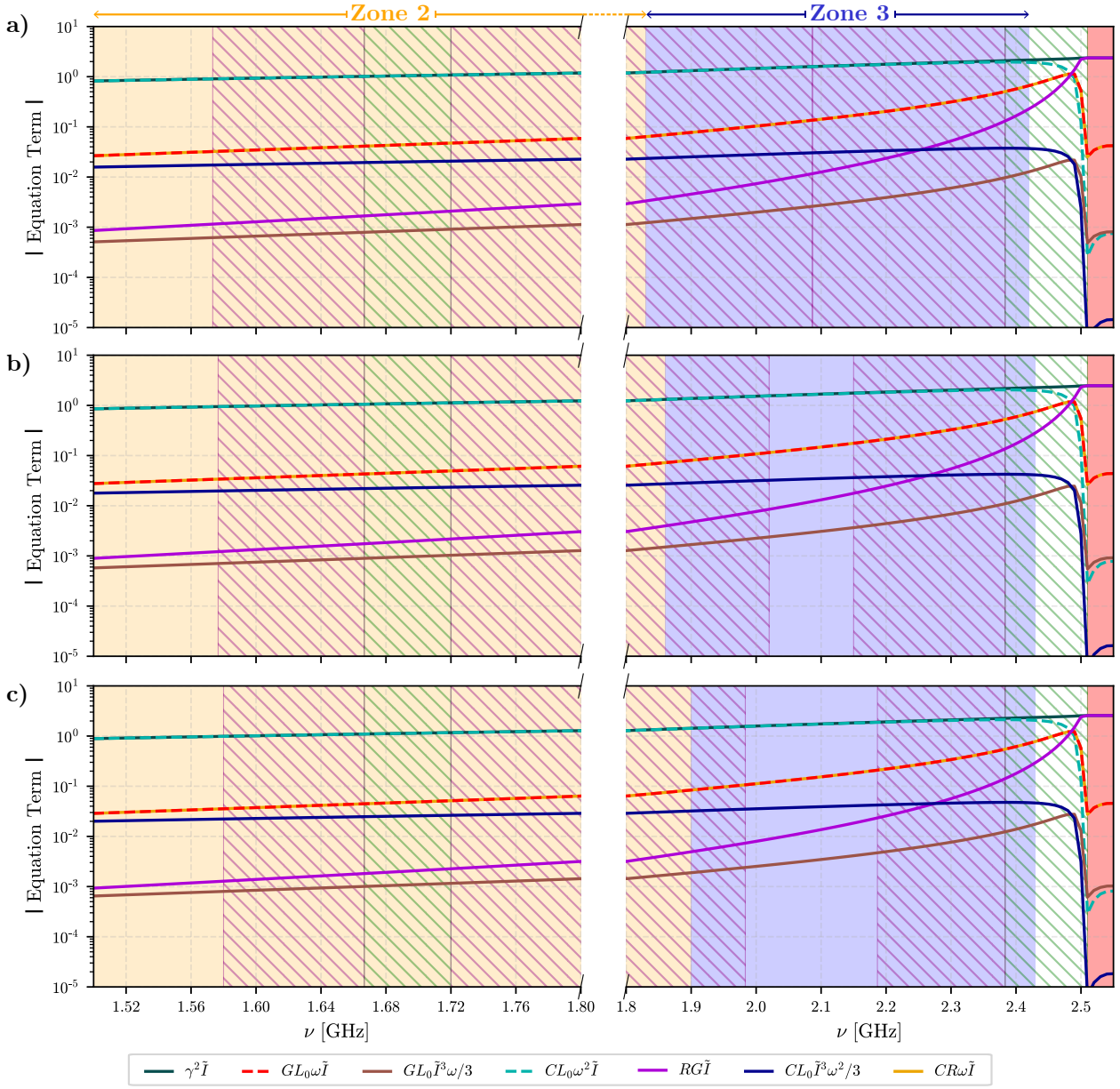

Figure 6.6: Continuation of Figure 6.5. The magnitudes of the total current are (a) $\tilde{I} = 0.24$, (b) $\tilde{I} = 0.25$, and (c) $\tilde{I} = 0.26$. It is observed that the continuous purple dashed region around 2.1 GHz at $\tilde{I} = 0.24$ starts separating for larger $\tilde{I}$.

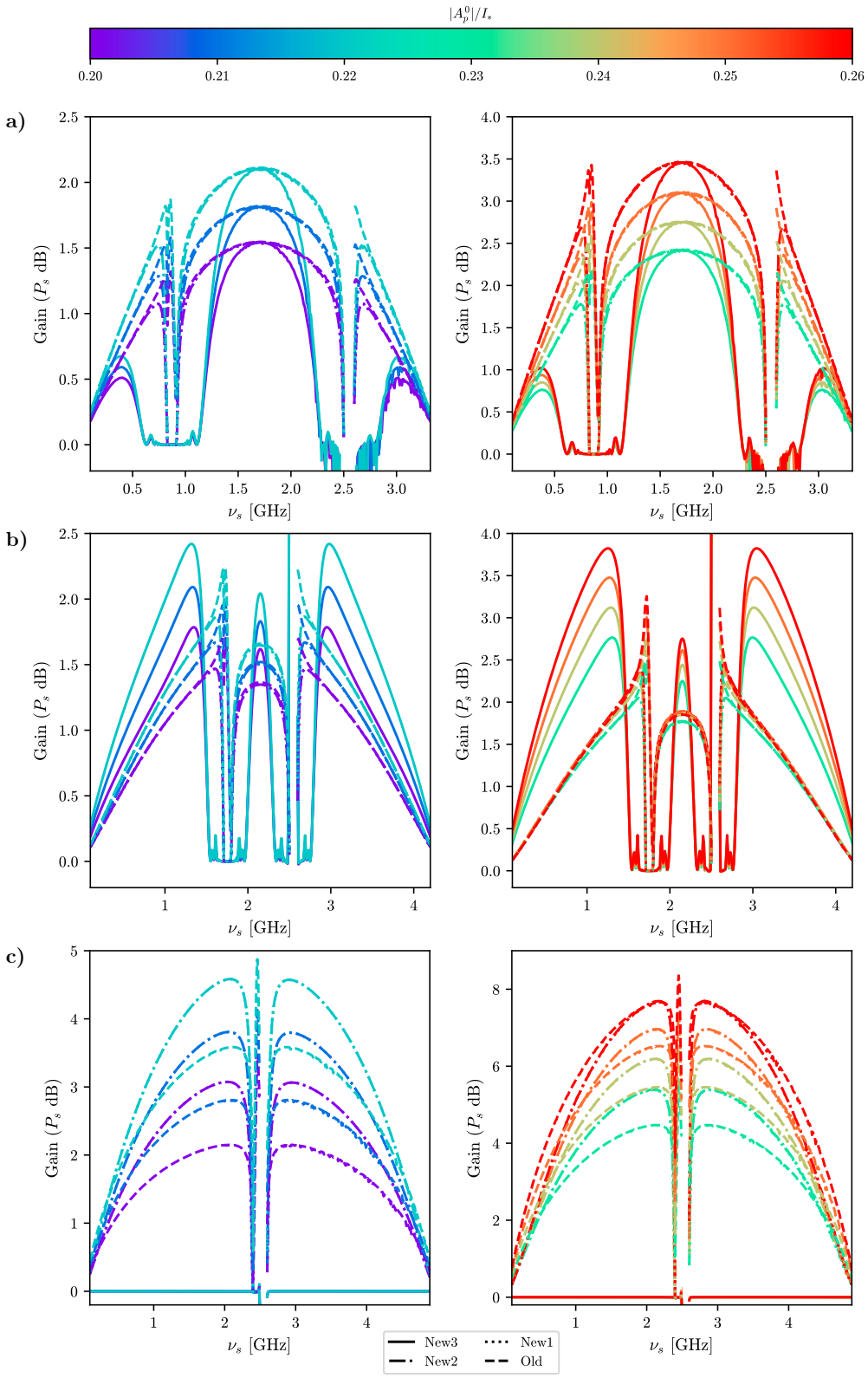

Figure 6.7: Gain of the target signal at $z/d = 62$ for various values of initial pump amplitude A_p^0 and (a) $\nu_p = 1.71$ GHz, (b) $\nu_p = 2.15$ GHz, (c) $\nu_p = 2.495$ GHz. The maximum gain around the pump frequency, as well as the corresponding fractional bandwidth B_f, and over-5dB-fractional bandwidth B_{o5f} are not calculated because they can not be defined in a same practical way for all cases.

Conclusions and future work

In this thesis, a new theoretical framework to simulate and design KI-TWPAs has been developed. This has been achieved by, first, performing a formal derivation of the amplitude equations from which the gain of the target signal is obtained when the device operates as a FWM process. Moreover, three models have been obtained, each dominating under specific circumstances identified as frequency zones around the stopbands of a Floquet TL. Each of these three models converge to the "Old" model used in the current literature in the expected limiting conditions. Furthermore, from the mathematical procedure followed, the signals generated throughout the FWM process have been derived. The amplitude equations have been also obtained for different cases that consider different amount of initial signals, including the target, idler, pump, and third pump's harmonic signals. Additionally, the need of the idler in order to achieve amplification has been formally deduced, whilst the total phase mismatch between the target, idler, and pump signals has been identified as the main cause responsible of achieving amplification.

To complete the developed theoretical framework, the different models have been applied to CPW, MS, and artificial-CPW designs. From these results, it has been concluded that one of the three derived models, namely the "New3" model, gives the largest gain of the target signal, under some operation conditions. The reason for this has been identified as a stabilization of the phase mismatch near its optimal value $\pi/2$, enhancing energy transfer from the pump towards the target and idler signals. Additionally, the suppression of the third pump's harmonic has been studied, obtaining converging results between the cases that consider it and the ones that neglect it, as long as the harmonic is suppressed because of it falling inside a stopband. The suppression of this harmonic is optimal, since otherwise, some energy would be transferred towards the harmonic instead of the target and idler signals.

A KI-TWPA design guide has been presented, allowing a better comprehension of how to change the design parameters in order to enhance the amplifier's performance in terms of gain and fractional bandwidth. It is concluded that the parameter's tuning must be done with the goal of obtaining a highly non-linear dispersion relation of the TL in order to allow better tuning of the phase mismatch. In addition, the pump frequency must operate in a zone where the New3 model dominates in its optimal conditions and where the third pump's harmonic is suppressed by a stopband.

Finally, predictions of the gain results for an artificial-CPW design have been performed. These predictions are to be tested soon in the lab, experimentally measuring them, and so, ideally validating the models derived throughout this thesis.

Bibliography

[1] A. H. Nayfeh and D. T. Mook, *Parametrically Excited Systems*. John Wiley & Sons, Ltd, 1995, ch. 5, pp. 258–364. [Online]. Available: https://onlinelibrary.wiley.com/doi/abs/10.1002/9783527617586.ch5

[2] A. Alexandrov, *Theory of Superconductivity: From Weak to Strong Coupling*, 10 2003.

[3] D. M. Pozar, *Microwave engineering; 3rd ed.* Wiley, 2012.

[4] J. Perruisseau-Carrier, "Microwave periodic structures based on microelectromechanical systems (mems) and micromachining techniques," Ph.D. dissertation, École Polytechnique Fédérale de Lausanne, 2007.

[5] S. Chaudhuri, J. Gao, and K. Irwin, "Simulation and analysis of superconducting traveling-wave parametric amplifiers," *IEEE Transactions on Applied Superconductivity*, vol. 25, no. 3, pp. 1–5, 2015.

[6] D. Valenzuela, *PhD Thesis in Progress*, 2022.

[7] M. W. Pospieszalski, "HFET receivers for ALMA bands 1, 2 and 3," *presented at ALMA in the Coming Decade: A Development Workshop*, 2011. [Online]. Available: https://science.nrao.edu/facilities/alma/alma2011/ALMA-CDP/index

[8] E. A. Tholén, A. Ergül, E. M. Doherty, F. M. Weber, F. Grégis, and D. B. Haviland, "Nonlinearities and parametric amplification in superconducting coplanar waveguide resonators," *Applied Physics Letters*, vol. 90, no. 25, p. 253509, 2007. [Online]. Available: https://doi.org/10.1063/1.2750520

[9] B. Abdo, O. Suchoi, E. Segev, O. Shtempluck, M. Blencowe, and E. Buks, "Intermodulation and parametric amplification in a superconducting stripline resonator integrated with a dc-SQUID," *EPL (Europhysics Letters)*, vol. 85, no. 6, p. 68001, mar 2009. [Online]. Available: https://doi.org/10.1209%2F0295-5075%2F85%2F68001

[10] N. Bergeal, F. Schackert, M. Metcalfe, R. Vijay, V. E. Manucharyan, L. Frunzio, D. E. Prober, R. J. Schoelkopf, S. M. Girvin, and M. H. Devoret, "Phase-preserving amplification near the quantum limit with a josephson ring modulator," *Nature*, vol. 465, no. 7294, pp. 64–68, May 2010. [Online]. Available: https://doi.org/10.1038/nature09035

[11] M. Rehák, P. Neilinger, M. Grajcar, G. Oelsner, U. Hübner, E. Il'ichev, and H.-G.

Meyer, "Parametric amplification by coupled flux qubits," *Applied Physics Letters*, vol. 104, no. 16, p. 162604, 2014. [Online]. Available: https://doi.org/10.1063/1.4873719

[12] M. T. Bell and A. Samolov, "Squid based superconducting traveling-wave parametric amplifier," *IEEE/CSC & ESAS SUPERCONDUCTIVITY NEWS FORUM (global edition)*, 2014.

[13] C. Macklin, K. O'Brien, D. Hover, M. E. Schwartz, V. Bolkhovsky, X. Zhang, W. D. Oliver, and I. Siddiqi, "A near–quantum-limited josephson traveling-wave parametric amplifier," *Science*, vol. 350, no. 6258, pp. 307–310, 2015. [Online]. Available: https://science.sciencemag.org/content/350/6258/307

[14] S. Chaudhuri, D. Li, K. D. Irwin, C. Bockstiegel, J. Hubmayr, J. N. Ullom, M. R. Vissers, and J. Gao, "Broadband parametric amplifiers based on nonlinear kinetic inductance artificial transmission lines," *Applied Physics Letters*, vol. 110, no. 15, p. 152601, 2017. [Online]. Available: https://doi.org/10.1063/1.4980102

[15] S. Zhao, S. Withington, D. J. Goldie, and C. N. Thomas, "Loss and saturation in superconducting travelling-wave parametric amplifiers," *Journal of Physics D: Applied Physics*, vol. 52, no. 41, p. 415301, jul 2019. [Online]. Available: https://doi.org/10.1088%2F1361-6463%2Fab3236

[16] L. Planat, A. Ranadive, R. Dassonneville, J. Puertas Martínez, S. Léger, C. Naud, O. Buisson, W. Hasch-Guichard, D. M. Basko, and N. Roch, "Photonic-crystal josephson traveling-wave parametric amplifier," *Phys. Rev. X*, vol. 10, p. 021021, Apr 2020. [Online]. Available: https://link.aps.org/doi/10.1103/PhysRevX.10.021021

[17] M. Malnou, M. Vissers, J. Wheeler, J. Aumentado, J. Hubmayr, J. Ullom, and J. Gao, "Three-wave mixing kinetic inductance traveling-wave amplifier with near-quantum-limited noise performance," *PRX Quantum*, vol. 2, p. 010302, Jan 2021. [Online]. Available: https://link.aps.org/doi/10.1103/PRXQuantum.2.010302

[18] S. Shu, N. Klimovich, B. H. Eom, A. D. Beyer, R. B. Thakur, H. G. Leduc, and P. K. Day, "Nonlinearity and wide-band parametric amplification in a (nb,ti)n microstrip transmission line," *Phys. Rev. Research*, vol. 3, p. 023184, Jun 2021. [Online]. Available: https://link.aps.org/doi/10.1103/PhysRevResearch.3.023184

[19] M. Malnou, J. Aumentado, M. R. Vissers, J. D. Wheeler, J. Hubmayr, J. N. Ullom, and J. Gao, "Performance of a kinetic-inductance traveling-wave parametric amplifier at 4 kelvin: Toward an alternative to semiconductor amplifiers," 2021. [Online]. Available: https://arxiv.org/abs/2110.08142

[20] B. H. Eom *et al.*, "A wideband, low-noise superconducting amplifier with high dynamic range," *Nature Phys*, vol. 8, pp. 623–627, 2012.

[21] A. D. O'Connell, M. Ansmann, R. C. Bialczak, M. Hofheinz, N. Katz, E. Lucero, C. McKenney, M. Neeley, H. Wang, E. M. Weig, A. N. Cleland, and J. M. Martinis, "Microwave dielectric loss at single photon energies and millikelvin temperatures," *Applied Physics Letters*, vol. 92, no. 11, p. 112903, 2008. [Online]. Available:

https://doi.org/10.1063/1.2898887

[22] A. A. Adamyan, S. E. de Graaf, S. E. Kubatkin, and A. V. Danilov, "Superconducting microwave parametric amplifier based on a quasi-fractal slow propagation line," *Journal of Applied Physics*, vol. 119, no. 8, p. 083901, 2016. [Online]. Available: https://doi.org/10.1063/1.4942362

[23] C. Bockstiegel *et al.*, "Development of a broadband nbtin traveling wave parametric amplifier for mkid readout," *J Low Temp Phys*, vol. 176, p. 476–482, 2014.

[24] W. Shan, Y. Sekimoto, and T. Noguchi, "Parametric amplification in a superconducting microstrip transmission line," *IEEE Transactions on Applied Superconductivity*, vol. 26, no. 6, pp. 1–9, 2016.

[25] P. K. Day, B. H. Eom, H. G. Leduc, J. Zmuidzinas, C. Groppi, P. Mauskopf, J. Lamb, and D. Woody, "Wideband paramps for the millimeter and submillimeter bands," in *2014 39th International Conference on Infrared, Millimeter, and Terahertz waves (IRMMW-THz)*, 2014, pp. 1–2.

[26] M. R. Vissers, R. P. Erickson, H.-S. Ku, L. Vale, X. Wu, G. C. Hilton, and D. P. Pappas, "Low-noise kinetic inductance traveling-wave amplifier using three-wave mixing," *Applied Physics Letters*, vol. 108, no. 1, p. 012601, 2016. [Online]. Available: https://doi.org/10.1063/1.4937922

[27] M. Takeda, T. Kojima, A. Saito, K. Makise, and H. Shimakage, "Evaluation of kinetic-inductance nonlinearity in a single-crystal nbtin-based coplanar waveguide," *JJAP Conference Proceedings*, vol. 011502, p. 4, 2016. [Online]. Available: https://journals.jsap.jp/jjapproceedings/online/4-011502

[28] P. Powers and J. Haus, *Fundamentals of Nonlinear Optics*. CRC Press, 2017. [Online]. Available: https://books.google.cl/books?id=m-O_DgAAQBAJ

[29] J. Moloney and A. Newell, *Nonlinear Optics*. CRC Press, 2018. [Online]. Available: https://books.google.cl/books?id=EUpaDwAAQBAJ

[30] A. H. Nayfeh and D. T. Mook, *Introduction*. John Wiley & Sons, Ltd, 1995, ch. 1, pp. 1–38. [Online]. Available: https://onlinelibrary.wiley.com/doi/abs/10.1002/9783527617586.ch1

[31] J. Peña-Ramírez, R. H. B. Fey, and H. Nijmeijer, *An Introduction to Parametric Resonance*. New York, NY: Springer New York, 2012, pp. 1–13. [Online]. Available: https://doi.org/10.1007/978-1-4614-1043-0_1

[32] E. Snider, N. Dasenbrock-Gammon, R. McBride, M. Debessai, H. Vindana, K. Vencatasamy, K. V. Lawler, A. Salamat, and R. P. Dias, "Room-temperature superconductivity in a carbonaceous sulfur hydride," *Nature*, vol. 586, pp. 373–377, 2020. [Online]. Available: https://doi.org/10.1038/s41586-020-2801-z

[33] D. C. Mattis and J. Bardeen, "Theory of the anomalous skin effect in normal

and superconducting metals," *Phys. Rev.*, vol. 111, pp. 412–417, Jul 1958. [Online]. Available: https://link.aps.org/doi/10.1103/PhysRev.111.412

[34] S. Zhao, D. J. Goldie, S. Withington, and C. N. Thomas, "Exploring the performance of thin-film superconducting multilayers as kinetic inductance detectors for low-frequency detection," *Superconductor Science and Technology*, vol. 31, no. 1, p. 015007, nov 2017. [Online]. Available: https://doi.org/10.1088/1361-6668/aa94b7

[35] R. Sorrentino and G. Bianchi, *Microwave and RF Engineering.* Wiley, 2010.

[36] R. N. Simons, *Conventional Coplanar Waveguide.* John Wiley & Sons, Ltd, 2001, ch. 2, pp. 11–86. [Online]. Available: https://onlinelibrary.wiley.com/doi/abs/10.1002/0471224758.ch2

[37] R. E. Collin, *Foundations for Microwave Engineering*, 2nd ed. New Delhi: Wiley, 2001.

[38] S. Zhao, S. Withington, D. J. Goldie, and C. N. Thomas, "Electromagnetic models for multilayer superconducting transmission lines," *Superconductor Science and Technology*, vol. 31, no. 8, p. 085012, jul 2018. [Online]. Available: https://doi.org/10.1088/1361-6668/aacc53

[39] M. Abramowitz and I. A. Stegun, *Handbook of Mathematical Functions with Formulas, Graphs, and Mathematical Tables.* Dover Publications, 1972.

[40] B. Young, S. Fauve, B. E. DeRemer, and S. Meacham, *1991 Summer Study Program in Geophysical Fluid Dynamics: patterns in fluid flow.* Woods Hole Oceanographic Institution, 1991. [Online]. Available: https://doi.org/10.1575/1912/802

Annexed

Derivation of models

A.1 Definition of zones (step 1)

The dynamics of the dimensionless electric current $\tilde{I} \equiv \frac{I}{I_*}$ is given by

$$\left(\frac{\partial^2}{\partial z^2} - CL_0\frac{\partial^2}{\partial t^2} - (CR + GL_0)\frac{\partial}{\partial t} - RG\right)\tilde{I} = \frac{L_0}{3}\left(G\frac{\partial}{\partial t} + C\frac{\partial^2}{\partial t^2}\right)\tilde{I}^3, \tag{A.1}$$

which is a non-linear wave equation that can be compactly written as

$$\mathcal{L}\tilde{I} = \mathcal{N}\tilde{I}^3, \tag{A.2}$$

where

$$\mathcal{L} \equiv \left(\frac{\partial^2}{\partial z^2} - CL_0\frac{\partial^2}{\partial t^2} - (CR + GL_0)\frac{\partial}{\partial t} - RG\right), \tag{A.3}$$

$$\mathcal{N} \equiv \frac{L_0}{3}\left(G\frac{\partial}{\partial t} + C\frac{\partial^2}{\partial t^2}\right) \tag{A.4}$$

are the differential operators acting on the linear and non-linear terms of the equation, respectively. Moreover, $\mathcal{L}$ can be separated as the sum of a "common" operator $\mathcal{L}_c$ and an "uncommon" operator $\mathcal{L}_u$. The former is corresponds to the part of $\mathcal{L}$ that is also contained in $\mathcal{N}$, while the latter is what is left, i.e. $\mathcal{L}_u \equiv \mathcal{L} - \mathcal{L}_c$. Hence,

$$\mathcal{L}_c \equiv -\left(CL_0\frac{\partial^2}{\partial t^2} + GL_0\frac{\partial}{\partial t}\right), \tag{A.5}$$

$$\mathcal{L}_u \equiv \left(\frac{\partial^2}{\partial z^2} - CR\frac{\partial}{\partial t} - RG\right), \tag{A.6}$$

$$\mathcal{L} = \mathcal{L}_c + \mathcal{L}_u, \tag{A.7}$$

$$\mathcal{N} = -\frac{1}{3}\mathcal{L}_c. \tag{A.8}$$

Therefore, $|\mathcal{N}\tilde{I}^3| < |\mathcal{L}_c\tilde{I}|$ because $|\tilde{I}| < 1 \Rightarrow |\tilde{I}|^3 < |\tilde{I}|$. This means that the non-linear terms of the equation can always be studied as perturbations to the linear terms involved in $\mathcal{L}_c$.

More in detail,

$$\epsilon\mathcal{O}\left(\mathcal{L}_c\tilde{I}\right) = \mathcal{O}\left(\mathcal{N}\tilde{I}^3\right), \tag{A.9}$$

where $\mathcal{O}(\cdot)$ is an operator that returns the order of the input, and $\epsilon \ll 1$ is a positive factor that compensates for the difference in orders between $\mathcal{L}_c\tilde{I}$ and $\mathcal{N}\tilde{I}^3$. In fact, $\epsilon = \mathcal{O}(\mathcal{N}\tilde{I}^3)/\mathcal{O}(\mathcal{L}_c\tilde{I})$ quantifies how much smaller is the non-linear term over the common linear one. This sets the minimum scale to consider in order to appreciate a non-linear effect in the dynamical evolution of equation A.1. However, more details on the orders of each of the terms involved in $\mathcal{L}_c$ and $\mathcal{L}_u$ are required to set the non-linear wave equation at first order in ϵ. For the KI-TWPA designs studied in this thesis, the typical orders are the ones shown in Figure A.1, where the spatial and temporal Fourier transforms have been used to relate $\frac{\partial}{\partial z} \mapsto -\mathrm{j}\gamma$ and $\frac{\partial}{\partial t} \mapsto \mathrm{j}\omega \equiv \mathrm{j}2\pi\nu$.

Figure A.1 shows that the dominating equation terms outside the stopbands are[1]

$$\mathcal{L}^{(0)}\tilde{I} \equiv \left(\frac{\partial^2}{\partial z^2} - CL_0\frac{\partial^2}{\partial t^2}\right)\tilde{I}, \tag{A.10}$$

which contains a term of $\mathcal{L}_c$. Therefore, from equation A.9, it is known that the non-linear effects will manifest at orders ϵ smaller than $\mathcal{O}(\mathcal{L}^{(0)}\tilde{I})$. Hence, the non-linear equation can be set to be solved as a perturbation, in orders of ϵ, to the linear equation $\mathcal{L}^{(0)}\tilde{I} = 0$. Nonetheless, all the equation terms of the order $\mathcal{O}(\epsilon) = \epsilon\mathcal{O}(\mathcal{L}^{(0)})$ must be included to complete the perturbative terms at first order in ϵ. In Figure A.1, three zones with different terms acting at order $\mathcal{O}(\epsilon)$ are identified by approximating $\mathcal{O}(\tilde{\epsilon}) \approx \mathcal{O}(\epsilon), \forall\tilde{\epsilon} \in (\epsilon\sqrt{\epsilon}, \epsilon/\sqrt{\epsilon})$, and defining

$$\epsilon_1 \equiv \frac{\min\left\{\mathcal{O}\left(GL_0\frac{\partial}{\partial t}\tilde{I}\right), \mathcal{O}\left(\frac{1}{3}CL_0\frac{\partial^2}{\partial t^2}\tilde{I}^3\right)\right\}}{\max\left\{\mathcal{O}\left(GL_0\frac{\partial}{\partial t}\tilde{I}\right), \mathcal{O}\left(\frac{1}{3}CL_0\frac{\partial^2}{\partial t^2}\tilde{I}^3\right)\right\}} \approx \frac{\min\left\{\mathcal{O}\left(CR\frac{\partial}{\partial t}\tilde{I}\right), \mathcal{O}\left(\frac{1}{3}CL_0\frac{\partial^2}{\partial t^2}\tilde{I}^3\right)\right\}}{\max\left\{\mathcal{O}\left(CR\frac{\partial}{\partial t}\tilde{I}\right), \mathcal{O}\left(\frac{1}{3}CL_0\frac{\partial^2}{\partial t^2}\tilde{I}^3\right)\right\}}, \tag{A.11}$$

$$\epsilon_2 \equiv \frac{\min\left\{\mathcal{O}\left(RG\tilde{I}\right), \mathcal{O}\left(\frac{1}{3}CL_0\frac{\partial^2}{\partial t^2}\tilde{I}^3\right)\right\}}{\max\left\{\mathcal{O}\left(RG\tilde{I}\right), \mathcal{O}\left(\frac{1}{3}CL_0\frac{\partial^2}{\partial t^2}\tilde{I}^3\right)\right\}}, \tag{A.12}$$

which are positive factors fulfilling $\epsilon_1, \epsilon_2 \ll 1$. Thus, the zones are defined as

- **Zone 1**: $\epsilon_2 < \epsilon_1 < \sqrt{\epsilon}$,
- **Zone 2**: $\epsilon_1 \geq \sqrt{\epsilon}$ and $\epsilon_2 < \sqrt{\epsilon}$,
- **Zone 3**: $\epsilon_2 \geq \sqrt{\epsilon}$ and[2] $\epsilon_1 > \epsilon$,

which set three different perturbative non-linear wave equations at first order in ϵ, namely:

1. Model "**New1**" (over zone 1):

$$\left(\frac{\partial^2}{\partial z^2} - CL_0\frac{\partial^2}{\partial t^2}\right)\tilde{I} = \epsilon\left(\frac{L_0C}{3}\frac{\partial^2}{\partial t^2}\right)\tilde{I}^3. \tag{A.13}$$

[1] With the exception of frequency regions extremely close to the stopbands.

[2] In zone 3, the condition for ϵ_1 has been relaxed so that ϵ_2 defines the limit closest to the stopbands.

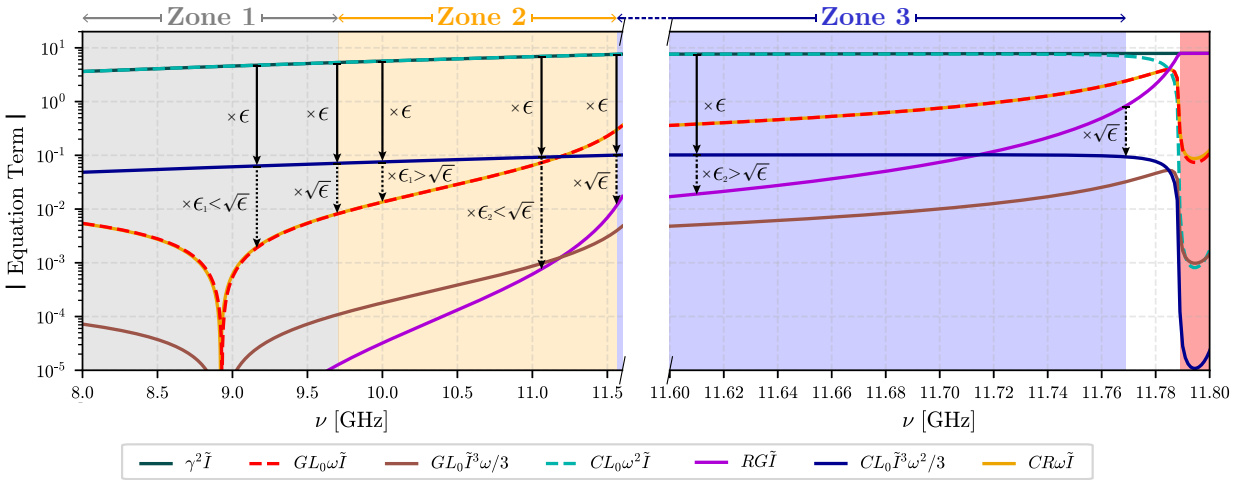

Figure A.1: Magnitudes of the equation terms near the 2nd stopband of the CPW design described in chapter 4. The zones 1, 2, and 3 define the range of frequencies where the models New1, New2, and New3 dominate the dynamics, respectively. The magnitude of the total current is $\tilde{I} = 0.2$. The defined values of the positive factors $\epsilon, \epsilon_1, \epsilon_2 \ll 1$ are shown for each zone.

2. Model "**New2**" (over zone 2):

$$\left(\frac{\partial^2}{\partial z^2} - CL_0\frac{\partial^2}{\partial t^2}\right)\tilde{I} = \epsilon(CR + GL_0)\frac{\partial}{\partial t}\tilde{I} + \epsilon\left(\frac{L_0C}{3}\frac{\partial^2}{\partial t^2}\right)\tilde{I}^3. \tag{A.14}$$

3. Model "**New3**" (over zone 3):

$$\left(\frac{\partial^2}{\partial z^2} - CL_0\frac{\partial^2}{\partial t^2}\right)I = \epsilon RG\tilde{I} + \epsilon(CR + GL_0)\frac{\partial}{\partial t}\tilde{I} + \epsilon\left(\frac{L_0C}{3}\frac{\partial^2}{\partial t^2}\right)\tilde{I}^3. \tag{A.15}$$

All these models can be compactly written as

$$\mathcal{L}^{(0)}\tilde{I} = \epsilon\left(\mathcal{L}^{(1)}\tilde{I} + \mathcal{N}^{(1)}\tilde{I}^3\right), \tag{A.16}$$

where

$$\mathcal{L}^{(0)} \equiv \frac{\partial^2}{\partial z^2} - CL_0\frac{\partial^2}{\partial t^2}, \tag{A.17}$$

$$\mathcal{N}^{(1)} \equiv \frac{L_0C}{3}\frac{\partial^2}{\partial t^2}, \tag{A.18}$$

$$\mathcal{L}^{(1)} \equiv \begin{cases} 0 & \text{for model 1} \\ (CR + GL_0)\frac{\partial}{\partial t} & \text{for model 2} \\ RG + (CR + GL_0)\frac{\partial}{\partial t} & \text{for model 3} \end{cases}. \tag{A.19}$$

What has been done in this section, finishing with the derivation of the models, corresponds to **step 1** of the multiple scales method described in chapter 2.

A.2 Derivation of the amplitude equations

A.2.1 Step 2

In KI-TWPAs, the amplification occurs as the wave travels through the transmission line, i.e. along the z axis. Since the amplification comes from the non-linear term $\mathcal{N}^{(1)}\tilde{I}$, which is a perturbation to the linear term $\mathcal{L}^{(0)}\tilde{I}$, the amplitude of the traveling waves must follow the amplification dynamics very slowly, compared to the wave dynamics itself that is given by $\mathcal{L}^{(0)}\tilde{I} = 0$ at zeroth order in ϵ. Therefore, the spatial derivatives with respect to z are to be scaled in multiple orders of ϵ that can be considered independent from each other,

$$\frac{\partial}{\partial z} \mapsto \frac{\partial}{\partial z} + \epsilon\frac{\partial}{\partial z_1} + \epsilon^2\frac{\partial}{\partial z_2} + \dots, \tag{A.20}$$

where

$$z_n = \epsilon^n z \tag{A.21}$$

are the different scales along the z axis that are effectively considered independent variables between each other. On the other hand, the time t is not separated in multiple orders because only traveling waves are considered, rather than stationary ones, implying that at a fixed z there is no signal amplification as t increases.

By applying the transformation A.20, the second spatial derivative involved in $\mathcal{L}^{(\prime)}$ transforms as

$$\left(\frac{\partial}{\partial z}\right)\left(\frac{\partial}{\partial z}\right) \mapsto \left(\frac{\partial}{\partial z} + \epsilon\frac{\partial}{\partial z_1} + \dots\right)\left(\frac{\partial}{\partial z} + \epsilon\frac{\partial}{\partial z_1} + \dots\right) \tag{A.22}$$

$$= \frac{\partial^2}{\partial z^2} + \epsilon\left(\frac{\partial}{\partial z}\frac{\partial}{\partial z_1} + \frac{\partial}{\partial z_1}\frac{\partial}{\partial z}\right) + \mathcal{O}\big(\epsilon^2\big), \tag{A.23}$$

where the derivatives with respect to z and z_1 are operators that do not necessarily commute. This depends on the structure of $\tilde{I}$ regarding its dependence on z and z_1, to be determined in later steps of the multiple scales method.

A.2.2 Step 3

To solve the perturbative models described by equation A.16, the current $\tilde{I}$ must be separated in multiple scales in orders of ϵ,

$$\tilde{I} = \tilde{I}^{(0)} + \epsilon\tilde{I}^{(1)} + \epsilon^2\tilde{I}^{(2)} + \dots, \tag{A.24}$$

where $\tilde{I}^{(0)}$ is the solution at zeroth order of equation A.16 after applying the transformation A.22. Furthermore, combining equations A.16, A.17, A.23, and A.24, gives

$$\left(\frac{\partial^2}{\partial z^2} + \epsilon\left(\frac{\partial}{\partial z}\frac{\partial}{\partial z_1} + \frac{\partial}{\partial z_1}\frac{\partial}{\partial z}\right) + \mathcal{O}\big(\epsilon^2\big) - CL_0\frac{\partial^2}{\partial t^2}\right)\left(\tilde{I}^{(0)} + \epsilon\tilde{I}^{(1)} + \dots\right)$$

$$= \epsilon\left(\mathcal{L}^{(1)}\left(\tilde{I}^{(0)} + \epsilon\tilde{I}^{(1)} + \dots\right) + \mathcal{N}^{(1)}\left(\tilde{I}^{(0)} + \epsilon\tilde{I}^{(1)} + \dots\right)^3\right). \tag{A.25}$$

A.2.3 Step 4

The order at which the non-linear term affects the dynamics is $\mathcal{O}(\epsilon)$, derived in step 1. Then, to solve at first order in ϵ, the correct perturbative form of the non-linear wave equation is obtained by writing equation A.25 up to only order $\mathcal{O}(\epsilon)$,

$$\mathcal{L}^{(0)}\tilde{I}^{(0)} + \epsilon\left(\frac{\partial}{\partial z}\frac{\partial}{\partial z_1} + \frac{\partial}{\partial z_1}\frac{\partial}{\partial z}\right)\tilde{I}^{(0)} + \epsilon\mathcal{L}^{(0)}\tilde{I}^{(1)} = \epsilon\left(\mathcal{L}^{(1)}\tilde{I}^{(0)} + \mathcal{N}^{(1)}(\tilde{I}^{(0)})^3\right). \tag{A.26}$$

However, by definition, $\tilde{I}^{(0)}$ is the solution to the zeroth order equation which can be obtained by simply making $\epsilon \to 0$ in equation A.26,

$$\mathcal{L}^{(0)}\tilde{I}^{(0)} = 0. \tag{A.27}$$

Hence, equation A.26 reduces to

$$\mathcal{L}^{(0)}\tilde{I}^{(1)} = -\left(\frac{\partial}{\partial z}\frac{\partial}{\partial z_1} + \frac{\partial}{\partial z_1}\frac{\partial}{\partial z}\right)\tilde{I}^{(0)} + \mathcal{L}^{(1)}\tilde{I}^{(0)} + \mathcal{N}^{(1)}(\tilde{I}^{(0)})^3, \tag{A.28}$$

where a division by ϵ has been performed. Equation A.28 is an equation to obtain the current at first order $\tilde{I}^{(1)}$ from the zeroth order solution $\tilde{I}^{(0)}$.

A.2.4 Step 5

A solution for $\tilde{I}^{(0)}$ is required in order to solve equation A.28 for $\tilde{I}^{(1)}$. From equation A.27, it is clear that the general solution is that of a wave,

$$\tilde{I}^{(0)} = \frac{1}{2}\left(\sum_n^N A_n \mathrm{e}^{\mathrm{j}(\omega_n t - \beta_n z)} + \text{c.c.}\right), \tag{A.29}$$

where A_n are the complex amplitudes, ω_n are the angular frequencies, and β_n are the wavenumbers for each of the N monochromatic signals involved in the process. Nonetheless, since $\mathcal{L}^{(0)}$ does not contain derivatives with respect to $z_m, m > 0$, the quantities A_n, ω_n, β_n may depend on $z_m, m > 0$. Moreover, A_n needs to depend on z_1 in order to allow amplification at scales of the order $\mathcal{O}(\epsilon)$. Hence, $A_n = A_n(z_1)$. Regarding ω_n, there is no dependence on $z_m, m > 0$ because the angular frequency is related to the temporal part of the solution. Instead, β_n should depend on $z_m, m > 0$, but these effect can be absorbed by $A_n = A_n(z_1, z_2, \dots)$, allowing to keep β_n independent of $z_m, m > 0$. Despite this, a better solution at first order is expected if β_n are related to the complete dispersion relation that comes from $\mathcal{L}\tilde{I} = 0$ rather than the dispersion relation related to equation A.27. Therefore, the wavenumbers β_n to be used will be the ones from the complete dispersion relation[3].

Therefore, the solution $\tilde{I}^{(0)}$ from equation A.29 can be recast in a better, more explicit, form for solving at order $\mathcal{O}(\epsilon)$,

$$\tilde{I}^{(0)} = \frac{1}{2}\left(\sum_n^N A_n(z_1) \mathrm{e}^{\mathrm{j}(\omega_n t - \beta_n z)} + \text{c.c.}\right), \tag{A.30}$$

[3]This may be a small change. Moreover, not considering it may result in the same final solution (solving for many order in ϵ), coming from the fact that the solution for the amplitudes A_n adapts. However, the solution at first order in ϵ may be slightly different.

which is known as the slowly varying amplitude approximation.

From equation A.30 it is clear that the derivatives of $\tilde{I}^{(0)}$ with respect to z and z_1 commute. Then, equation A.28 can be rewritten as

$$\mathcal{L}^{(0)}\tilde{I}^{(1)} = -2\frac{\partial^2 \tilde{I}^{(0)}}{\partial z \partial z_1} + \mathcal{L}^{(1)}\tilde{I}^{(0)} + \mathcal{N}^{(1)}(\tilde{I}^{(0)})^3. \tag{A.31}$$

The solution to equation A.31, i.e.

$$\tilde{I}^{(1)} = \mathcal{L}^{(0)\dagger}\left(-2\frac{\partial^2 \tilde{I}^{(0)}}{\partial z \partial z_1} + \mathcal{L}^{(1)}\tilde{I}^{(0)} + \mathcal{N}^{(1)}(\tilde{I}^{(0)})^3\right), \tag{A.32}$$

must respect the multiple scales and can not diverge, which means that secular terms must be avoided. To achieve this goal, the projection of the right hand side of equation A.31 on the eigenbasis of $\mathcal{L}^{(0)\dagger}$ must be null. Therefore, to ensure that the requirement is fulfilled[4],

$$\left\langle \mathrm{e}^{\mathrm{j}\omega_m t} \middle| -2\frac{\partial^2 \tilde{I}^{(0)}}{\partial z \partial z_1} + \mathcal{L}^{(1)}\tilde{I}^{(0)} + \mathcal{N}^{(1)}(\tilde{I}^{(0)})^3 \right\rangle = 0, \tag{A.33}$$

which are the **amplitude equations**. Finally, using equations A.18, A.19, and A.30, the amplitude equations A.33 are explicitly obtained for each model[5]:

1. **Model New1**: the amplitude equation for the $m-$th signal is

$$\frac{\partial A_m}{\partial z} = \frac{f_m \mathrm{e}^{\mathrm{j}\beta_m z}}{3 \cdot 8 \cdot I_*^2} \left\langle \mathrm{e}^{\mathrm{j}\omega_m t} \middle| \left(\sum_n^N A_n \mathrm{e}^{\mathrm{j}(\omega_n t - \beta_n z)} + \text{c.c.} \right)^3 \right\rangle. \tag{A.34}$$

2. **Model New2**: the amplitude equation for the $m-$th signal is

$$\frac{\partial A_m}{\partial z} = -2\alpha_m A_m + \frac{f_m \mathrm{e}^{\mathrm{j}\beta_m z}}{3 \cdot 8 \cdot I_*^2} \left\langle \mathrm{e}^{\mathrm{j}\omega_m t} \middle| \left(\sum_n^N A_n \mathrm{e}^{\mathrm{j}(\omega_n t - \beta_n z)} + \text{c.c.} \right)^3 \right\rangle. \tag{A.35}$$

3. **Model New3**: the amplitude equation for the $m-$th signal is

$$\frac{\partial A_m}{\partial z} = \mathrm{j}g_m A_m - 2\alpha_m A_m + \frac{\mathrm{j}f_m \mathrm{e}^{\mathrm{j}\beta_m z}}{3 \cdot 8 \cdot I_*^2} \left\langle \mathrm{e}^{\mathrm{j}\omega_m t} \middle| \left(\sum_n^N A_n \mathrm{e}^{\mathrm{j}(\omega_n t - \beta_n) z} + \text{c.c.} \right)^3 \right\rangle. \tag{A.36}$$

[4]The projection is done on the temporal eigenbasis only in order to add extra degrees of freedom in the solution regarding the multiple-scaled variable z. It is worth noticing that both options, projecting only on the time basis and projecting on the temporal and spatial basis, were tested throughout the present thesis, but the former gave better results (comparing with experimental data from the literature).

[5]The derivatives with respect to z_1 have been changed to $\frac{\partial}{\partial z}$ by applying $z_1 = \epsilon z$ at the end. The emerging ϵ were reabsorbed by the transmission line parameters.

In all the previous equations,

$$f_m = \frac{1}{2\beta_m}\left(\alpha_m^2 - \beta_m^2 - \frac{|\gamma_m|^2}{|\eta_m|^2}(r_m^2 - x_m^2)\right), \tag{A.37}$$

$$g_m = \frac{\alpha_m^2 r_m^2 - \beta_m^2 x_m^2}{\beta_m(r_m^2 + x_m^2)}, \tag{A.38}$$

which have been obtained by the relation between the transmission line parameters R_m, G_m, $L_{0,m}$, C_m and the propagation constant $\gamma_m \equiv \alpha_m + \mathrm{j}\beta_m$ together with the characteristic impedance $\eta_m \equiv r_m + \mathrm{j}x_m$,

$$\gamma_m = \sqrt{(R_m + \mathrm{j}\omega_m L_{0,m})(G_m + \mathrm{j}\omega_m C_m)}, \tag{A.39}$$

$$\eta_m = \sqrt{\frac{R_m + \mathrm{j}\omega_m L_{0,m}}{G_m + \mathrm{j}\omega_m C_m}}. \tag{A.40}$$

■